

UNSTEADY DRAG AND DYNAMIC STALL AS SIMULATED
IN A VARYING FREESTREAM

A THESIS

Presented to

The Faculty of the Division of Graduate
Studies and Research

by

Donald Lee Kunz

In Partial Fulfillment

of the Requirements for the Degree

Doctor of Philosophy

in the School of Aerospace Engineering

Georgia Institute of Technology

March 1976

ACKNOWLEDGMENTS

First and foremost among those whom I wish to than is Dr. G. Alvin Pierce. His guidance, insight, encouragement, and patience helped me through the rough spots and kept me headed in the right direction throughout this program.

I would also like to thank my thesis committee of Drs. Robin B. Gray and Donald P. Giddens for taking the time to read and evaluate this dissertation. In addition, my thanks go out to Mrs. Ruth Shaw for her expert job of typing.

Since the work done here was primarily experimental, it could never have been started, let alone completed, without the assistance of the people who helped fabricate and assemble the equipment. In this regard, I would like to extend my sincerest thanks to Messrs. Harold Meyer and Dewey Ransom in the Aerospace Shop and to Messrs. John Caudell and Ken Ferrell in the Instrument Lab. I also wish to thank Dr. John Malone, whose work preceded mine, and who taught me a great deal about the equipment and methods that we both used.

Finally, I thank my parents and family for their continued encouragement and support. Their understanding and their confidence in me has been my primary inspiration.

TABLE OF CONTENTS

	Page
ACKNOWLEDGMENTS	ii
LIST OF TABLES	vii
LIST OF FIGURES	viii
SYMBOLS	xii
SUMMARY	xvii

PART I

DYNAMIC STALL

Chapter

I.	INTRODUCTION	2
II.	WIND TUNNEL FACILITY	4
	Gust Generator	
	Gust Generator Calibration	
	Hot-wire Anemometer and Probe	
	Hot-wire Calibration	
III.	AIRFOIL MODEL AND DRIVE MECHANISM	14
	Airfoil Model	
	Model Support System	
	Model Oscillating Mechanism	
	Moment Transducer	
	Acceleration Transducer	

Chapter	Page
IV. ACQUISITION AND REDUCTION OF DATA	23
Acceleration	
Total Moment	
Aerodynamic Moment	
Data Recording	
Flow Parameter Control	
Gust Frequency Control	
Mean Velocity Control	
Model Frequency Control	
Experimental Procedures	
Warm-up and Preliminary Checks	
Still Air Moment	
Constant Freestream Data	
Varying Freestream Data	
Aerodynamic Moment Coefficient	
Angle of Attack	
Pitching Stability	
V. RESULTS AND DISCUSSION	49
Static Moment Data	
Constant and Varying Freestream Moments	
Angle of Attack Effects	
Model Frequency Effects	
Frequency Ratio Effects	
Overall Varying Freestream Effects	
Comparison with Analytical Results	
Analytical Methods	
Discussion	
VI. CONCLUSIONS AND RECOMMENDATIONS	75
Conclusions	
Recommendations	

PART II

UNSTEADY DRAG

Chapter		Page
VII.	INTRODUCTION	79
VIII.	MODIFIED AXIAL GUST GENERATOR	83
	Hot-wire Calibration	
	Gust Generator Calibration	
	Computer Cross-Plotting Program	
	Observations	
IX.	AIRFOIL MODEL AND SUSPENSION SYSTEM	96
	Airfoil Model	
	Suspension System Assembly	
	Force Balance	
	Balance Design	
	Drag Beam	
	Lift Beam	
	Force Balance Calibration	
	Lift Calibration	
	Drag Calibration	
	Lift-Drag Coupling	
X.	DATA ACQUISITION AND REDUCTION	113
	Velocity	
	Static Lift and Drag	
	Unsteady Drag	
	Unsteady Lift	
	Experimental Procedures	
	Aerodynamic Derivatives	
	Lift and Drag Data Reduction	

Chapter	Page
XI. RESULTS AND DISCUSSION	123
Static Lift Data	
Static Drag Data	
Unsteady Drag Derivative	
Quasi-Steady Drag Approximation	
Unsteady Lift Derivative	
Quasi-Steady Lift Approximation	
Potential-Flow Approximation	
XII. CONCLUSIONS AND RECOMMENDATIONS	143
Conclusions	
Recommendations	
APPENDIX	
A. GUST GENERATOR CROSS-PLOT PROGRAM	145
B. FORCE BALANCE DESIGN CALCULATIONS	156
Load Increments	
Drag Bridge Output	
Drag Stiffness	
Lift Bridge Output	
Lift Stiffness	
REFERENCES	165
VITA	170

LIST OF TABLES

Table		Page
1	Gust Generator Operational Curves for the 50% Vanes (0.67-2 Hz)	10
2	Oscillating Airfoil Experimental Flow Conditions . .	50
3	Gust Generator Operational Curves for the 50% Vanes (1-6 Hz)	89
4	Gust Generator Operational Curves for the 60% Vanes (1-6 Hz)	90
5	Gust Generator Operational Curves for the 70% Vanes (1-6 Hz)	91
6	Unsteady Drag Test Conditions	124
7	Unsteady Lift Test Conditions	125
8	Constants for the Force Balance Computations	157

LIST OF FIGURES

Figure		Page
1.	Low Turbulence Wind Tunnel	5
2.	Gust Generator Mechanism	6
3.	Gust Generator Operational Limits (0.67 - 2Hz)	9
4.	Hot-wire Calibration Curve No. 1	13
5.	Main Bearing Assembly	16
6.	Airfoil Oscillating Mechanism (Front View)	17
7.	Airfoil Oscillating Mechanism (Top View)	18
8.	Drive Arm and Drive Rod Assembly	20
9.	Moment Calibration Curve	21
10.	Electronic Data Acquisition Equipment	24
11.	Moment Correction Circuit ($\ddot{\alpha}$, $\dot{\alpha}$)	27
12.	Moment Correction Circuit ($\ddot{\alpha}^2$, $\dot{\alpha}\ddot{\alpha}$)	28
13.	Gust Generator Velocity Curve (R=6)	31
14.	Timing Disk Assembly	33
15.	Analog Shutter Synchronization Circuit	34
16.	Digital Shutter Synchronization Circuit	36
17.	Digital Sequencing	37
18.	Hot-wire Voltage Averaging Circuit	42
19.	Static Moment Curves	51
20.	Static Stall Type as a Function of Reynolds Number and Leading Edge Curvature (from [26])	53
21.	Sequential C_L vs α for Oscillations About 6° at 6 Hz in Constant and 1 Hz Varying Freestreams	55

Figure		Page
22.	Sequential C_m vs. α for Oscillations About 10° at 6 Hz in Constant and 1 Hz Varying Freestreams	56
23.	Sequential C_m vs. α for Oscillations About 14° at 6 Hz in Constant and 1 Hz Varying Freestreams	57
24.	Sequential C_m vs. α for Oscillations About 18° at 6 Hz in Constant and 1 Hz Varying Freestreams	58
25.	Sequential C_m vs. α for Oscillations About 10° at 6 Hz in Constant and 2 Hz Varying Freestreams	59
26.	Sequential C_m vs. α for Oscillations About 10° at 12 Hz in Constant and 2 Hz Varying Freestreams	60
27.	Sequential C_m vs. α for Oscillations About 10° at 12 Hz in Constant and 1 Hz Varying Freestreams	61
28.	Analytical and Experimental C_m vs. α for Oscillations About 6° at 6 Hz in Constant and 1 Hz Varying Freestreams	67
29.	Analytical and Experimental C_m vs. α for Oscillations About 10° at 6 Hz in Constant and 1 Hz Varying Freestreams	68
30.	Analytical and Experimental C_m vs. α for Oscillations About 14° at 6 Hz in Constant and 1 Hz Varying Freestreams	69
31.	Analytical and Experimental C_m vs. α for Oscillations About 18° at 6 Hz in Constant and 1 Hz Varying Freestreams	70

Figure		Page
32.	Analytical and Experimental C_m vs. α for Oscillations About 10° at 6 Hz in Constant and 2 Hz Varying Freestreams	71
33.	Analytical and Experimental C_m vs. α for Oscillations About 10° at 12 Hz in Constant and 2 Hz Varying Freestreams	72
34.	Analytical and Experimental C_m vs. α for Oscillations About 10° at 12 Hz in Constant and 1 Hz Varying Freestreams	73
35.	Hot-wire Calibration Curve No. 2	84
36.	Hot-wire Calibration Curve No. 3	85
37.	Equipment for the Gust Generator Calibration	87
38.	Gust Generator Operational Limits (1-6 Hz)	92
39.	Operational Curves for the 70% Vanes (1-6 Hz)	94
40.	Raw Data Curves for the 70% Vanes (1-6 Hz)	95
41.	Stationary Model Suspension System	98
42.	Force Balance Configuration and Strain Gage Bridge Circuits	100
43.	Lift Force Calibration Stand	103
44.	Lift Force Calibration Curves	105
45.	Drag Force Calibration Stand	106
46.	Drag Force Calibration Curves	107
47.	Extended Drag Force Calibration Curves	109
48.	Lift-Drag Coupling Curves	110
49.	Electronics for the Unsteady Drag Measurements	116
50.	Example of Unsteady Drag Data	122
51.	Static Lift Curves	126

Figure		Page
52.	Static Drag Curves	128
53.	Drag Derivative Variations with Reduced Frequency (Real Part)	130
54.	Drag Derivative Variations with Reduced Frequency (Imaginary Part)	131
55.	Drag Derivative Variations with Angle of Attack (Real Part)	132
56.	Drag Derivative Variations with Angle of Attack (Imaginary Part)	133
57.	Lift Derivative Variations with Reduced Frequency	137
58.	Lift Derivative Variations with Angle of Attack	138
59.	Force Balance Drag Beam	159
60.	Force Balance Lift Beam	162

SYMBOLS

Roman Symbols

b	airfoil model semichord (ft)
$C(k)$	Theodorsen's function
C_D	steady drag coefficient
\bar{C}_D	magnitude of the quasi-steady drag coefficient, defined in Equation (27)
C_d	unsteady drag coefficient
\bar{C}_d	magnitude of the unsteady drag coefficient
C_L	steady lift coefficient
\bar{C}_L	magnitude of the quasi-steady lift coefficient, defined in Equation (35)
C_L^*	unsteady, potential-flow lift coefficient, defined in Equation (39)
C_l	unsteady lift coefficient
\bar{C}_l	magnitude of the unsteady lift coefficient
c	airfoil model chord (ft)
D	drag force (lb)
ΔD	drag force increment (lb)
d	unsteady drag force (lb)
\bar{d}	magnitude of the unsteady drag force (lb)
E	electromotive force (volts)
E_{Al}	Young's modulus of elasticity for aluminum (lb/in ²)

Roman Symbols

e	logarithmic constant (2.71828182 ...)
e_i	strain gage bridge exciting voltage (volts)
Δe_d	change in the drag bridge output (volts)
Δe_l	change in the lift bridge output (volts)
$F(k)$	real part of Theodorsen's function
F_d	gage factor for the drag bridge strain gages
F_l	gage factor for the lift bridge strain gages
f_d	natural frequency of the airfoil model and suspension system in the drag plane (Hz)
f_l	natural frequency of the airfoil model and suspension system in the lift plane (Hz)
$G(k)$	imaginary part of Theodorsen's function
h_d	drag beam thickness (in)
h_l	lift beam thickness (in)
I	moment of inertia (in ⁴)
i	imaginary constant ($\sqrt{-1}$)
K_d	stiffness of the drag beam (lb/in)
K_{ds}	stiffness of the suspension system in the drag plane (lb/in)
K_l	stiffness of the lift beam (lb/in)
K_{ls}	stiffness of the suspension system in the lift plane (lb/in)
k	reduced frequency
k_v	reduced frequency of the pulsating freestream with respect to semichord and mean velocity, $\omega_v b/V_o$

Roman Symbols

L	lift force (lb)
ΔL	lift force increment (lb)
l	unsteady lift force (lb)
M	total pitching moment (in-lb)
M_d	drag beam moment (in-lb)
M_l	lift beam moment (in-lb)
m_s	sprung mass of the airfoil model and suspension system (lb-sec ² /in)
R	ratio of model frequency to gust frequency, ω_w/ω_v
Re	Reynolds number with respect to semichord, Vb/ν
s	airfoil model span (ft)
s_d	drag beam length (in)
s_l	lift beam length (in)
t	time (sec)
t_1	time delay between the timing circuit pulse initiation and the sweep triggering (sec)
t_2	time delay between the timing circuit pulse initiation and shut-off (sec)
V	wind tunnel test-section velocity (ft/sec)
V_0	mean velocity of the pulsating freestream (ft/sec)
V_1	gust amplitude of the pulsating freestream (ft/sec)
V_r	mean velocity of the pulsating freestream during one model pitching cycle (ft/sec)
V_∞	velocity of the constant freestream (ft/sec)
w_d	drag beam width (in)
w_l	lift beam width (in)

Roman Symbols

x	non-dimensional in-plane coordinate, defined in Equation (9)
\bar{x}	magnitude of the non-dimensional in-plane coordinate
x^*	horizontal beam coordinate (in), defined in Figures 59 and 60
x_d^*	drag strain gage location (in)
x_l^*	lift strain gage location (in)

Greek Symbols

α	angle of attack (deg)
α_o	mean angle of attack (deg)
α_l	angle of attack amplitude (deg)
α_r	angle of attack (rad)
$\dot{\alpha}$	angular pitching velocity (deg/sec)
$\ddot{\alpha}$	angular pitching acceleration (deg/sec ²)
δ_d	drag beam deflection (in/lb)
δ_l	lift beam deflection (in/lb)
ϵ_d	drag beam strain (in/in)
$\Delta\epsilon_d$	change in drag beam strain (in/in)
ϵ_l	lift beam strain (in/in)
ν	kinematic viscosity (ft ² /sec)
ξ	in-plane coordinate (ft), positive in the direction of the advancing blade
$\bar{\xi}$	magnitude of the in-plane displacement (ft)
$\dot{\xi}$	rate of in-plane displacement (ft/sec)
π	pi (3.141592653 ...)
ρ	density of air (lb-sec ² /ft ⁴)

Greek Symbols

τ	airfoil model thickness ratio
ϕ	gust velocity time scale (deg), defined in Figure 13
ϕ_m	mean ϕ during one model cycle (deg)
ω_v	frequency of the pulsating freestream (Hz)
ω_α	frequency of the pitching airfoil model (Hz)

Subscripts

I	imaginary part of a complex quantity
R	real part of a complex quantity

SUMMARY

The Georgia Tech Low Turbulence Wind Tunnel, equipped with an axial gust generator, was employed to simulate the aerodynamic environment of a helicopter rotor blade for two different phenomena. It was used to study the dynamic stall of a pitching blade, and the in-plane oscillations of a rotor blade on a hovering helicopter. The objectives of this investigation were to find out to what extent streamwise, simple harmonic velocity perturbations in the freestream affect dynamic stall and unsteady drag.

The study of dynamic stall involved making measurements of the aerodynamic moment on a two-dimensional, pitching rotor blade model in both constant and pulsating airstreams. Using an operational analog computer to perform on-line data reduction, plots of moment coefficient versus angle of attack were obtained for single pitching cycles under various flow conditions.

The data taken in the harmonically varying freestream were then compared to constant freestream data, and to the results of two analytical methods; one based on potential flow theory, and the other an empirical method. These comparisons showed that, under the conditions tested, the velocity perturbations had a significant effect on the pitching moment which could not be consistently predicted by the analytical methods, but had no drastic effect on the blade stability.

A two-dimensional blade model at constant, small angles of attack was used to simulate in-plane oscillations. A strain gage force balance

was used to obtain the unsteady lift and drag, which were displayed in conjunction with the velocity perturbations. By relating these velocity perturbations to an equivalent in-plane displacement, the complex lift and drag derivatives with respect to the equivalent displacement were obtained.

The properties of these derivatives with respect to reduced frequency and angle of attack were compared to derivatives derived from steady data. In addition, the lift derivative was compared to a derivative from potential flow theory. It was found that the unsteady lift and drag could not be accurately predicted from the quasi-steady approximation. However, the potential flow result was a more reasonable approximation to the unsteady lift.

PART I

DYNAMIC STALL

CHAPTER I

INTRODUCTION

One aerodynamic phenomenon that can have a great effect on the performance of helicopters, as well as compressors and fixed-wing aircraft, is dynamic stall. In the case of a helicopter, dynamic stall not only limits the forward flight speed of the aircraft, but also may cause an aeroelastic instability known as stall flutter. This instability occurs when a blade, oscillating in pitch, draws energy from its surroundings, and is a result of the hysteretic nature of the pitching moment on the blade surface.

A great deal of work has been done in an attempt to get a firm understanding of the development, nature, and effects of dynamic stall [1-16]. Based on these and other investigations, researchers began trying to predict the onset of and loads due to dynamic stall. Both theoretical and empirical techniques were used, with varying degrees of success [12,17-24]. The one feature that all of these efforts have in common is that the airfoil is oscillating in a freestream which has a constant velocity.

When a helicopter is in forward flight, the velocity that the rotor blades see is the sum of a mean velocity due to the rotor rotation, and a perturbation velocity due to the forward flight speed. In order to investigate what effect this varying velocity has on the stability of blade pitch oscillations, Malone [25] set up an axial gust generator

to impress simple harmonic velocity perturbations on a mean freestream velocity. The conclusion he reached from his investigation was that the velocity variations can have a destabilizing effect on blade oscillations at large mean angles of attack.

Extending the scope of Malone's work, the effect of the pulsating freestream was investigated in various angle of attack regimes. In particular, the regions of interest were: maximum and mean angles below the static stall angle, minimum and mean angles above stall, mean angle below stall and maximum angle above, and mean angle above stall and minimum angle below. In addition, the effects of model oscillation frequency and frequency ratio were investigated for the most interesting of the angle of attack regimes above.

CHAPTER II

WIND TUNNEL FACILITY

This investigation was carried out in the Georgia Tech Low Turbulence Wind Tunnel (Figure 1). The wind tunnel is of the closed-jet, open-circuit type, and has a maximum airspeed of 80 feet per second in the test section. Downstream of the fan, which is located at the upstream entrance, and upstream of the converging nozzle is a honeycomb screen which serves to straighten the flow and to limit the size of the turbulent eddies.

One sidewall of the test-section is fitted with screw-jacks, so that the test-section contour can be varied. For the purposes of this study, the sidewalls were made to be parallel. This made the cross-section of the test-section a square, 42 inches on a side.

Gust Generator

At the downstream exit of the wind tunnel is located the gust generator mechanism (Figure 2). The mechanism consists of four component systems: the drive motor and controls, the drive-side gear box, the idle-side assembly, and the vanes.

The power source for the gust generator is a Wood's, one horsepower, SCR motor. A Wood's Model U-100 ULTRACON drive control regulates the motor torque and speed. A pulley and belt drive transfers the rotational motion of the motor shaft to the drive-side gear box.

Power is transmitted from the motor to the vanes through the

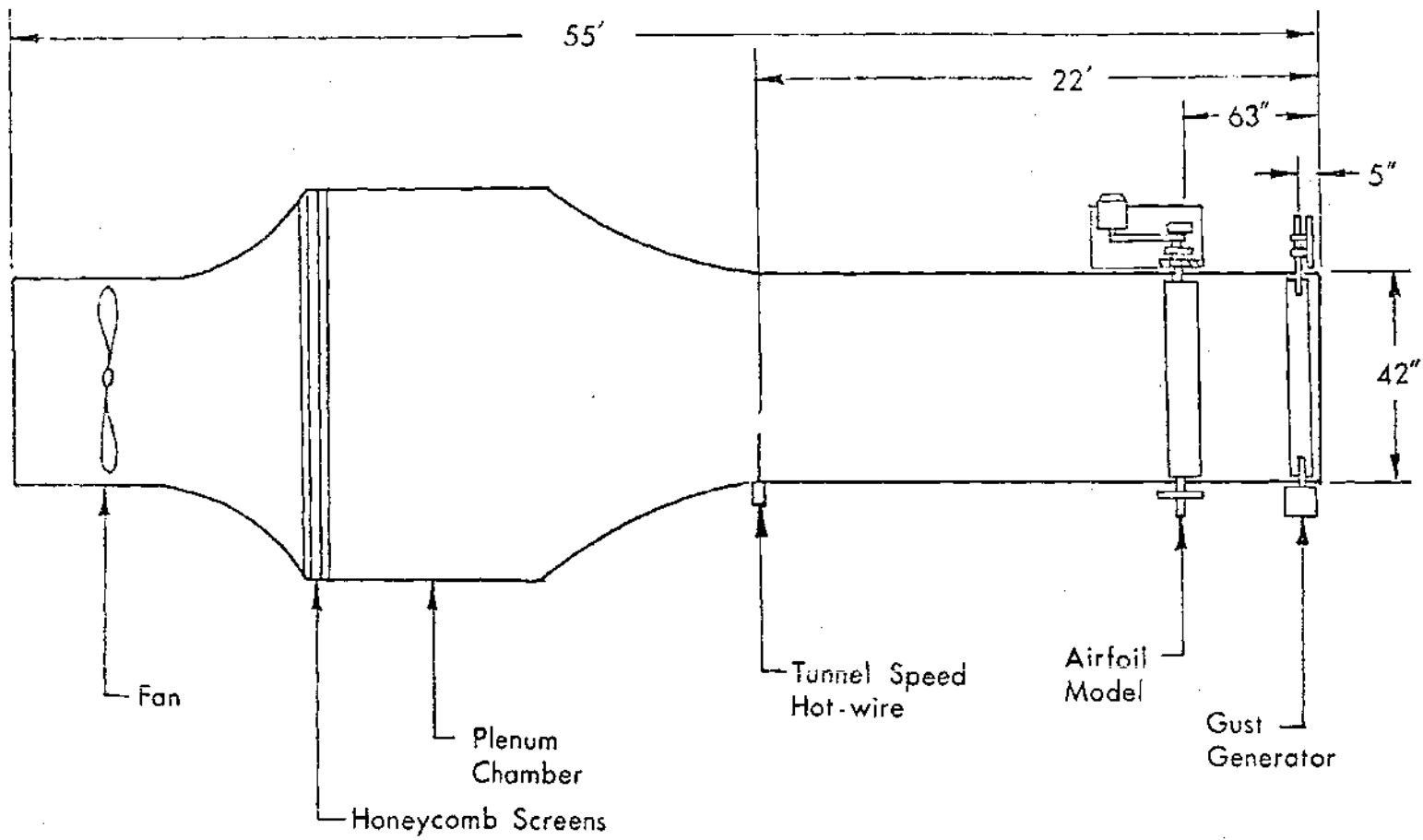


Figure 1. Low Turbulence Wind Tunnel

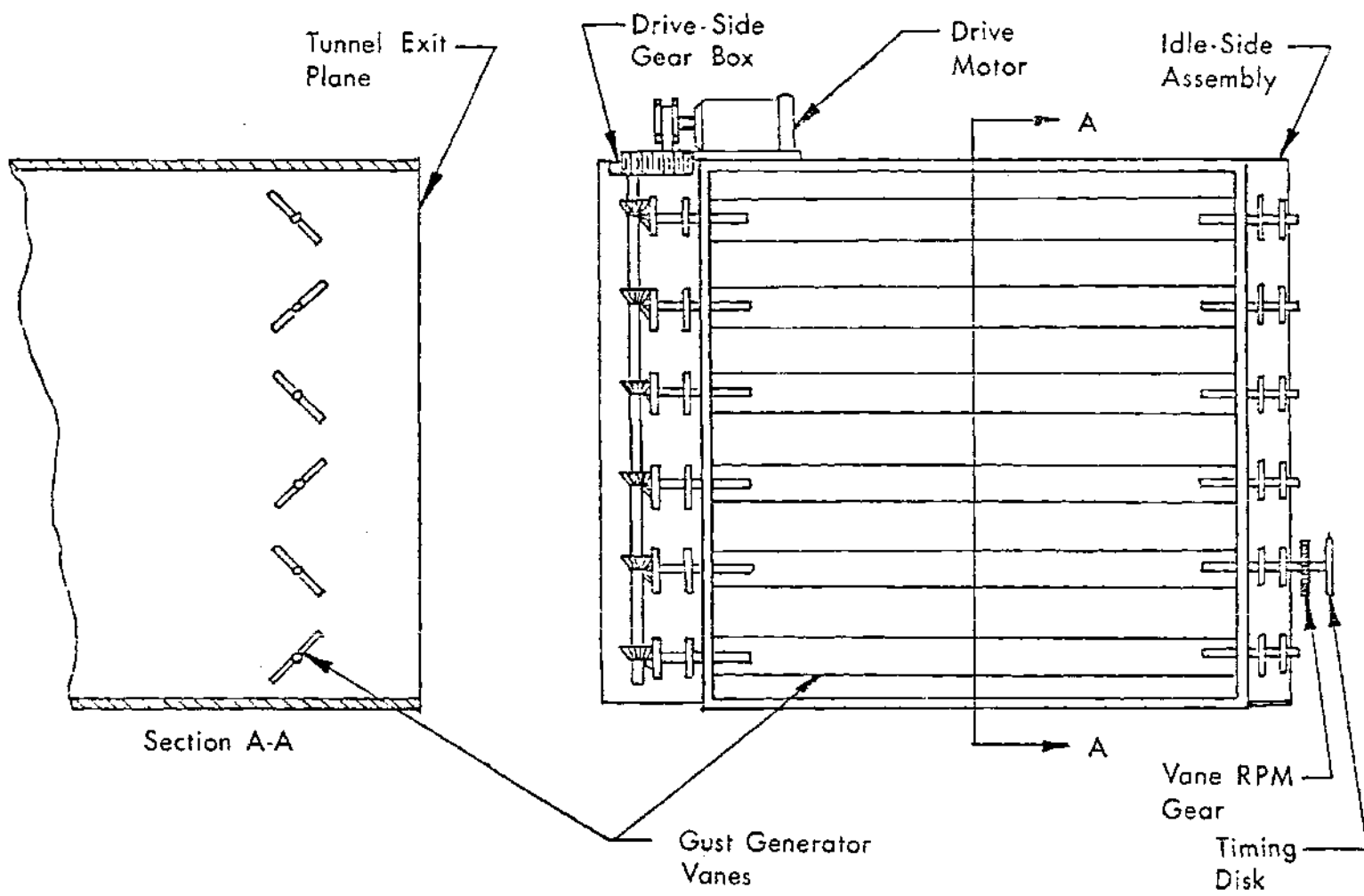


Figure 2. Gust Generator Mechanism

drive-side gear box. The gear box contains a worm gear, a vertical shaft, and a series of bevel gears and slotted shafts set in pillow blocks. Horizontal rotation from the motor is geared down and changed to vertical rotation through the worm gear. The vertical shaft transfers the rotation to the vanes through the bevel gears, which change the vertical rotation back to horizontal rotation. Six slotted shafts serve as points of attachment for the vanes.

On the other side of the wind tunnel is the idle-side assembly. The main components of this assembly are six slotted shafts, each set in a pair of pillow blocks. In addition, on the second shaft from the bottom are fixed the vane RPM gear and the timing disk. The vane RPM gear is a 60-tooth gear which, when used in conjunction with a magnetic pickup, filter, and electronic counter, allows the rotational rate of the vanes to be determined. The timing disk, which is an aluminum disk with a steel stud set into its edge, is used together with a magnetic pickup to give a voltage pulse at a specific point in the vane rotation.

The vanes for the gust generator are made from 1/4 inch thick aluminum, 42 inches long, and of different widths, depending on the percent blockage desired. At each end, along the centerline, are holes through which the vanes are bolted to the slotted shafts which protrude into the wind tunnel. Vane widths are designated by how much of the wind tunnel exit area is blocked off when the vanes are in a vertical position. For example, the set of 70 percent vanes blocks off 70 percent of the tunnel exit area. In order to minimize flow angularity in the test section, adjacent vanes rotate in opposite directions.

Gust Generator Calibration

This being an extension of the work done by Malone [25], the identical gust generator set-up and calibration curves were used. Figure 3 shows the operational limits of the gust generator for the 30, 50, and 70 percent vanes between 0.67 and 2 Hertz. It should be pointed out that as the gust frequency increases, for a constant mean velocity, the gust amplitude decreases. Thus, the upper limit gust amplitude curve for each set of vanes represents a frequency of 0.67 Hertz, while the lower limit represents a frequency of 2 Hertz. The upper and lower limits on mean velocity are determined by where the waveform begins to deteriorate.

Since there is no point where any of the operational limits overlap, it is impossible to vary one parameter (gust frequency, amplitude, or mean velocity) and hold the other two constant. With this in mind, and wanting to retain only a few significant variables, it was decided to select one mean velocity and one set of vanes for all the tests. Using the 50 percent vanes and a mean velocity of 42.50 feet per second, gust amplitudes of 7.53 and 3.04 feet per second were obtained at 1 and 2 Hertz respectively (Table 1).

Hot-wire Anemometer and Probe

Velocity measurements in the wind tunnel were made throughout these tests with a hot-wire anemometer. This means of measurement was selected for its accuracy, ease of use, and voltage output. The model used was a Flow Corporation Model 900-A constant-temperature hot-wire anemometer.

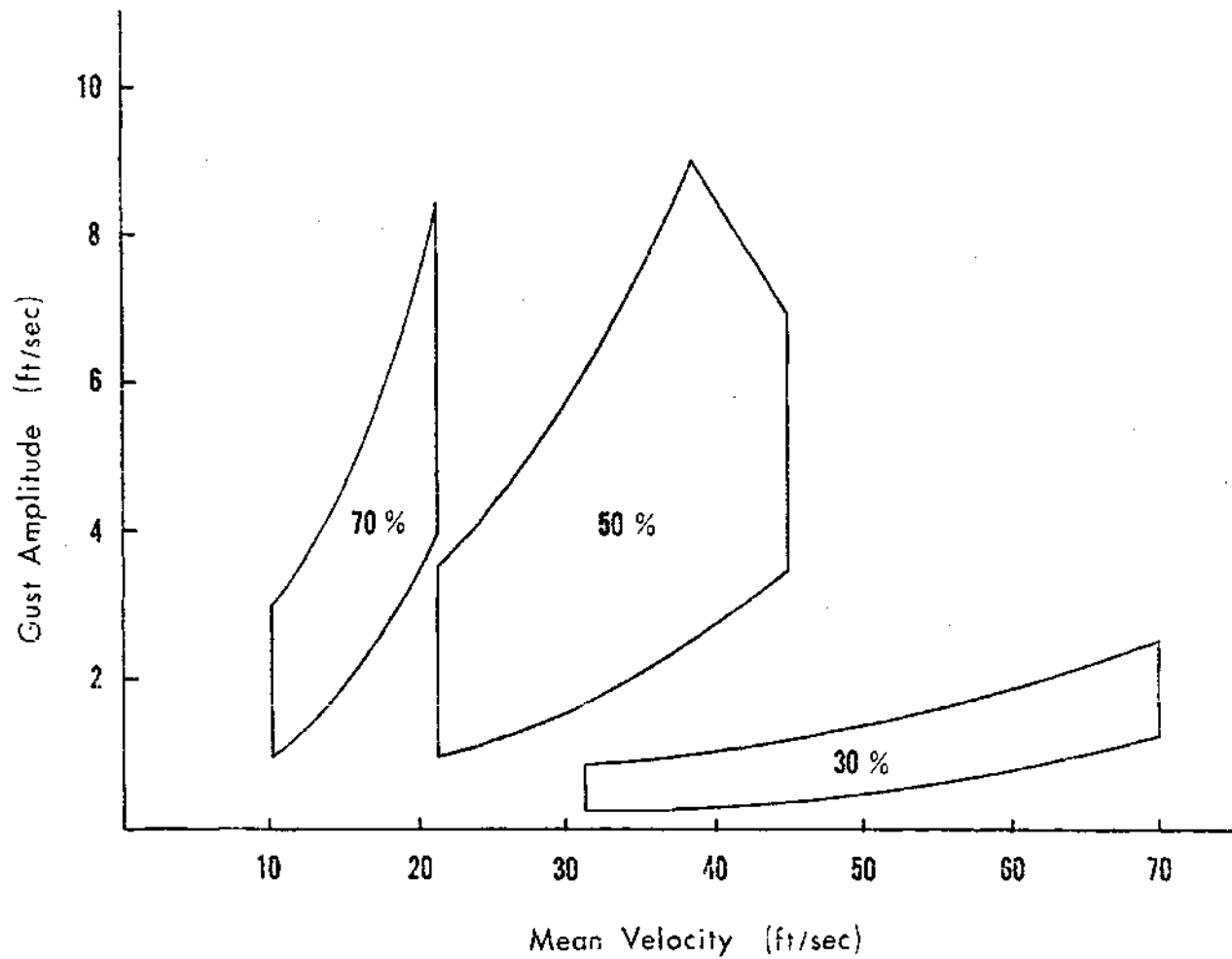


Figure 3. Gust Generator Operational Limits (0.67 - 2 Hz)

Table 1. Gust Generator Operational Curves for
the 50% Vanes (0.67 - 2 Hertz)

ω_v (Hz)	Gust Amplitude (fps)
0.67	$V_1 = - 2.0180 + .1900 V_o + .0024 V_o^2$
0.83	$V_1 = - 1.6940 + .1542 V_o + .0022 V_o^2$
1.00	$V_1 = - 1.3440 + .1196 V_o + .0021 V_o^2$
1.17	$V_1 = - 0.9690 + .0865 V_o + .0020 V_o^2$
1.33	$V_1 = - 0.5685 + .0545 V_o + .0020 V_o^2$
1.50	$V_1 = - 0.1425 + .0238 V_o + .0020 V_o^2$
1.67	$V_1 = 0.3089 - .0056 V_o + .0021 V_o^2$
1.83	$V_1 = 0.7858 - .0337 V_o + .0022 V_o^2$
2.00	$V_1 = 1.2880 - .0606 V_o + .0024 V_o^2$

The probe, also made by Flow Corporation, was 14 inches long and 1/4 inch in diameter. A piece of 0.00035 inch diameter tungsten wire, welded to the probe tip, served as the sensing element. With this arrangement, it was possible to measure velocities as low as two feet per second.

Hot-wire Calibration

The calibration of the hot-wire was done in the wind tunnel using the anemometer and probe, a manometer, and a pitot-static probe. The hot-wire probe was placed in the position where it was to be during the tests, while the pitot-static probe was located in a downstream position. In these locations, neither probe interfered with the other. With the wind off, the manometer and pitot probe were connected, and the manometer adjusted to read a column height of zero. Then, the hot-wire probe element was oriented perpendicular to the flow direction by turning the wind tunnel on and rotating the probe until the maximum output was obtained.

For constant wind tunnel velocities between 5 and 70 feet per second, the manometer height and hot-wire voltage were recorded. In addition, the average stagnation temperature and stagnation pressure were determined over the duration of the calibration run.

The reduction and curve fitting for this data was done on a digital computer. The program converted manometer column height to velocity using the incompressible Bernoulli equation, then fit both linear and quadratic curves to the data by a least squares approximation. Using the standard deviation of each curve, the better fit was selected

as the calibration curve. The curve fit used throughout this part of the investigation is shown in Figure 4.

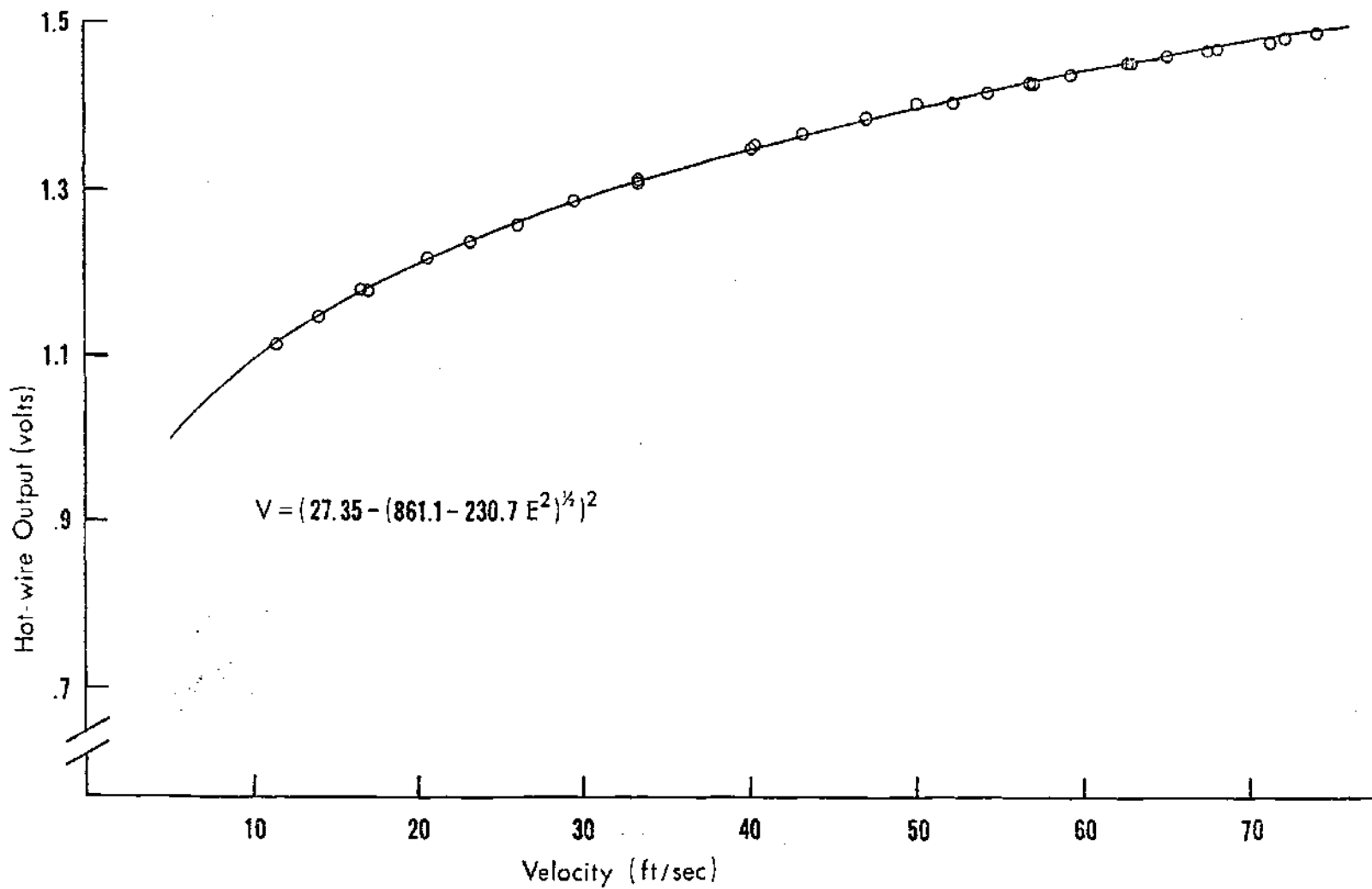


Figure 4. Hot-wire Calibration Curve No. 1

CHAPTER III

AIRFOIL MODEL AND DRIVE MECHANISM

The following paragraphs briefly describe the airfoil model, the pitch drive mechanism, and the transducers used in this investigation. A more detailed description of the design and construction of the equipment can be found in Malone's thesis [25].

Airfoil Model

The model used for these tests was constructed from balsa blocks, which were laminated together and bonded to a $7/8$ inch diameter steel spar. The blocks were shaped into a 9 inch chord, NACA 0012 contour that had a 42 inch span. The spar was located at the quarter-chord. After the shaping was complete, the model surface was sealed and painted.

To mass balance the model, two rectangular, brass bars were attached to the spar. The locations for the bars were such that when the model was installed in the wind tunnel, the bars were outside the test-section walls. Thus, the airflow inside the tunnel was not disturbed.

At a point 2.5 inches aft of the axis of rotation, an accelerometer was placed. It was located near the edge of the model, next to the wall of the test-section. In this location, the disturbances created by the accelerometer would have a minimum effect on the overall flow pattern.

Model Support System

Due to the requirement that all supports be free of the test-section walls, both supports for the model suspension system were attached to the external wind tunnel structure. On the side where the oscillating mechanism was set up, the support structure consisted of a base plate bolted to the tunnel with steel angles. On the other side, the support was a trapezoidal frame constructed out of steel angles.

As for the model suspension system, the model was supported by the main bearing assemblies (Figure 5), which were located outside and on either side of the test section. The center arm on each assembly was pinned to the base at one end and fixed at the other. Strain gage bridges were bonded to the center arm at the points where the arm had been milled down. This lift measuring arrangement was, however, not used in the course of this investigation.

Model Oscillating Mechanism

The oscillating mechanism for the model (Figures 6 and 7) was designed so that mean angle of attack, amplitude of oscillation, and frequency could all be varied. The driving element for this system was an interchangeable eccentric crank.

Driving the mechanism was a Minarik, 1/2 horsepower, shunt motor. A Model WTF-73, Minarik Tachometer Generator regulated the motor speed. The oscillatory frequency was measured in the same manner as the vane frequency, using a 60-tooth gear, magnetic pickup, low-pass filter, and electronic counter.

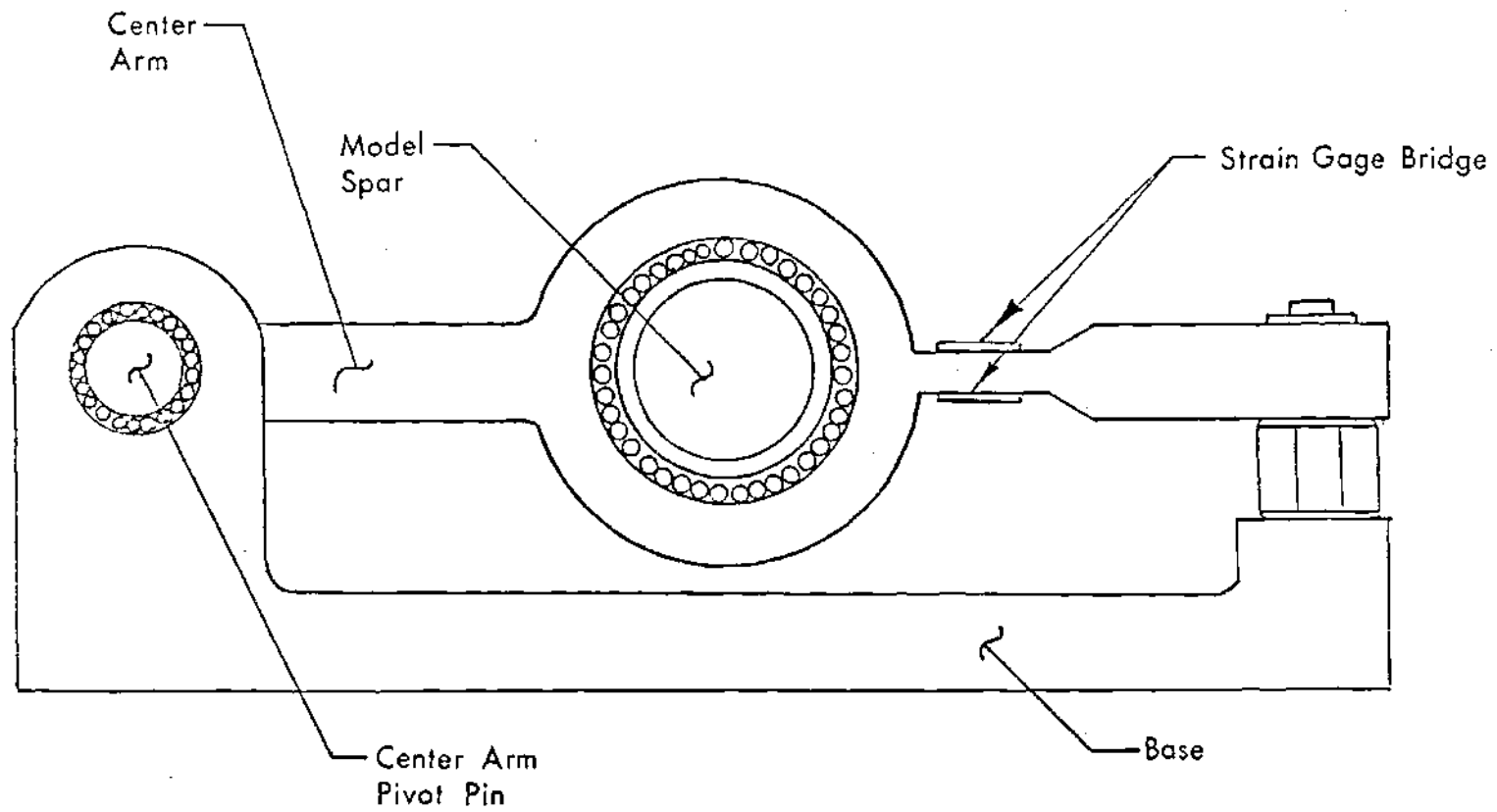


Figure 5. Main Bearing Assembly

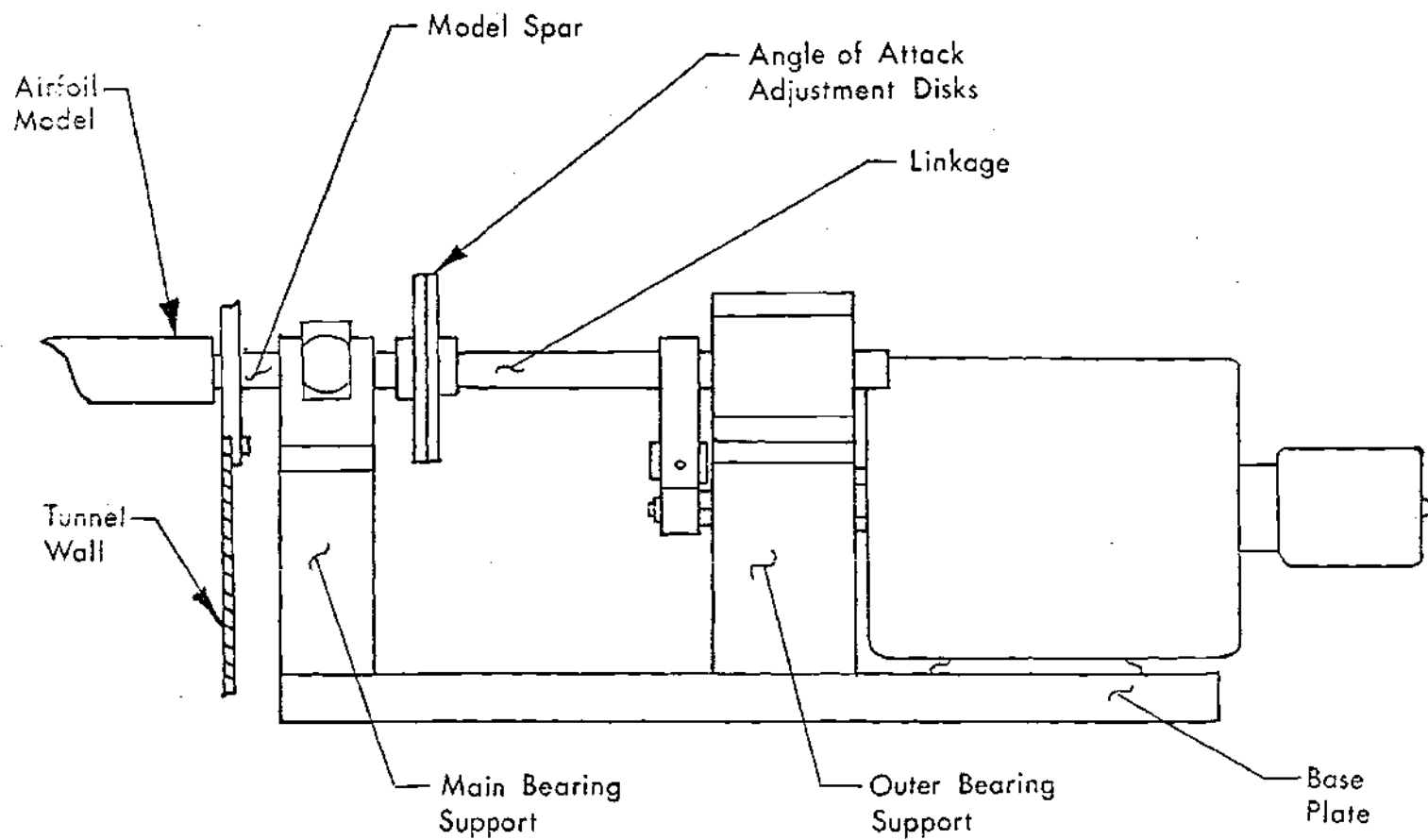


Figure 6. Airfoil Oscillating Mechanism (Front View)

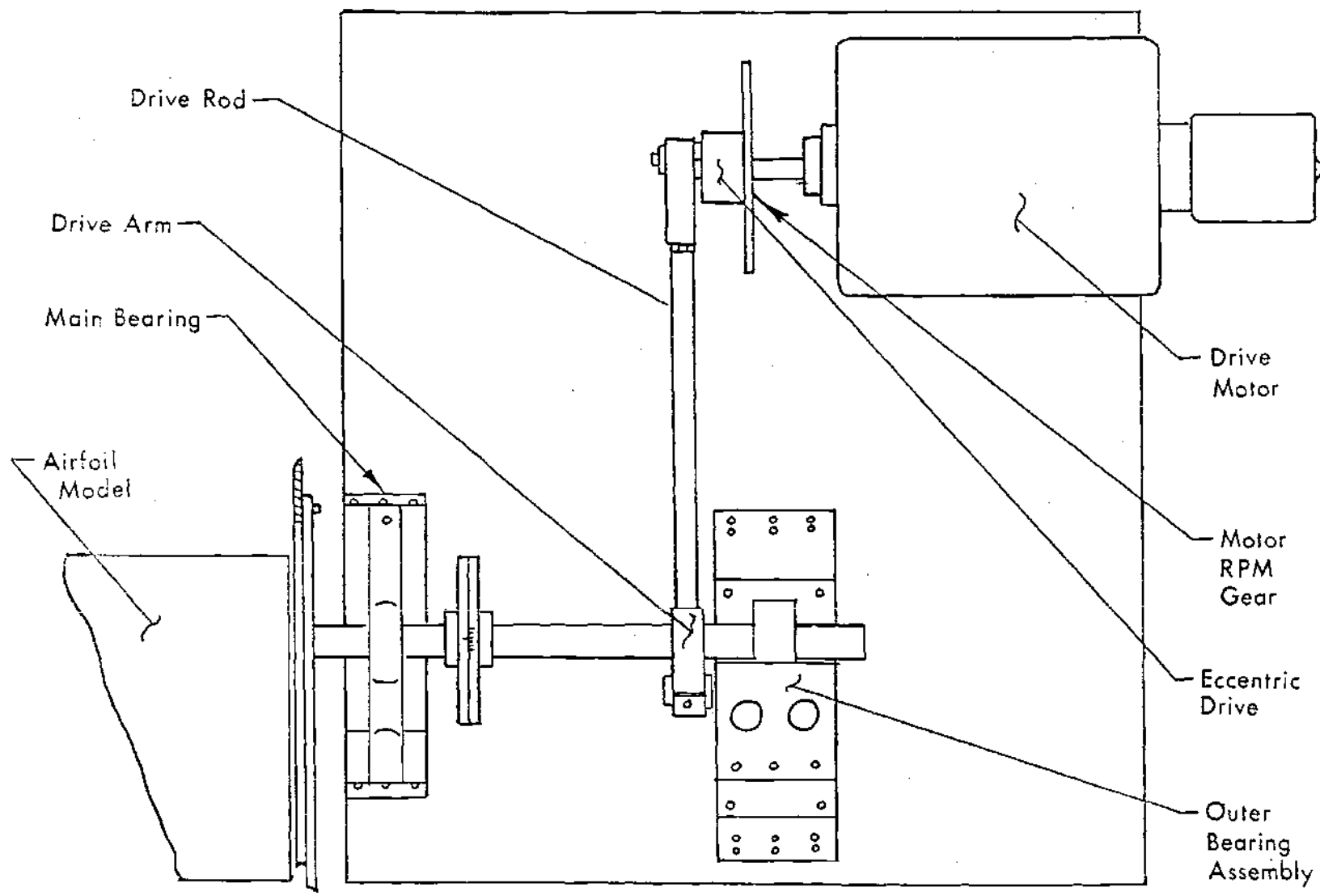


Figure 7. Airfoil Oscillating Mechanism (Top View)

Transforming the rotational motion of the motor shaft into the oscillatory motion of the model was the function of the eccentric. It was fixed to the motor shaft, and had an off-center crank pin to which the drive rod was connected. The distance that the crank pin was away from the center determined the amplitude of oscillation. Although four different eccentrics were available ($\pm 2^\circ$, $\pm 4^\circ$, $\pm 6^\circ$, $\pm 8^\circ$), only the $\pm 4^\circ$ crank was used.

The drive arm and drive rod assembly (Figure 8) transferred the motion of the eccentric to the model spar. As the drive arm oscillated the linkage shaft, the motion was transmitted to the model spar through the angle of attack adjustment disks. By changing the relative positions of the disks, the mean angle of attack of the model could be varied.

Moment Transducer

A strain gage bridge was bonded onto the drive arm (Figure 8). This bridge put out a signal proportional to the total moment on the model. The calibration curve for the bridge, as determined by Malone [25], is shown in Figure 9. Before proceeding with the experiments, this curve was spot-checked for accuracy and was found to be accurate throughout its range.

Acceleration Transducer

Since no measurements of acceleration were required in this investigation, the B & K Model No. 306 accelerometer that was attached to the model was not calibrated. Its signal was used, however, in the synthesis of an angle of attack scale, and to cancel out the output of the moment strain bridge as the model oscillated in still air. These

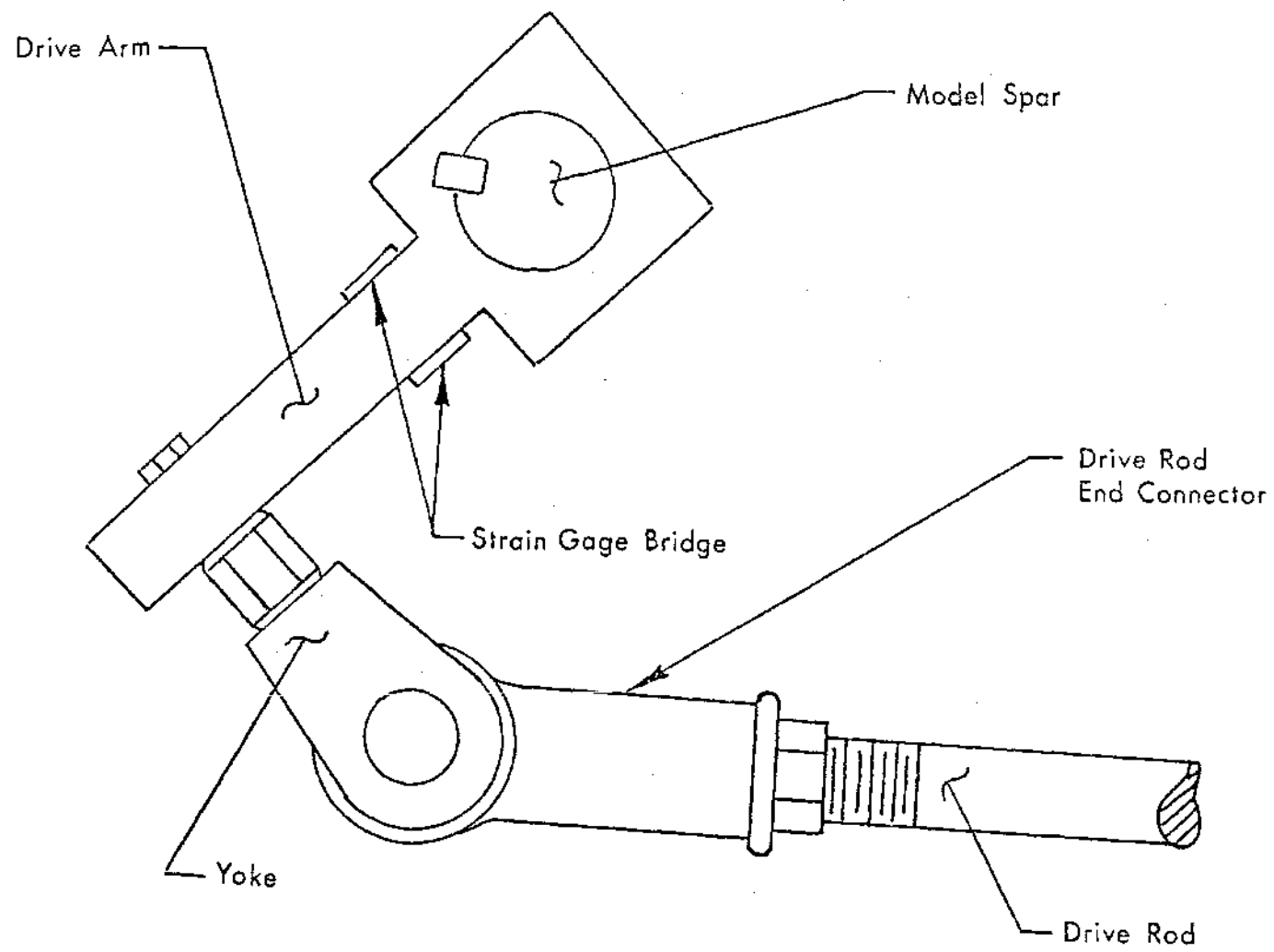


Figure 8. Drive Arm and Drive Rod Assembly

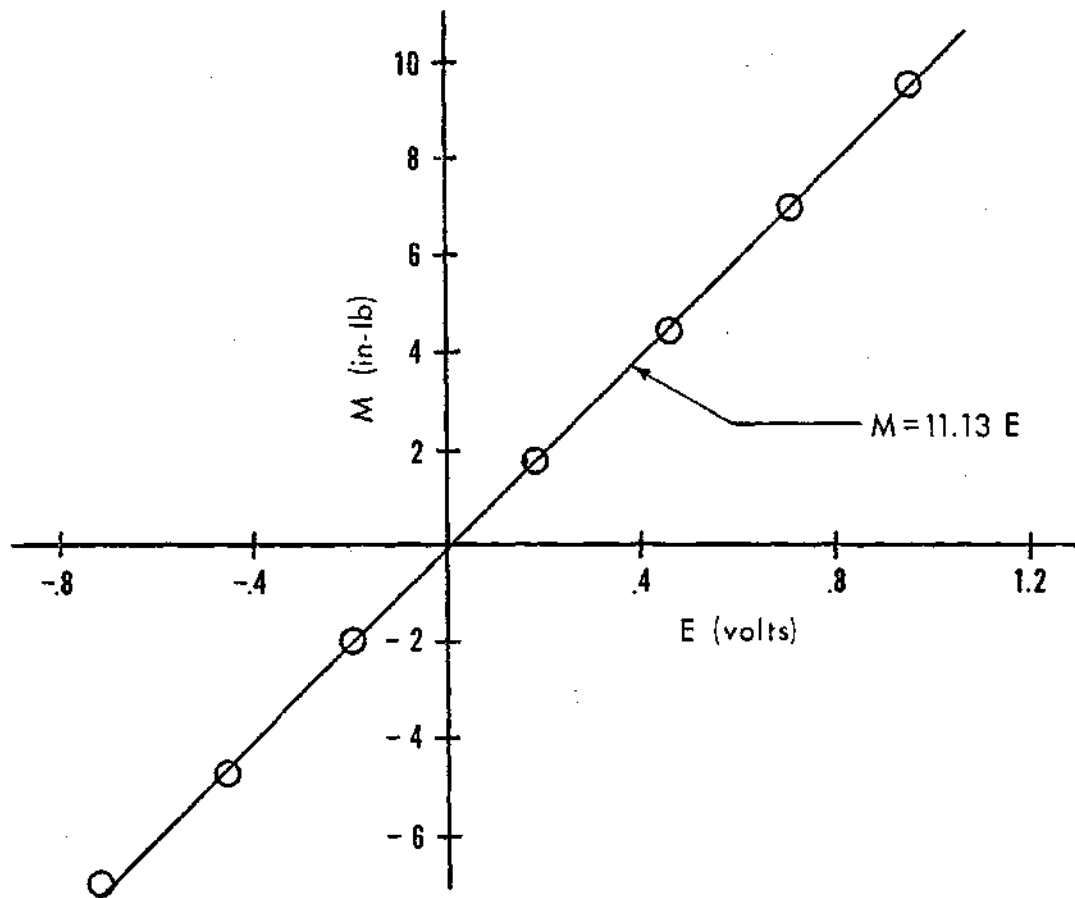


Figure 9. Moment Calibration Curve

procedures will be explained in detail in a later section.

CHAPTER IV

ACQUISITION AND REDUCTION OF DATA

Due to the nature and quantity of the data to be obtained, any decrease in the time and effort required to acquire and reduce this data would be most advantageous. Using the equipment and techniques described in this chapter, it was possible to reduce the data on line, as the data were being taken. Because of this, a great deal of time was saved since inconsistencies in the data could be seen immediately and the test repeated on the spot, and since post-acquisition reducing was virtually eliminated.

Acceleration

The acceleration signal used in this investigation came from the accelerometer that was attached to the model. This signal was amplified by an M-B Model N400 Zero Drive amplifier, after having been conditioned by an M-B voltage line driver (Figure 10).

It was then necessary to filter this signal to eliminate high-frequency noise. Sending it through one channel of a Krohn-Hite, Model 3343, low-pass filter, set to pass only frequencies below 20 Hertz, eliminated the noise. However, in spite of the fact that the moment signal was passed through the other channel using the same settings, there was a phase shift between the two signals. Thus, a Spectral Dynamics SD101B Dynamic Analyzer fitted with a 10 Hertz bandwidth filter was added to the circuit. The use of this tracking filter made it

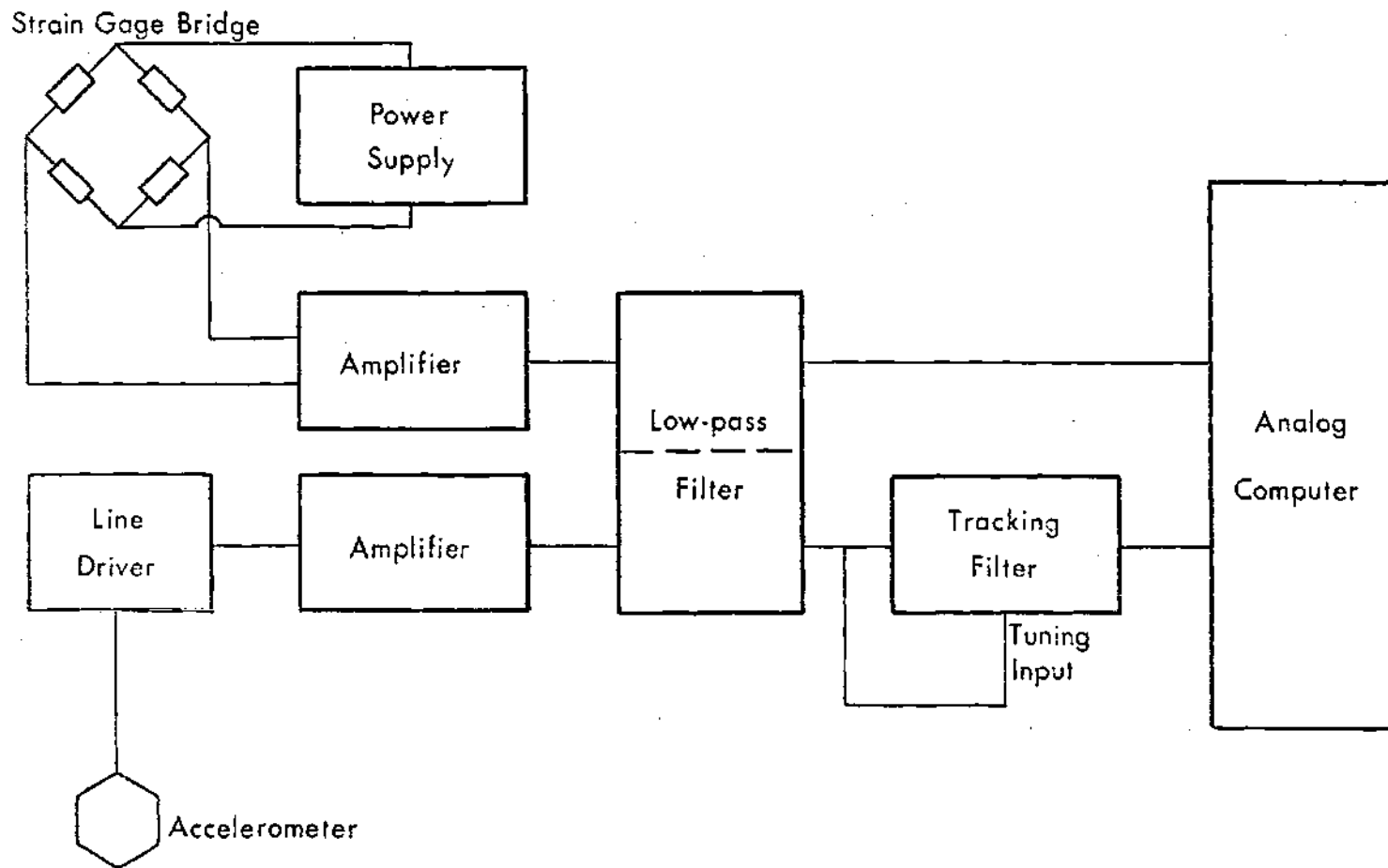


Figure 10. Electronic Data Acquisition Equipment

possible to have a phase adjustment in the circuit.

From the tracking filter, the acceleration signal, now filtered, was put into the analog computer. There, it was used to convert the total moment into aerodynamic moment, and to synthesize an angle of attack scale.

Total Moment

The complete reduction of the moment data was accomplished as it was being taken, by electronic means (Figure 10). From the strain gage bridge, the moment signal was amplified by a factor of 1000 by a Weff, Type 122, DC amplifier. To eliminate the high-frequency noise in the signal, it was passed through the other channel of the Krohn-Hite, Model 3343, low-pass filter. This channel was also set to pass only those frequencies below 20 Hertz, so that attenuation of the signal would be negligible.

The signal was then sent into the analog computer where, by subtracting off unwanted moment contributions the total moment was converted to aerodynamic moment.

Aerodynamic Moment

Before the moment data could be recorded, all components of the moment not due to aerodynamics had to be eliminated. This was accomplished by using an Electronics Associates, Inc., TR-48 operational analog computer, with its DES-30 parallel logic unit. The process consisted essentially of subtracting the proper proportions of inertial moment, damping moment, and other, higher-order contributions to the moment, with the model oscillating in still air.

The process which converted the total moment signal to aerodynamic moment is shown in Figures 11 and 12. The incoming data arrives via trunk 3. In amplifier A10, a correction is made, through potentiometer P10, which forces the signal from the stationary model in still air to zero. Then, using A08 and P11, the voltage input is converted to inch-pounds (calibration constant = 11.13 in-lb/volt). Finally, the total moment, in inch-pounds, is fed into A09, where the correction factors are applied.

The first correction to be made was the inertial correction. Since the inertial moment is proportional to the angular acceleration, it was a simple matter to get the proper constant using P25 and the gains of A20 and A09.

Getting the damping correction turned out to be somewhat more difficult. The damping moment is, of course, proportional to angular velocity, which is the integral of angular acceleration. Since open-loop integration is normally an unstable operation, it was necessary to use the integration stabilization circuit that was developed in the course of Malone's work [25].

The stabilization circuit is basically a feedback circuit in which the sum of the relative maxima and minima of the integrated signal are fed back into the integrator. In this case, the angular velocity out of integrator I11 provides the inputs for track-and-store units TS22, TS23, TS34, and TS35. Comparator C21 is driven by the angular acceleration from trunk 2, which is 90° out of phase with the angular velocity. The output of C21 controls TS22 and TS23 which put out the relative maxima, and TS34 and TS35 which put out the relative minima. The

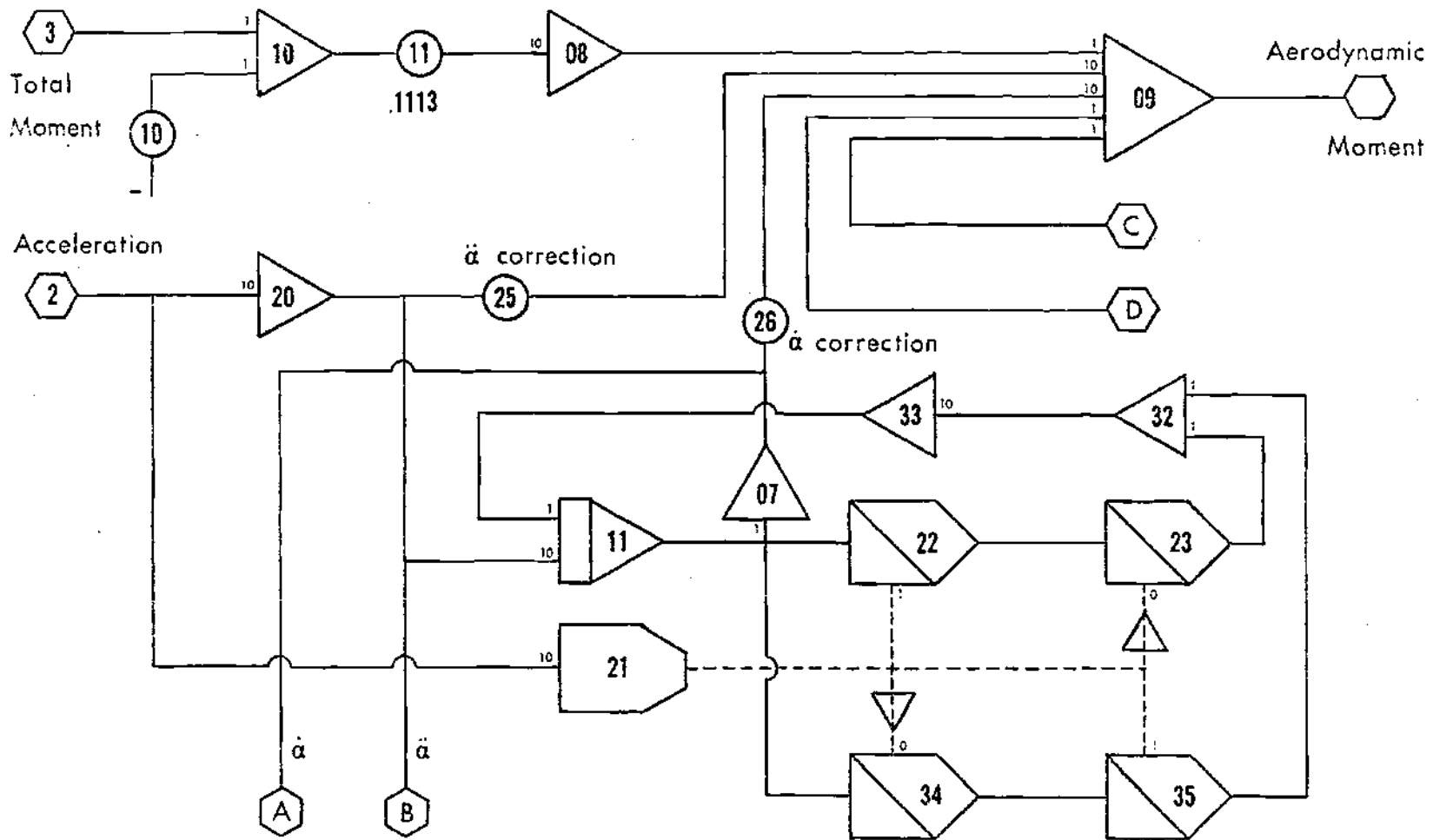


Figure 11. Moment Correction Circuit ($\ddot{\alpha}$, $\dot{\alpha}$)

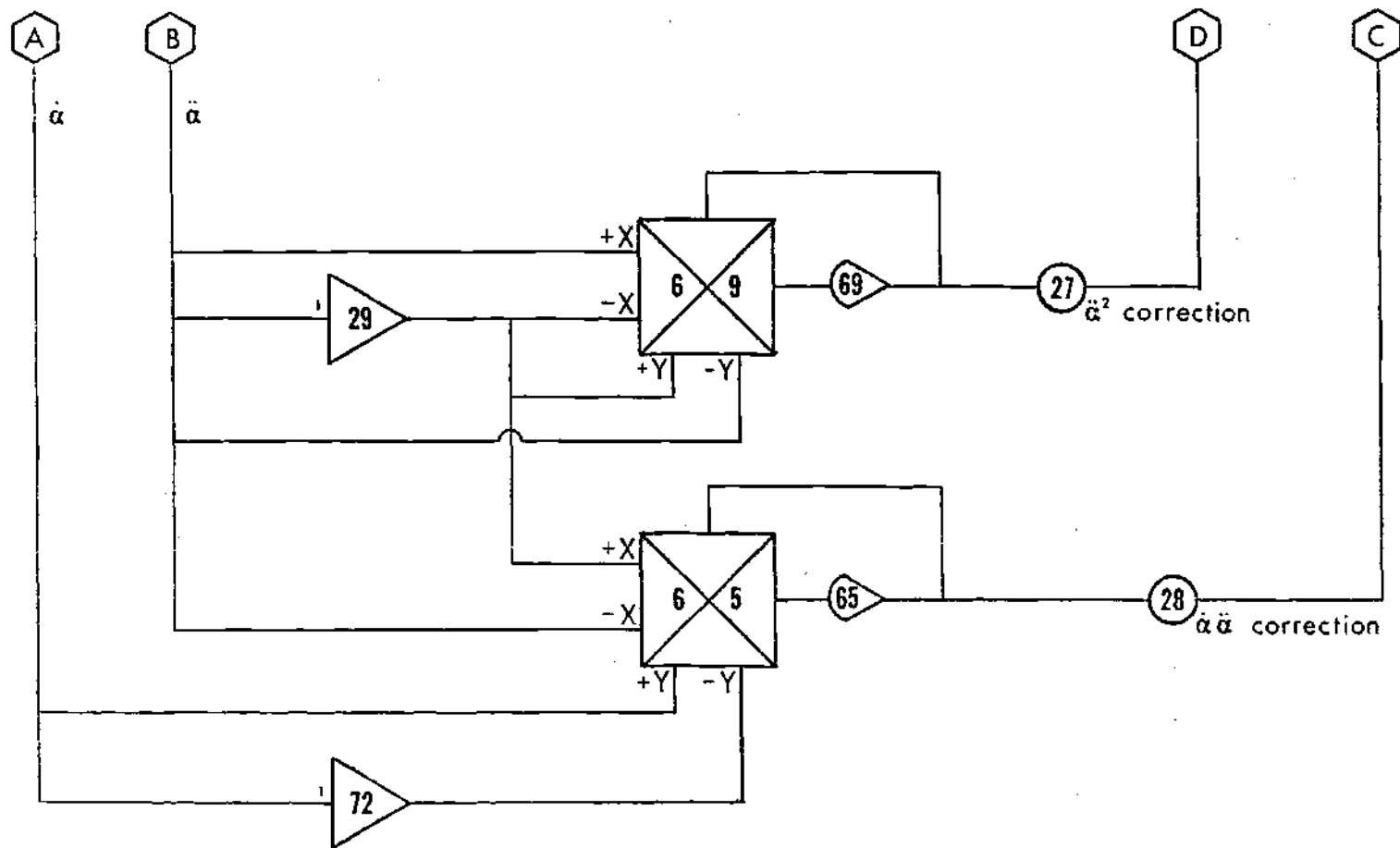


Figure 12. Moment Correction Circuit ($\ddot{\alpha}^2$, $\dot{\alpha}\ddot{\alpha}$)

maxima and minima are continuously added and fed back into I11, stabilizing the integration. Having obtained a stable angular velocity, the proper proportion was obtained using P26 and the gains of A07 and A09.

On an oscilloscope display of the corrected moment versus angular acceleration, it was seen that although the $\dot{\alpha}$ and $\ddot{\alpha}$ corrections had removed most of the unwanted moment contributions, some still remained. The most obvious higher-order correction needed was an $\ddot{\alpha}^2$ correction. This was included as shown in Figure 12. The angular acceleration out of A20 was squared in multiplier M69, and the correction factor applied by P27 and the gain on A09.

Again viewing the moment, this time with three correction terms, versus angular acceleration on the oscilloscope, the need for an $\dot{\alpha} \ddot{\alpha}$ factor became apparent. The multiplication of the angular velocity out of A07 and the angular acceleration out of A20 was done by M65. Using P28 and the gain into A09, the correction constant was adjusted to an optimum value.

Merely by looking at the gains on the correction factor inputs to A09, it can be seen that the $\dot{\alpha}$ and $\ddot{\alpha}$ contributions amounted to the greater part of the moment acting on the model, while it oscillated in still air. This conclusion was borne out by observations of the corrected and uncorrected moment signals on the oscilloscope. Even though $\ddot{\alpha}^2$ and $\dot{\alpha} \ddot{\alpha}$ contributions were approximately an order of magnitude smaller than the $\dot{\alpha}$ and $\ddot{\alpha}$ contributions, they were still very important since they were of the same order of magnitude as the aerodynamic moment. The point is that without this or some other

equivalent method of cancelling out the still air moment, it would have been virtually impossible to separate the aerodynamic moment from the total moment.

Data Recording

Having established a method of acquiring and reducing the data, a means of recording and storing it had to be developed. Using the horizontal display of the Tektronix, Model No. 533A, dual-trace oscilloscope for the angular acceleration, and the vertical display for the aerodynamic moment, curves of moment versus acceleration were produced. These were recorded on Polaroid Type 47, high-speed film taken by a Tektronix Oscilloscope Camera C-12. The camera was equipped with an Ilex Speedcomputer and Electronic Shutter.

The idea behind taking data in the harmonically varying freestream was to get traces of one complete pitching cycle of the model in specific areas of the velocity curve. These could then be compared to equivalent constant freestream data. The areas of the curve that seemed most interesting were: increasing velocity through the mean velocity (0°), at the maximum velocity (90°), decreasing through the mean (180°), and at the minimum (270°).

As an example of how this would work, consider the model oscillating at 6 times the frequency of the velocity variations (Figure 13). Since one model pitching cycle would cover 60° of one velocity cycle, a photograph of the 90° area would start at 60° and end at 120° . Similarly a photograph of the 180° area would start at 150° and end at 210° . In Figure 13, the solid lines show the areas of the curve that would be photographed at each station.

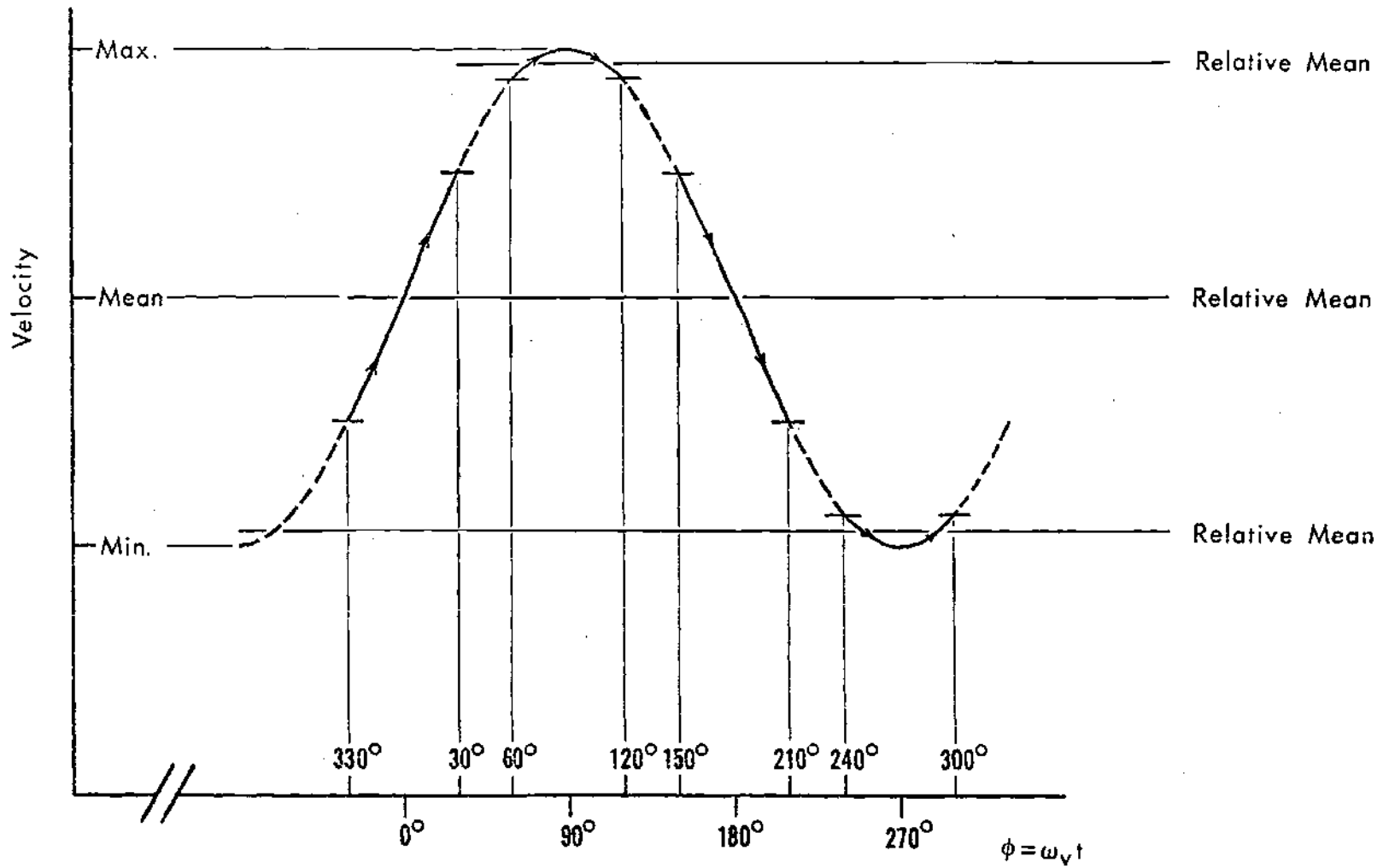


Figure 13. Gust Generator Velocity Curve ($R=6$)

It was for the purpose of taking these photographs that the timing disk (Figure 14) was installed. The steel stud fixed to the edge of the disk passed close to the magnetic pickup once every vane rotation, or once every other velocity cycle. This caused the pickup to send out a voltage pulse. The location on the velocity curve where this pulse was generated depended on the position of the stud with respect to the vanes, and could be adjusted by rotating the disk.

The pulses from the magnetic pickup were sent to the analog computer, where a circuit had been designed to operate the camera shutter and the oscilloscope single sweep trigger (Figure 15). With this circuitry, the shutter could be opened anytime before the sweep was triggered, then closed after a single sweep.

Obtaining one, and only one, pitch cycle of the model proved to be no problem, as the oscilloscope time scale could be set so that the single sweep would only last long enough for the model to complete one cycle. Also, the closing of the camera shutter presented no difficulties, since the exposure time could be controlled by the speed selector knob on the Speedcomputer. The required exposure time was easily computed by summing the period of one model cycle and the time delay between the triggering of the shutter and the sweep.

The need for using the analog computer and its digital expansion system arose for three reasons. First, the magnetic pickup did not put out enough voltage to trigger either the shutter or the sweep. Also, a time delay in triggering the sweep was needed so that the shutter would be fully opened for the entire sweep. Finally, it was necessary to shut off the triggering pulses while preventing another triggering pulse

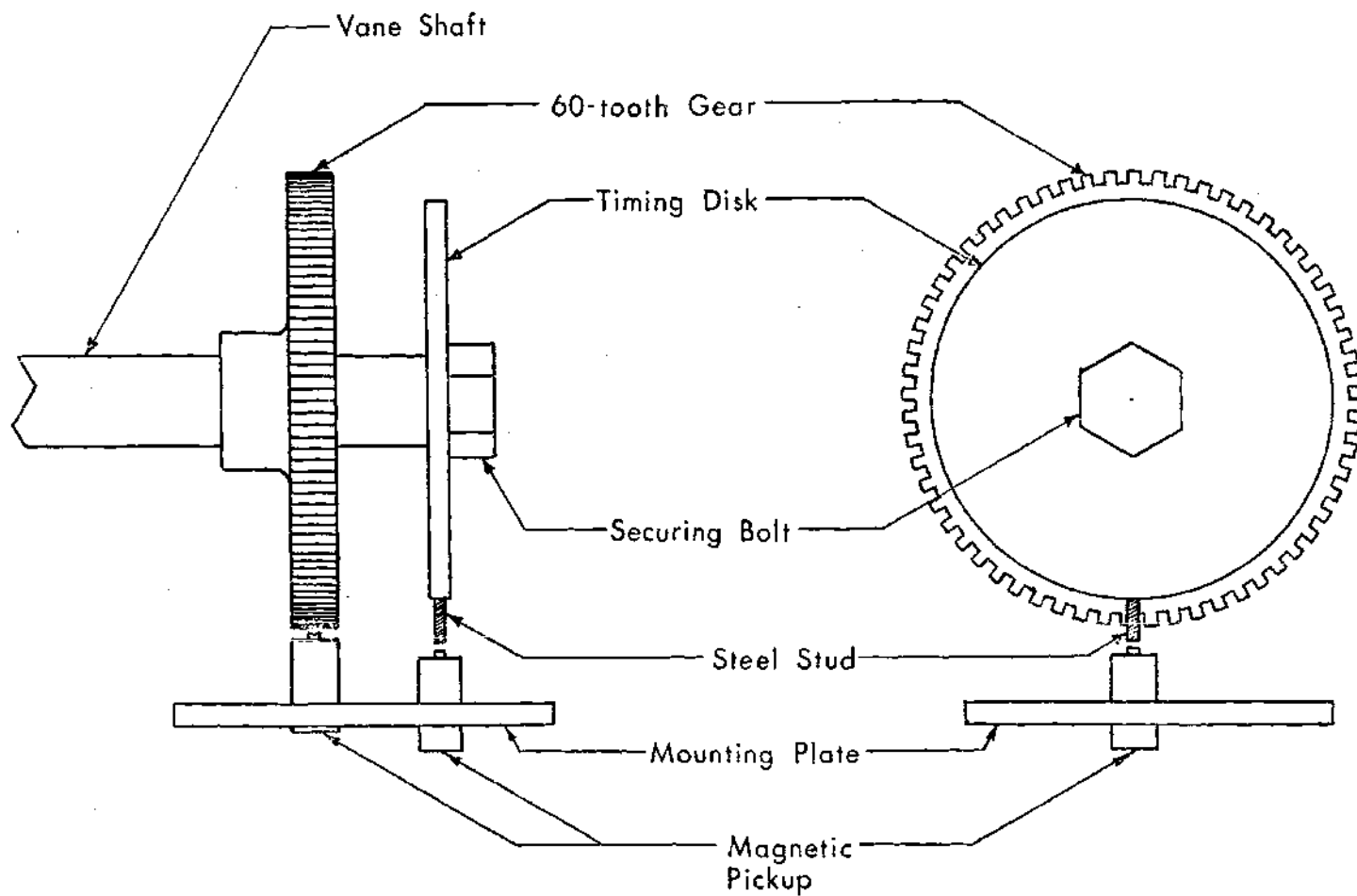


Figure 14. Timing Disk Assembly

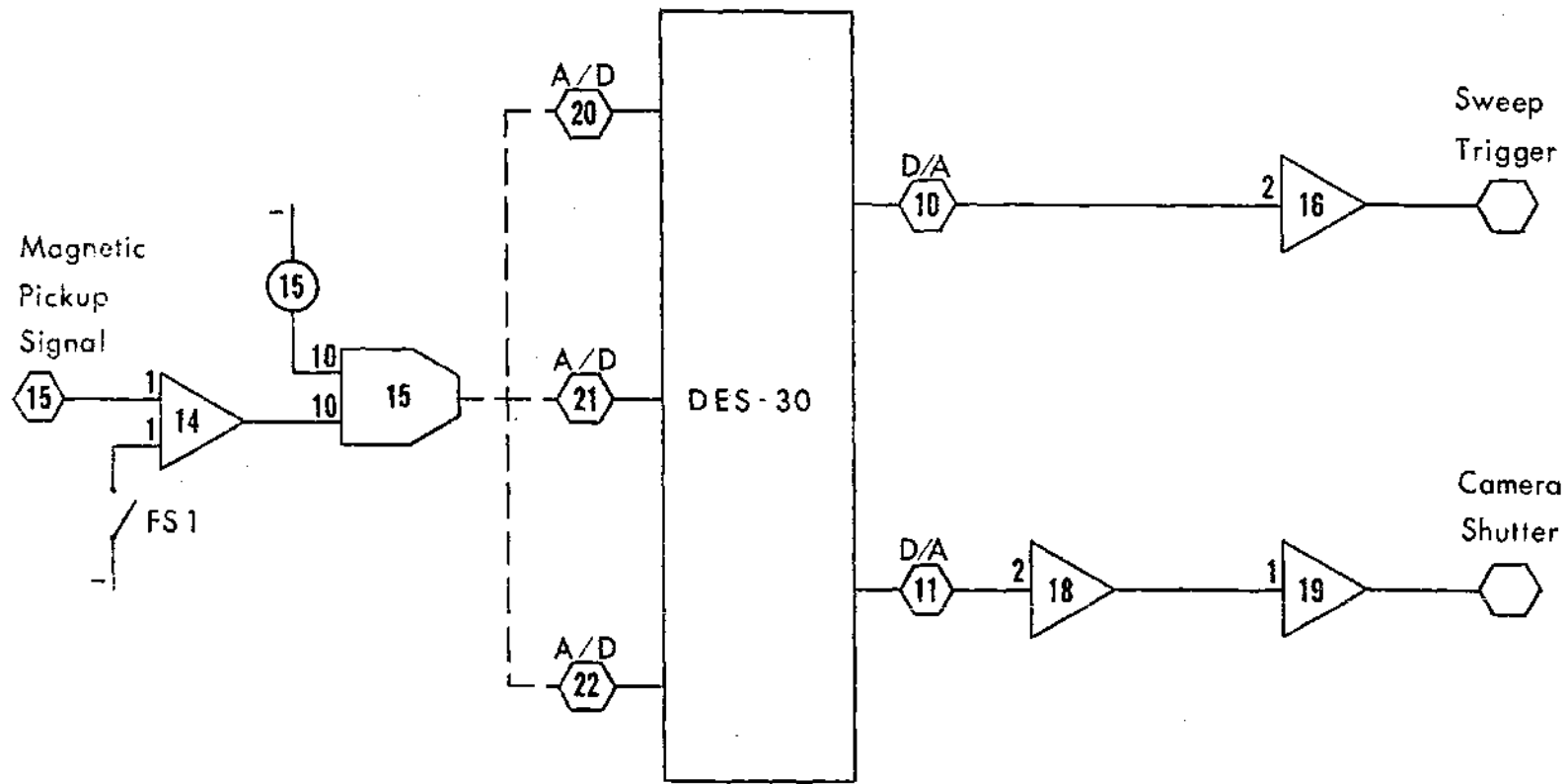


Figure 15. Analog Shutter Synchronization Circuit

from being generated.

The small output of the magnetic pickup required that either the pulses be amplified or used to generate a larger voltage. In view of the other requirements, the second alternative was chosen. The line from the magnetic pickup was connected to the analog computer and fed in through trunk line 15 (Figure 15). This signal was then put into C15 after undergoing a sign change in A14. For proper operation of C15, a biasing voltage had to be applied to the other input. It was controlled by P15. When correctly set up, C15 put out a +1 digital signal (5 volts) when a pulse was sensed, and a digital 0 (0 volts) when there was no pulse. The digital output of C15 was sent to the DES-30, where the time delay and triggering pulse control circuitry had been built, through analog-to-digital trunks 20, 21, and 22.

The time delay circuitry for the sweep trigger starts at A/D 20 (Figure 16), and includes flip-flops 20D and 21B, monostable timer MTO6, and differentiator O6. Figure 17 shows the timing of the circuit. A digital +1 from C15 sets 20D, which causes MTO6 to put out a +1 for t_1 seconds. The complementary output of MTO6, $\overline{\text{MTO6}}$, then starts with a +1 output and goes to 0 after 20D sets. Differentiator O6 goes to +1 for one clock whenever it feels the leading edge of a pulse from $\overline{\text{MTO6}}$. Thus, the first +1 output of the differentiator occurs t_1 seconds after MTO6 goes to +1. Flip-flop 21B is set after DO6 goes to +1, and it is this signal which goes through digital-to-analog trunk 10. It is this signal which eventually triggers the oscilloscope sweep.

Triggering the camera shutter was much less complex, as no time delay was required. The output of C15 goes through A/D trunk 21, sets

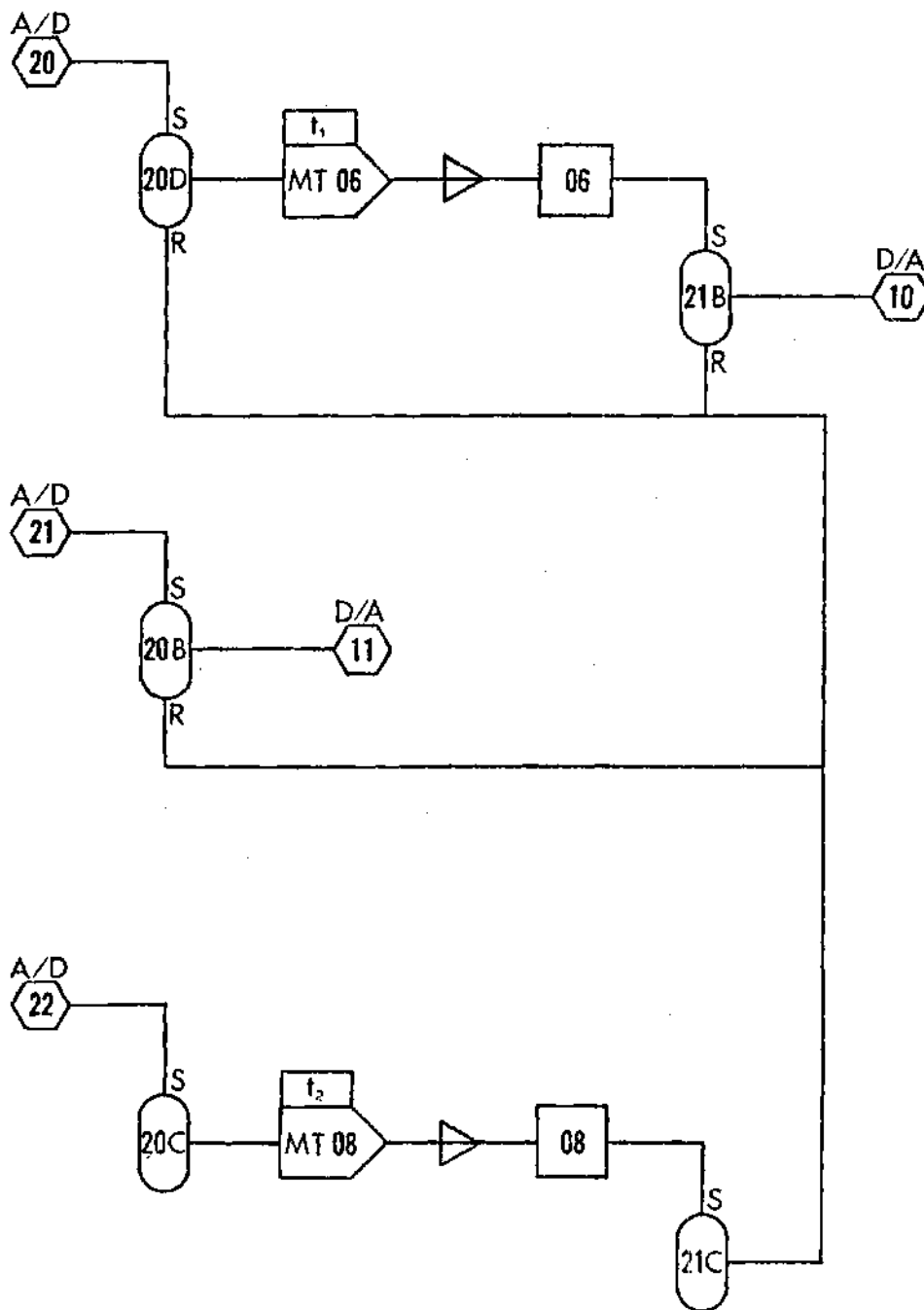


Figure 16. Digital Shutter Synchronization Circuit

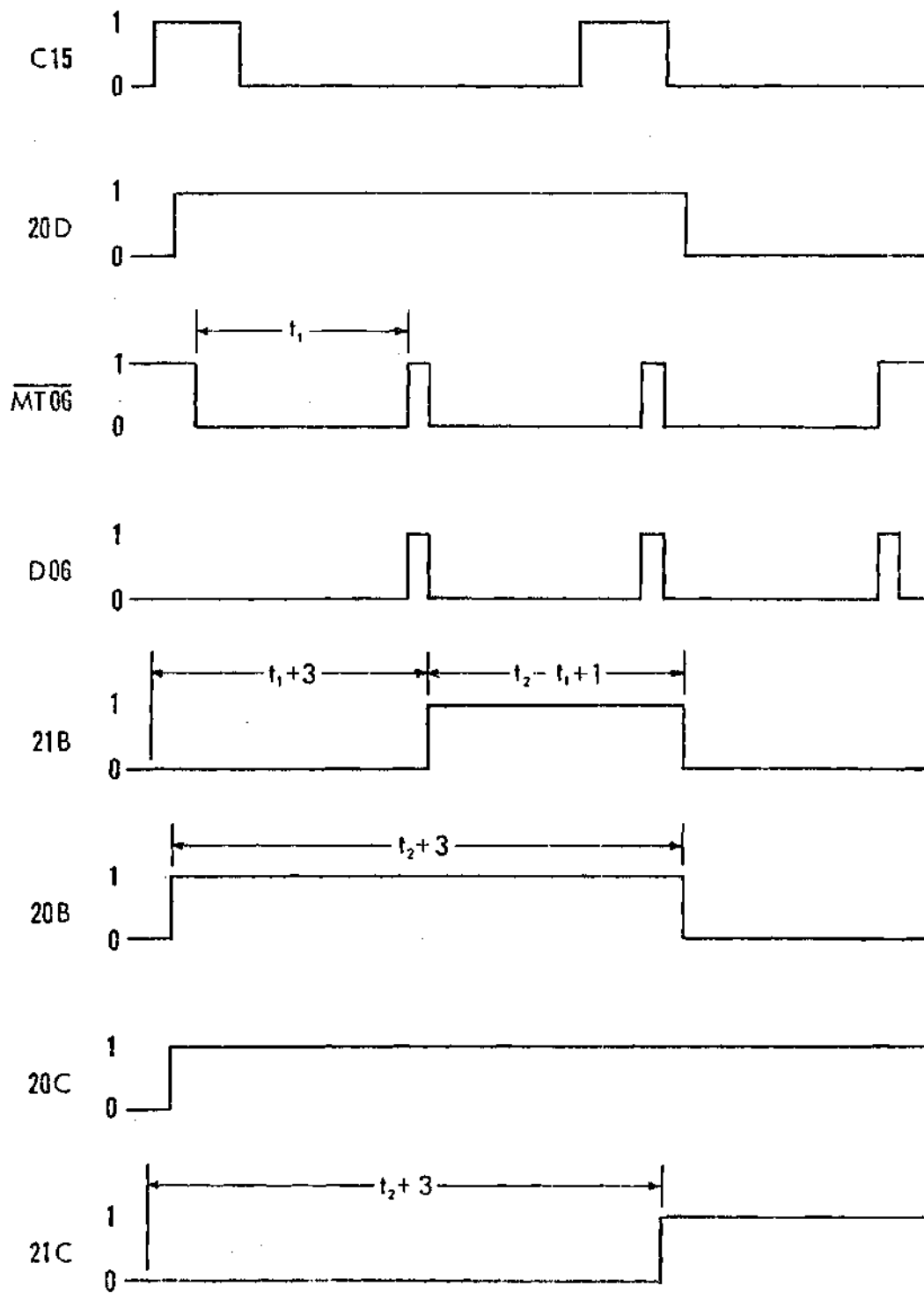


Figure 17. Digital Sequencing

20B, and returns to the analog computer through D/A trunk 11. Note that there is a delay of one clock between the time C15 goes to + 1 and when 20B goes to + 1. This is due to the fact that all of these flip-flops react to their input on the next clock. That is the reason for the digital sequencing diagram having such notations as $t_1 + 3$ and $t_2 - t_1 + 1$. The numbers indicate the number of clocks in the time span. The length of a clock period depends on which of the three internal timing clocks is selected. For the purposes of this investigation the 1 MHz clock was used, giving a clock period of one microsecond. The other clocks have periods of one millisecond and one second.

The section of the circuit that shuts off the triggering pulses starts at A/D trunk 22. All of the components behave in the same way as those in the time delay circuitry. The only difference in this section is that the monostable timer constant is $t_2 (t_2 > t_1)$, and that the output of 21C is fed into the reset inputs of 20D, 21B, and 20B. As shown in Figure 17, these three flip-flops all go back to 0, one clock after 21C sets. They remain at 0 until 21C is cleared and another pulse is felt.

Returning to Figure 15, the triggering pulse from D/A trunk 10 is multiplied by a factor of two in A16, so that the triggering signal to the oscilloscope sweep trigger is a full -10 volts. Similarly, the pulse from D/A trunk 12 is multiplied by two in A18, but due to the requirements of the Speedcomputer, a sign change (A19) is needed to get a + 10 volt signal.

The convenience of this timing sequence and automatic triggering made it desirable for use in collecting constant freestream data. However,

the vanes were stationary in this case and no pulses could be obtained from the magnetic pickup. To take care of this, switch FS1 was added to provide a manual trigger. When closed, a -10 volt signal is fed into A14. Upon the application of this pulse, the rest of the circuitry operates as described above.

Proper operation of the circuit requires that the analog computer be in either the IC or OP mode. To make it ready for operation, the DES-30 is put in the RUN mode. After the manual or magnetic pickup pulse is applied and the triggering is complete, the DES-30 is put into CLEAR. Switching the DES-30 back to RUN rearms it for another pulse.

Flow Parameter Control

For each set of data taken, six parameters determined the flow condition to be investigated. These quantities were the three model parameters (mean angle of attack, amplitude of oscillation, and model frequency) and the three velocity parameters (mean velocity, gust amplitude and gust frequency). Of the six, only three needed to be monitored during the course of the tests.

The three which did not require any checking were the mean angle of attack, the amplitude of oscillation, and the gust amplitude. The first two of these three quantities were model parameters that were fixed by the geometry of the drive system (see Chapter III). Since the gust amplitude was a function of vane size, which was fixed, and of mean velocity and gust frequency, which were to be monitored, there was no reason to check on it. The value of the gust amplitude was determined solely by these three quantities, and could be calculated from the operational curves (Table 1).

In the following paragraphs, the means used to monitor the remaining flow parameters are described. The number of variables in this set-up made it imperative that those parameters which needed checking remained at their assigned values.

Gust Frequency Control

As described in Chapter II, the gust generator was fitted with a 60-tooth gear (Figure 2). Close to this was placed a magnetic pickup, which sent out a pulse as each tooth passed. To eliminate noise from the pulse train and make the pulses easier to count, the signal from the pickup was filtered through one channel of a Krohn-Hite, Model 3202R, low-pass filter. Then it was fed into a Hewlett-Packard, Model 5302A, 50 MHz Universal Counter.

The fact that the gear had 60 teeth made it possible to have the counter readout give the vane frequency in revolutions per minute. Since the vane frequency was half of the gust frequency, dividing the counter reading by 30 gave the gust frequency in Hertz.

Monitoring the gust frequency was easy because of the stability of the counter readings. Once the proper frequency was set, only periodic checks had to be made.

Mean Velocity Control

In the constant freestream, the measurement of the mean velocity presented no problem, since the hot-wire voltage could be read directly from a digital voltmeter. Knowing the hot-wire voltage for any desired velocity, the wind tunnel controls were easily set to obtain that velocity.

Recalling that, with the gust generator in operation, the velocity in the tunnel had simple harmonic velocity perturbations impressed on it,

it can be seen that the mean velocity could not have been measured simply by using a digital voltmeter. To solve this problem, the analog computer was again used (Figure 18).

The hot-wire signal was fed into the computer through trunk line 1. There, it went into the averaging circuit. Essentially, this consisted of an integrator with a feedback resistor. The values of P00 and P01 were set to be identical, and determined how fast the circuit would reach the average. Due to the presence of the potentiometers in the circuit, the average put out by I00 was somewhat off of the true average. Thus, P02 was used to compensate for this offset by adding a constant voltage to the output of I00.

This average or, in this case, mean voltage was displayed on the analog computer's digital voltmeter. Like the gust frequency readings, these readings were stable, and required only periodic checks after the initial setting was made.

Model Frequency Control

As in the case of the gust frequency, the model frequency was measured using a 60-tooth gear with a magnetic pickup sending out a pulse train. This signal was filtered through the other channel of the same filter used by the gust frequency pickup before going into a Hewlett-Packard, Model 5301A, 10 MHz Counter. The readout from the counter gave the model frequency in RPM. A conversion to Hertz was readily made by dividing the model RPM by 60.

Unlike the gust frequency readout, the model frequency readout was most difficult to monitor. Not only did it require constant checking, but a double-check using the output of the accelerometer had to be made

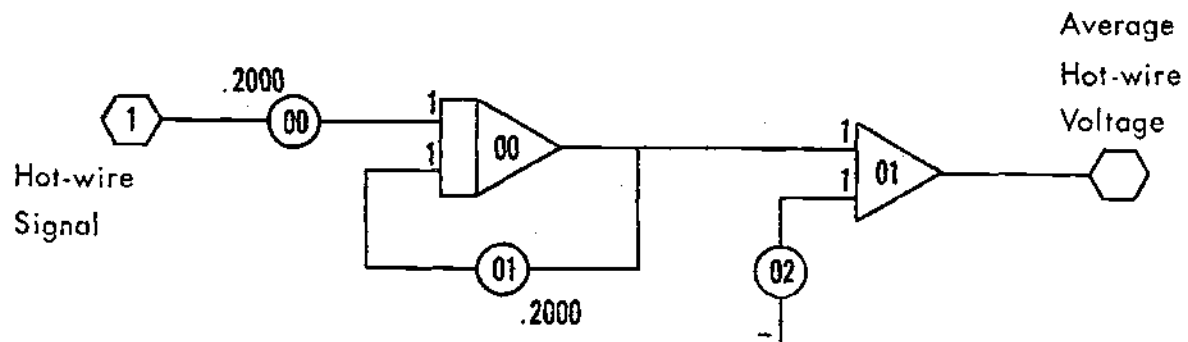


Figure 18. Hot-wire Voltage Averaging Circuit

for each photograph taken.

Experimental Procedures

Before the actual taking of data was attempted, a procedure was set up, such that the data could be taken quickly, easily, and with minimal experimental error. During the preliminary testing, this procedure was refined and several checks on the data were included.

Warm-up and Preliminary Checks

One hour before any testing was to take place, all of the electronic equipment, except for the hot-wire anemometer, was turned on and allowed to warm up. This lengthy warm-up period was actually only necessary for the tracking filter, but it was felt that giving everything a chance to warm up could only be beneficial. The hot-wire anemometer was turned on, as per its instructions just prior to the preliminary checks. This kept the probe, which was most delicate, protected from harm for as long as possible.

After the warm-up period was over, the inputs to both channels of the low-pass filter (Figure 10) were disconnected and replaced by two in-phase signals from an audio oscillator. The frequencies of the two signals were identical to each other and to the model frequency for the next series of tests. Observing the output of the analog computer on the oscilloscope served as a check for distortion or equipment failure. Using the phase adjustment on the tracking filter, the two output signals were put in phase. This assured that there would be no phase difference between moment and acceleration. Finally, the connections to the moment bridge and the accelerometer were replaced.

Still Air Moment

Once the equipment was warmed up and checked out, it was necessary to cancel out the moment acting on the model while it oscillated in still air. The model was turned on and its frequency set to the appropriate value. On the oscilloscope was displayed a figure which represented moment plotted versus angle of attack for the model. Ideally, without inertia and damping, this figure would have indicated zero aerodynamic moment. Since this was not the case, the moment correction circuit (Figures 11 and 12) was used to force the output to zero. By setting P10, P25, P26, P27, and P28, and observing the oscilloscope display, the moment could be nearly set to zero.

Constant Freestream Data

The first data taken for each experimental condition was for the model oscillating in a freestream with a constant velocity. Three freestream velocities were selected for each condition. Each corresponded to the relative mean velocities of the portions of the velocity curve that would be photographed during the varying freestream tests (Figure 13).

After the proper airspeed, as measured by the hot-wire anemometer, was attained in the test-section, the readings on the digital voltmeter connected directly to the anemometer and on the analog computer's digital voltmeter (giving the output of A01) were made identical by adjusting P02 (Figure 18). The purpose of this was to make sure that the averaging circuit would seek the true mean in the varying freestream tests.

Using the manual trigger to operate the shutter synchronization circuit, photographs were taken of the aerodynamic moment versus negative acceleration curves for one model pitching cycle. A second exposure was

taken on each photograph, giving the vertical location of the horizontal axis. When the picture was developed, the total horizontal length of the trace was checked against a standard length. Since a change in model frequency would be reflected in the acceleration, or the horizontal length of the trace, this served as a check on the model frequency.

Varying Freestream Data

The most important of the data taken was the aerodynamic moment acting on the model while it oscillated in the harmonically pulsating freestream. Four areas on the velocity curve were recorded for each experimental condition. These regions were centered at 0° , 90° , 180° , and 270° , and covered that portion which one complete model pitching cycle would traverse.

Before starting the wind tunnel, the vanes were turned on, so that they would not be subjected to severe steady-state loads. With the vane frequency set, the wind tunnel was turned on and the mean test-section airspeed set to the approximate value. The output of the averaging circuit (AO1), as displayed on the analog computer's digital voltmeter, gave this mean velocity.

The actual recording of data involved monitoring the model frequency on its counter until it had stabilized at the proper value. Then, the shutter synchronization circuit was activated so that it would trigger on the next vane revolution. Again, a second exposure was made to determine the location of the horizontal axis, and the length of the trace was checked against the standard.

To prepare to record the next velocity region, the wind tunnel was shut down, the vanes were stopped, and the timing disk was rotated into

its next position. Then, the recording procedure above was repeated. For each region on the velocity curve, the wind tunnel and vanes had to be shut down. As inconvenient as this was, it did provide an opportunity to check the still air moment to see that it had not drifted away from zero.

Aerodynamic Moment Coefficient

In order to conform to the conventional way of presenting the aerodynamic moment, it was necessary to nondimensionalize it to get an aerodynamic moment coefficient. This was done in the usual manner, letting

$$C_m = M_a / \frac{1}{2} \rho V_o^2 c^2 s \quad (1)$$

where c is the chord length and s is the span. For all the data, the reference velocity was taken to be the mean velocity of the pulsating freestream (42.50 ft/sec).

This meant that the constant freestream moment data were not necessarily nondimensionalized using the constant freestream velocity, and the varying freestream moment data were not necessarily nondimensionalized using the relative mean velocity. The reasons for using this approach were to maintain uniformity with each set of data, and to eliminate the need for transforming the majority of the data to fit a different scale.

Angle of Attack

With the aerodynamic moment coefficient being displayed on the vertical axis of the oscilloscope, it would have been convenient to

display the angle of attack on the horizontal axis. Then, the moment versus angle of attack would be available and not require any further manipulation.

It was found that with the existing apparatus, there was no suitable method of measuring the angle of attack, such that it could be displayed on the oscilloscope. Therefore, it was decided to synthesize an angle of attack scale by using the angular acceleration signal.

Comparing the acceleration signal out of the analog computer to a signal from an audio oscillator, it was found that the acceleration was almost perfectly simple harmonic. It was also known that the change in angle of attack was simple harmonic. For any mean angle α_0 , amplitude α_1 , and frequency ω_α ,

$$\alpha = \alpha_0 + \alpha_1 e^{i\omega_\alpha t} \quad (2)$$

Differentiating twice to get the angular acceleration,

$$\ddot{\alpha} = -\omega_\alpha^2 \alpha_1 e^{i\omega_\alpha t} \quad (3)$$

Since the values of α_0 , α_1 , and ω_α were all known for any experimental condition, the negative angular acceleration could be used to represent the change in angle of attack. Had the model pitching motion not been simple harmonic, this approach would not have been permissible.

Pitching Stability

To determine the stability of the model's pitching motion, the sign of the damping had to be found. Positive damping means that the

motion is stable, while negative damping indicates an instability. The area enclosed by the C_m trace gives the cycle damping (or work per cycle), and is defined, as in Reference 4, by

$$\text{damping} = \oint C_m d\alpha \quad (4)$$

When a C_m curve traces a counterclockwise circuit, the damping is positive and the motion stable. Similarly, the tracing of a clockwise circuit gives negative damping and unstable motion. Where there are loops in the C_m vs. α curves, regions of stability or instability are indicated. For instance, a curve shaped like the sign for infinity, making a clockwise circuit at the higher angles, shows unstable motion in that region. At the lower angles, however, the motion is stable, as indicated by the counterclockwise circuit.

CHAPTER V

RESULTS AND DISCUSSION

The data that were taken and reduced by the method described in the preceding sections were compiled to facilitate its analysis. Seven sets of flow conditions were selected for study (Table 2). The conditions chosen were those which might best show the dependence of moment coefficient on mean angle of attack (α_o), model frequency (ω_a), gust frequency (ω_v), and frequency ratio (R).

Static Moment Data

Figure 19 shows the static moment curve for this airfoil model. The data was taken at an airspeed of 42.50 ft/sec ($Re = 2.02 \times 10^5$), which was the mean velocity for all of the varying freestream conditions. Also shown in the figure is the static curve as presented by Carter et al., [22].

It is apparent that although both models were of NACA 0012 cross-section, the moment curves are markedly different. The results of the present tests, which show a gradual increase in nose-down moment after a sharp, but short, dropoff, seem to indicate that this model underwent "thin airfoil stall" [4]. On the other hand, Carta's moment curve shows a large increase in nose-down moment which continues out to an angle of attack of 24° . This behavior is typical of the "leading edge" type of stall that would, in most cases, be associated with a 12% thick airfoil section [4].

Table 2. Oscillating Airfoil Experimental Flow Conditions

Condition	α_0 (deg)	α_1 (deg)	ω_α (hz)	V_0 (fps)	V_1 (fps)	ω_v (Hz)	R	$\Delta\phi$ (deg)	Figure No.
1	6	4	6	42.50	7.53	1	6	60	21,28
2	10	4	6	42.50	7.53	1	6	60	22,29
3	14	4	6	42.50	7.53	1	6	60	23,30
4	18	4	6	42.50	7.53	1	6	60	24,31
5	10	4	6	42.50	3.04	2	3	120	25,32
6	10	4	12	42.50	3.04	2	6	60	26,33
7	10	4	12	42.50	7.53	1	12	30	27,34

$$\alpha = \alpha_0 + \alpha_1 e^{i\omega_\alpha t}$$

$$V = V_0 + V_1 e^{i\omega_v t}$$

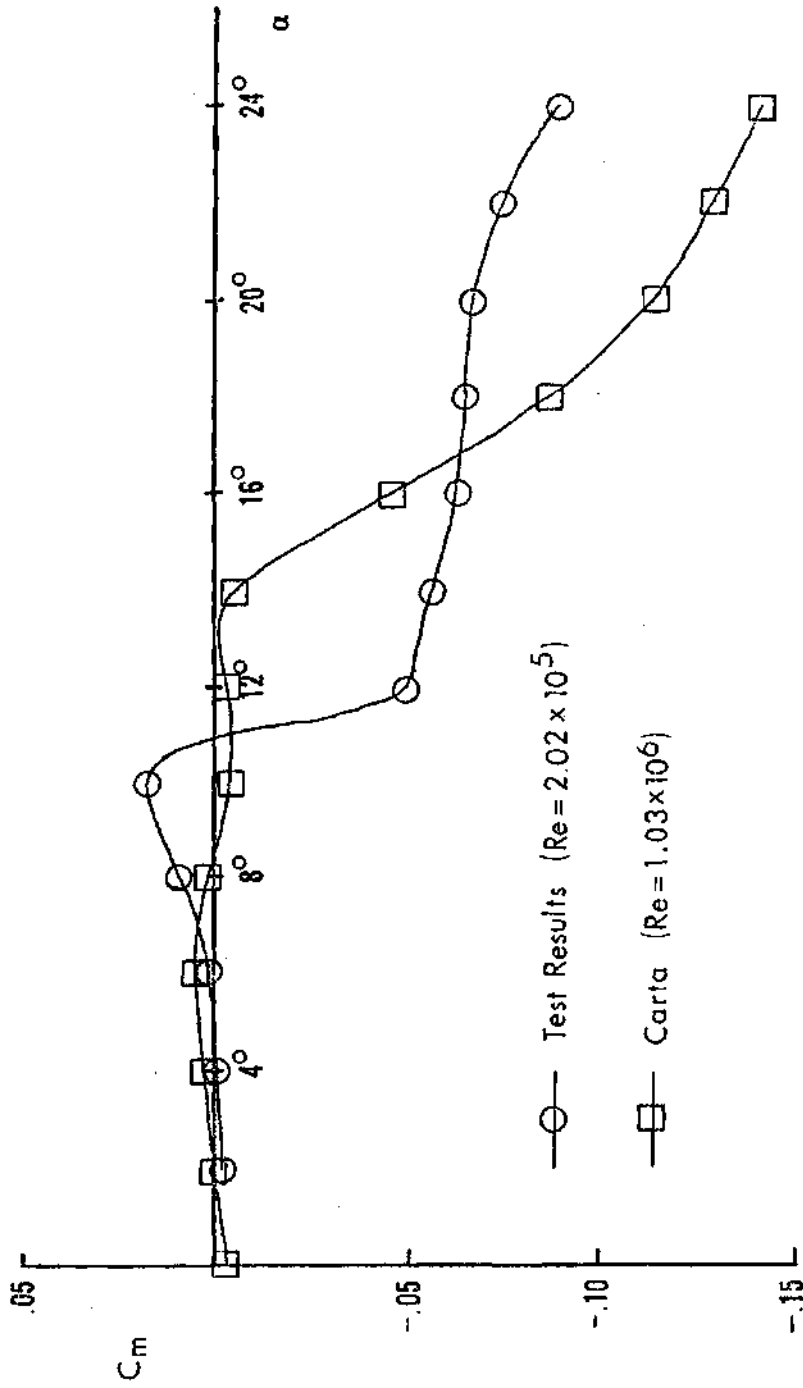


Figure 19. Static Moment Curves

This evaluation of the two static moment curves is backed up by the findings of Gault [26], and Ericsson and Reding [27]. They pointed out that the stall type is strongly dependent on Reynolds number and leading edge curvature. For a Reynolds number of 1.03×10^6 and an NACA 0012 section, as Carta had, it would be expected that the airfoil would experience leading edge stall (Figure 20). Depending on such factors as surface roughness and turbulence, there is also the possibility that the stall could be of the mixed leading and trailing edge type. Although Figure 20 does not include Reynolds numbers as low as 2.02×10^5 , the findings in Reference 26 indicate that at such a low Reynolds number, thin airfoil stall would be expected.

These differences in static behavior suggest that there might also be differences in dynamic behavior. In their discussion of dynamic stall testing, Ericsson and Reding [27] included this among the problems that could be encountered. Thus, it might be expected that comparisons of the test data and Carta's results would not show close agreement in the stall region.

Constant and Varying Freestream Moments

To gauge the effect that the harmonically varying freestream velocity has on the pitching moment coefficient, the varying freestream moment data was compared to the constant freestream moment data. The format of this comparison is such that for each mean velocity position (ϕ_m) and its corresponding relative mean velocity (V_r), a constant velocity (V_∞) equal to V_r is on the same horizontal line. In this way, the effects of the varying freestream can be readily observed.

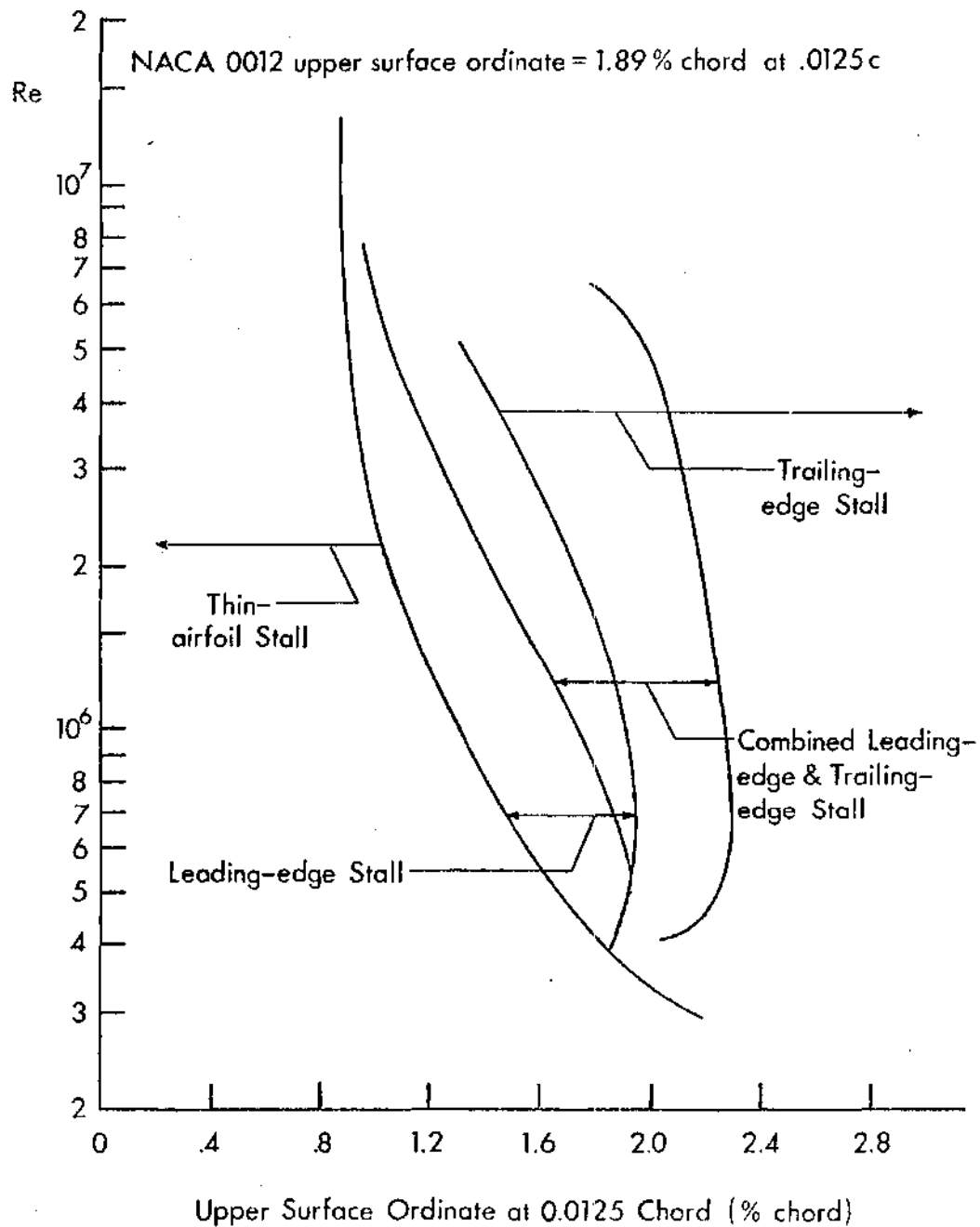


Figure 20. Static Stall Type as a Function of Reynolds Number and Leading Edge Curvature (from [26])

It can be seen that the constant freestream curves change with velocity in all of Figures 21-27. These changes can be attributed to both variations in dynamic pressure and Reynolds number. The dynamic pressure effects predominate in the constant freestream curves of Figures 21, 23, 24, 26, and 27, where the areas enclosed by the curves increase with increasing freestream velocity. Since a single reference velocity was chosen for all of the cases, this effect of dynamic pressure appears in the plots.

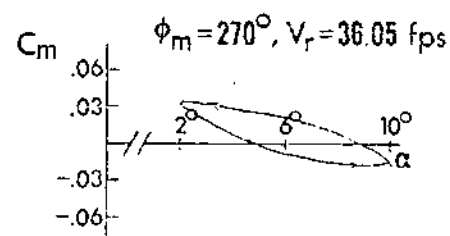
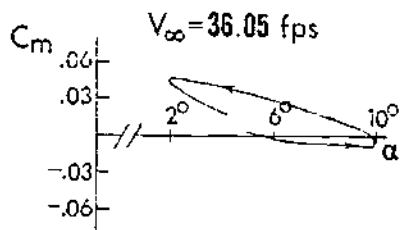
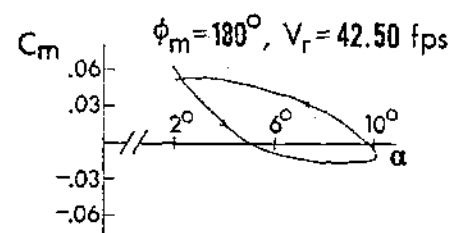
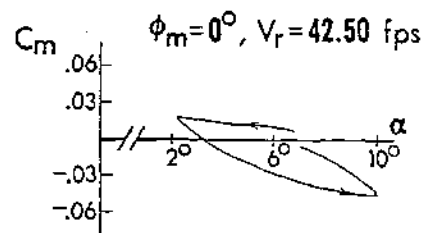
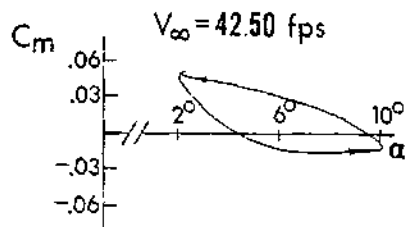
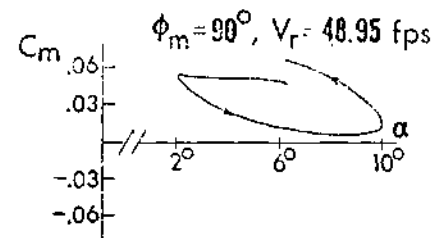
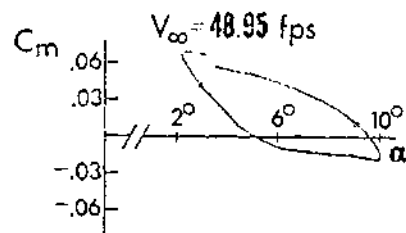
The constant freestream curves in Figures 22 and 25 show primarily the effects of the change in Reynolds number. The Reynolds number changes of approximately 15 and 3 percent, respectively, appear as pronounced alterations in the curve shape. The influence of dynamic pressure is also undoubtedly present, but is overshadowed by Reynolds number effects. The reasons behind the greater dependence on Reynolds number in these cases are not precisely unknown, but are probably related to the particular combination mean angle of attack and frequency of the model.

Angle of Attack Effects

Figures 21-24 show the effects of changes in mean angle of attack. Holding all of the other parameters constant, the mean angle was varied so that the model would oscillate about 6° , 10° , 14° , and 18° . Since the amplitude for all cases was 4° , the model was operating in four different regimes with respect to the static stall angle (Figure 19).

At a mean angle of 6° , the results were pretty much as expected. The moment curves were somewhat elliptical, but with rather pointed ends, and the oscillations were stable.

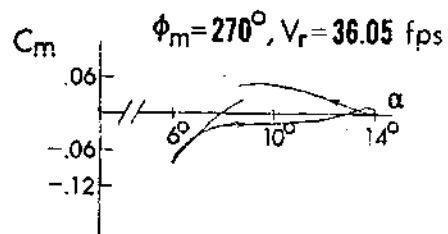
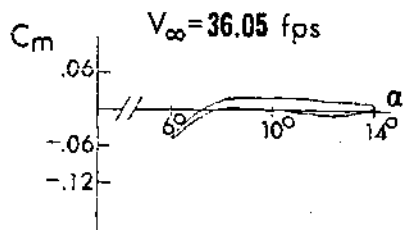
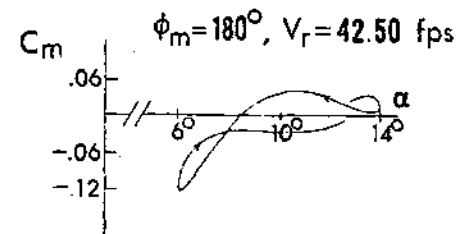
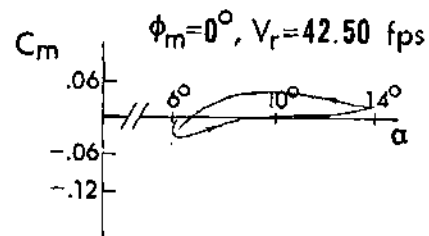
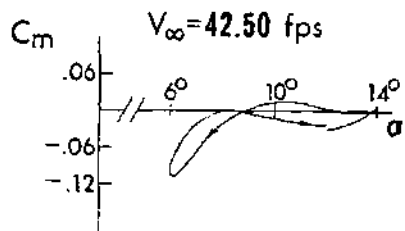
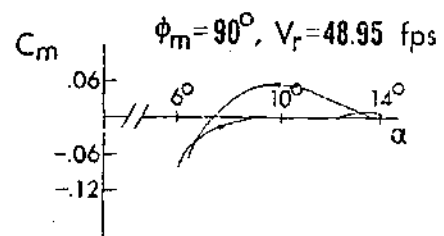
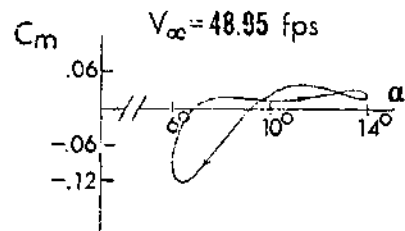
The mean angle of attack of 10° caused a drastic change in the



CONSTANT FREESTREAM

VARYING FREESTREAM

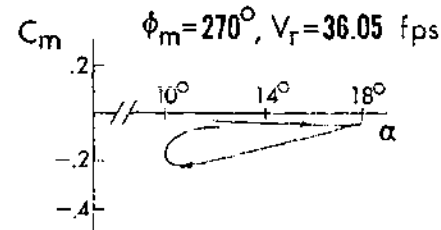
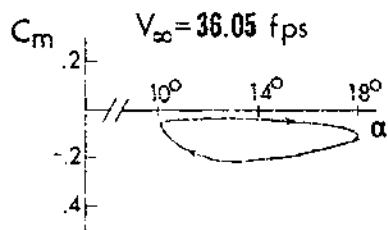
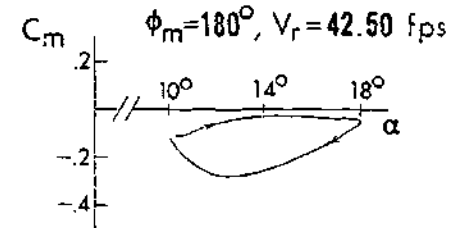
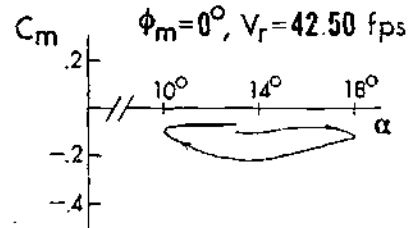
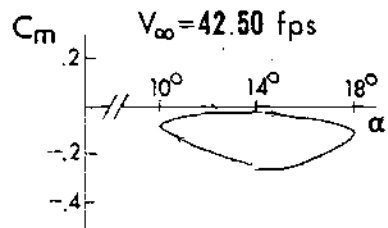
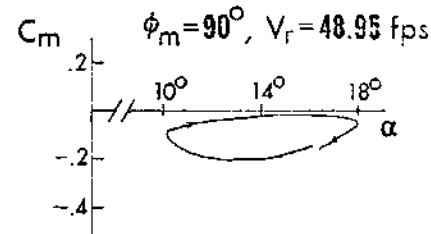
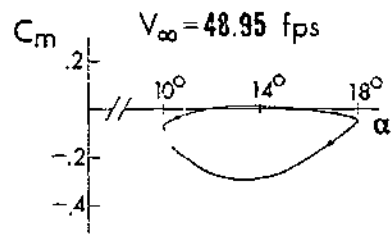
Figure 21. Sequential C_m vs. α for Oscillations About 6° at 6 Hz in Constant and 1 Hz Varying Freestreams



CONSTANT FREESTREAM

VARYING FREESTREAM

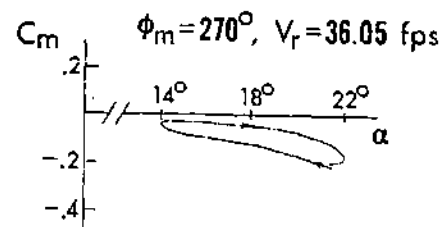
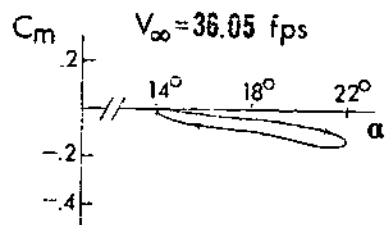
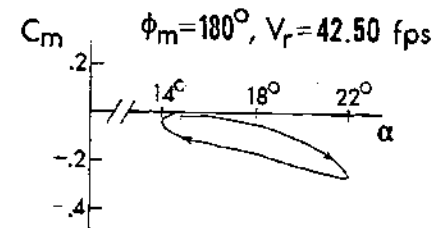
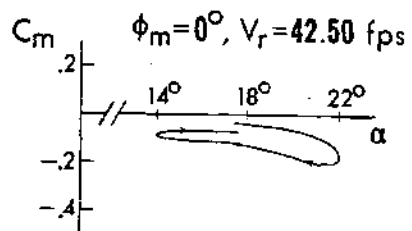
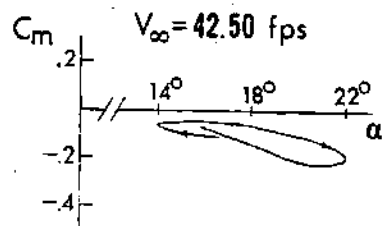
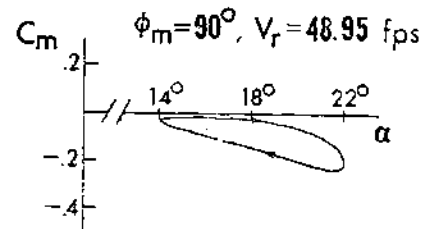
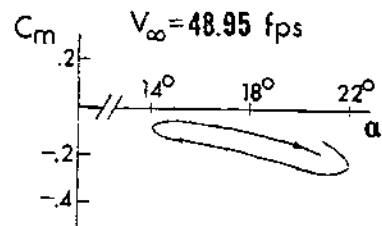
Figure 22. Sequential C_m vs. α for Oscillations About 10° at 6 Hz in Constant and 1 Hz Varying Freestreams



CONSTANT FREESTREAM

VARYING FREESTREAM

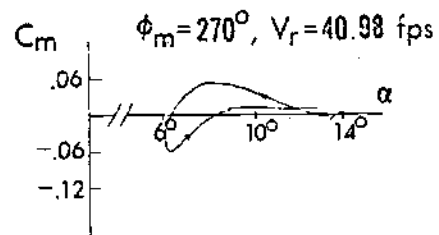
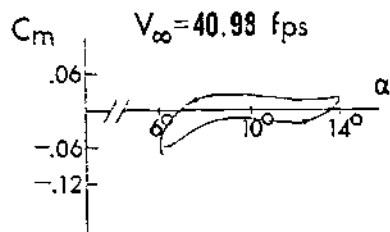
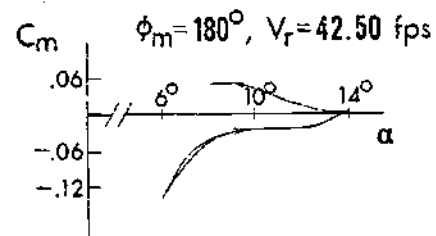
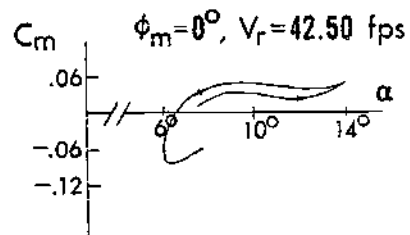
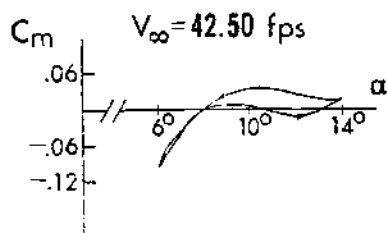
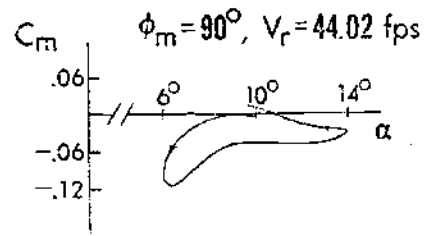
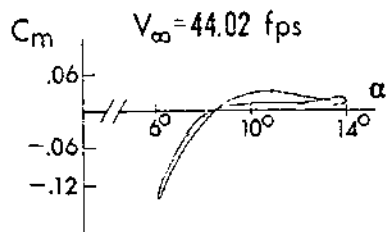
Figure 23. Sequential C_m vs. α for Oscillations About 14° at 6 Hz in Constant and 1 Hz Varying Freestreams



CONSTANT FREESTREAM

VARYING FREESTREAM

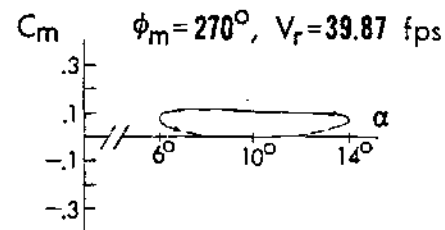
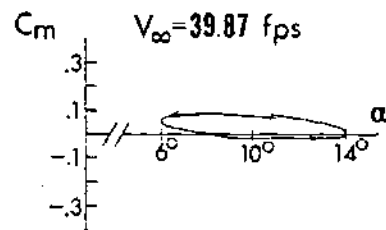
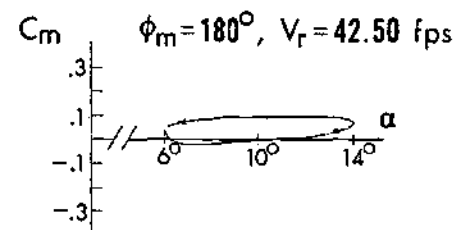
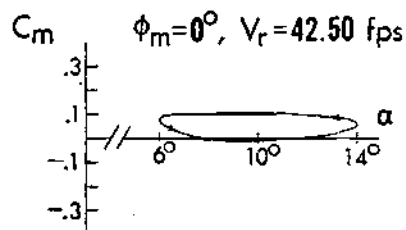
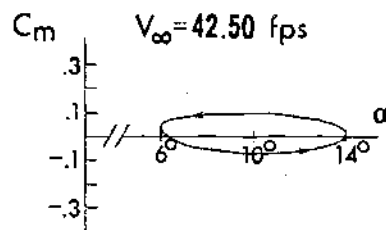
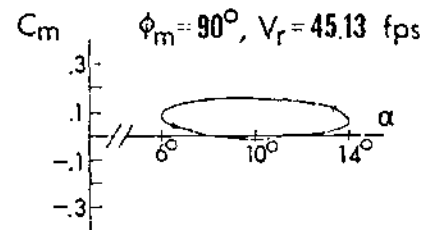
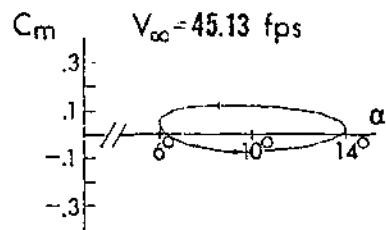
Figure 24. Sequential C_m vs. α for Oscillations About 18° at 6 Hz in Constant and 1 Hz Varying Freestreams



CONSTANT FREESTREAM

VARYING FREESTREAM

Figure 25. Sequential C_m vs. α for Oscillations About 10° at 6 Hz in Constant and 2 Hz Varying Freestreams



CONSTANT FREESTREAM

VARYING FREESTREAM

Figure 26. Sequential C_m vs. α for Oscillations About 10° at 12 Hz in Constant and 2 Hz Varying Freestreams

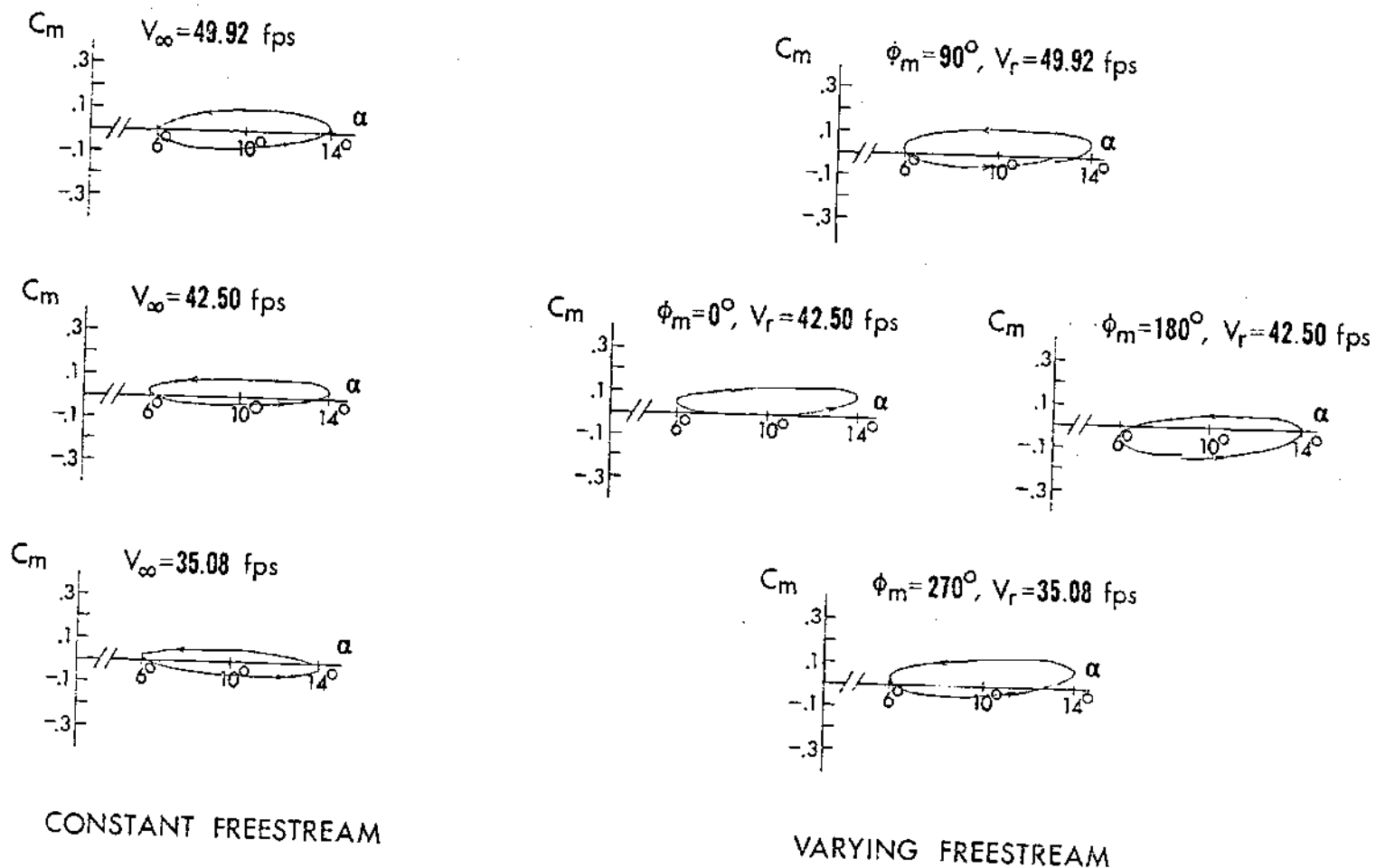


Figure 27. Sequential C_m vs. α for Oscillations About 10° at 12 Hz in Constant and 1 Hz Varying Freestreams

behavior of the moment curves. As might be expected, an instability showed up at the higher angles of attack, which were above the static stall angle. In addition, instabilities appeared at the lower angles. This was totally unexpected and unexplained.

At 14° , the motion turned completely unstable at all angles. As a progression from the 10° angle, this was not completely unexpected. However, since part of the angle of attack region was below the static stall angle, this case was not expected to be unstable throughout the entire range of angle of attack. Perhaps these results are due to the fact that the stall angle was at the extreme lower end of the angle traverse, and the flow never had time to reattach.

In Case 4, the mean angle of attack was 18° . Although the motion here was still unstable, it was somewhat less unstable than that with a 14° mean angle. The type of behavior implied here was also observed by several other investigators [3-4, 22-23], who found that the damping again became positive at very high angles of attack. Thus, it would be expected that if this investigation had tested even higher angles, the damping would have become less and less negative until it was indeed positive.

Model Frequency Effects

The increase in model frequency from 6 to 12 Hertz had a profound effect on the shapes of the moment curves. In Case 2 (Figure 22), the moment curves showed instabilities at high and low angles, and sensitivity to Reynolds number. By increasing only the model frequency for Case 7 (Figure 27), all traces of the instabilities were eliminated, and the curves reshaped to be remarkably elliptical. In addition, the curves seemed no longer to be sensitive to Reynolds number, as only dynamic

pressure effects appeared.

To verify that this change was due solely to the increase in model frequency, Cases 2 and 6 and Cases 5 and 6 were compared. In both Cases 2 (Figure 22) and 6 (Figure 26), the frequency ratio (R) was held at a constant value of 6, and still the curve shapes changed. Similar results were obtained in Cases 5 (Figure 25) and 6 (Figure 26) where, like Cases 2 (Figure 22) and 7 (Figure 27) the gust frequency was kept constant.

Frequency Ratio Effects

The frequency ratio, being the quotient of the model frequency and the gust frequency, shows the combined effect of the two parameters. However, because of the pronounced model frequency effects, it is difficult to get a true picture of the effect of frequency ratio. Cases 5-7 (Figures 25-27) show a progression in frequency ratio from 3 to 6 to 12.

One effect of the frequency ratio was apparent from these tests. As the ratio decreases, the moment curves become unsteadier. That is, they do not stay in one constant shape and position, but deform and change magnitude throughout the velocity cycle. Of these figures, only Figure 25 illustrates this phenomenon to any great extent. The large gaps in the traces between the beginnings and ends are indicative of this effect. Note also that the moment becomes larger than the constant freestream values at certain points (especially at $\phi_m = 180^\circ$). Although Figures 26 and 27 show none of this unsteadiness, it was observed on the oscilloscope as these cases were being run. In contrast to the large variations seen in Case 5, the curves viewed in Case 7 were nearly stationary.

Overall Varying Freestream Effects

In the preceding section, the effects noted resulted from the

presence of the velocity perturbations. These effects are noteworthy because they show that the velocity perturbations do have a significant effect on the C_m versus α curves.

For the test conditions observed, it does not appear that the varying freestream has an important effect on blade pitching stability. Under none of these conditions did the velocity variations appear to have either a stabilizing or destabilizing effect on the pitching oscillations. However, Case 5 (Figure 25) does give an indication that under conditions of small frequency ratio, large pitching moment changes could be induced, which might adversely affect the fatigue life of the blade, if not its structural integrity.

One additional characteristic appeared, to some extent, in all seven cases. Upon viewing the sequential curves, it seemed that the moment was lagging the velocity by approximately 90° . This effect can be seen by rotating the positions of the four varying freestream plots 90° in the counterclockwise direction. In this new position, nearly every curve matched up to the constant freestream curves better than when they were in their proper locations.

Comparison with Analytical Results

For each flow condition (Table 2), three curves were selected for comparison with analytical results. One curve was taken from the constant freestream data and two were taken from the varying freestream data. The constant freestream curve had a velocity of 42.50 feet per second. The varying freestream curves were selected so that one would have a large rate of change of velocity ($\phi_m = 0^\circ$), and the other a small rate of change of velocity ($\phi_m = 90^\circ$). The data were then compared to the results of two

analytical methods designed to predict the moment coefficient for an airfoil oscillating in a harmonically varying freestream.

Analytical Methods

The reasons for comparing these tests results to analytical results were twofold. First, it was necessary to find out if the data were consistent with previously documented work. If so, then the data could be regarded with some degree of confidence. Secondly, a comparison was desired among the test results and the two analytical results to see how they compared to each other. Good correlations could mean that a certain analytical method was a reliable way to predict moment loads.

One of the methods was an empirical method based on the data obtained by Carta et. al [22]. In that presentation, tables of normal force and pitching moment coefficients were tabulated for an airfoil oscillating in a constant freestream. These tables were fed into a computer program that could interpolate between the data points [28]. Also, this program was set up such that the stored data could be applied to harmonically varying freestreams, as well as constant freestreams.

The other analytical method, developed by Greenberg [29], was based on Theodorsen's treatment of unsteady potential flows [30]. While Theodorsen treated the problem of an airfoil undergoing simple harmonic oscillations in a constant airstream, Greenberg expanded the problem to include a harmonically pulsating freestream velocity. Greenberg's formulation used the basic form of the Theodorsen function, $C(k)$, but had three different reduced frequencies for which $C(k)$ was tabulated. These three were the reduced frequency of the airfoil, the reduced frequency of the airstream, and the sum of the two. All were based on the mean velocity

of the airstream. The computer program which computed the moments and normal forces was written by Malone [25].

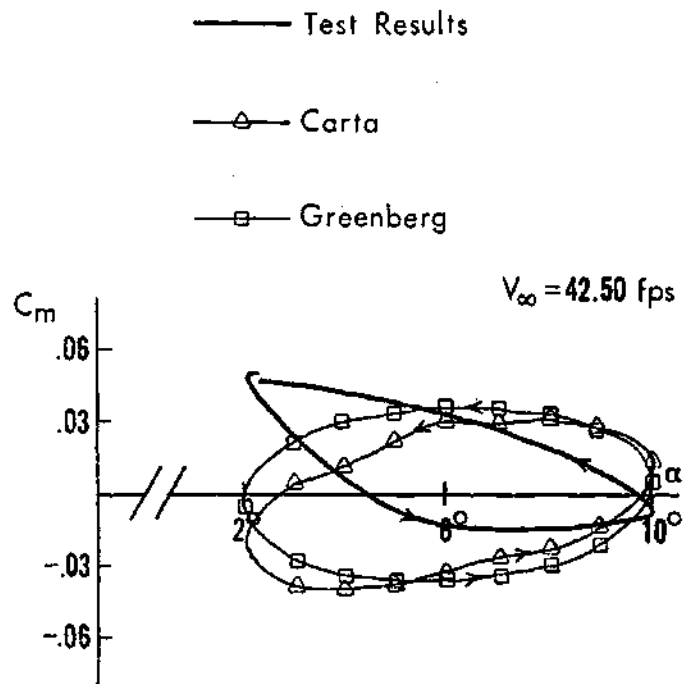
Discussion

The curves showing the analytical results and experimental data described above, are in Figures 28-34. In keeping with the format established for the sequential C_m vs α curves, the constant freestream pitching moment data are on the left, with the varying freestream data on the right.

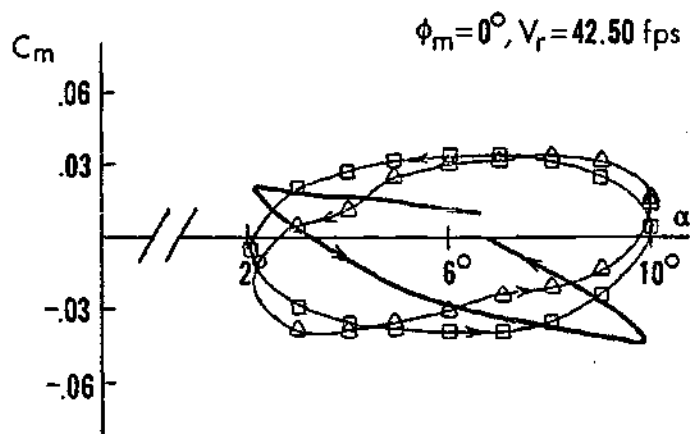
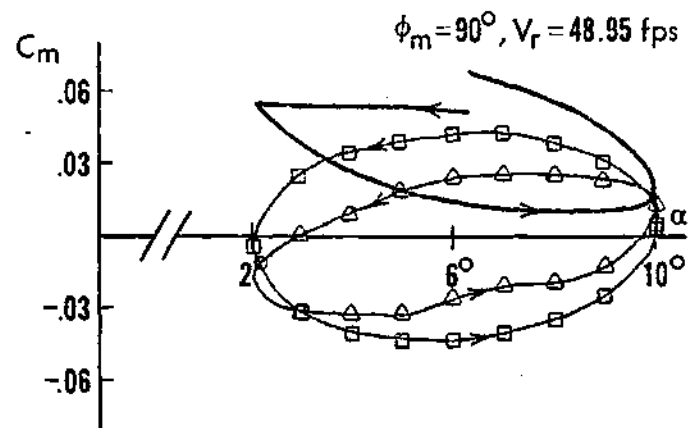
Figure 28 is in the comparison for Case 1 (see Table 2). This case is a potential flow condition, so all three curves in each plot would be expected to look very much the same. The Carta and Greenberg curves are nearly equivalent, but the test results show some noticeable differences. Although the test data are of the same magnitude as the other curves, they are somewhat less elliptical. Also, the analytical curves show a slight tilt to the left, while the experimental curves tilt to the right. A possible explanation for this is that when the still air moment was being eliminated, the inertial term was improperly adjusted.

As would be expected, the Greenberg curves remain elliptical in Figures 29, 31, and 32, and do not compare well to the experimental curves in shape. They are, however, quite similar in magnitude. In Figure 30, there is no potential flow curve, since the computer program could not process this case. Judging from the other curves, it would probably be very much similar to the potential flow curves in Figure 31.

The Carta curves in Figures 29-32 do not compare well with the experimental curves either. However, because of the difference in Reynolds number, this was to be expected. The gaps in Figure 31, are due to the

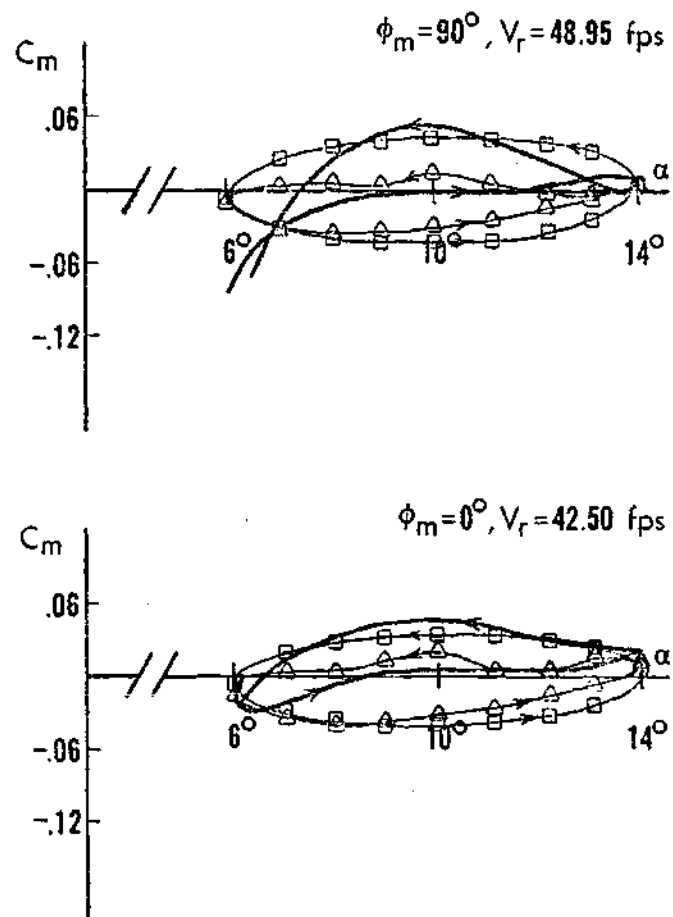
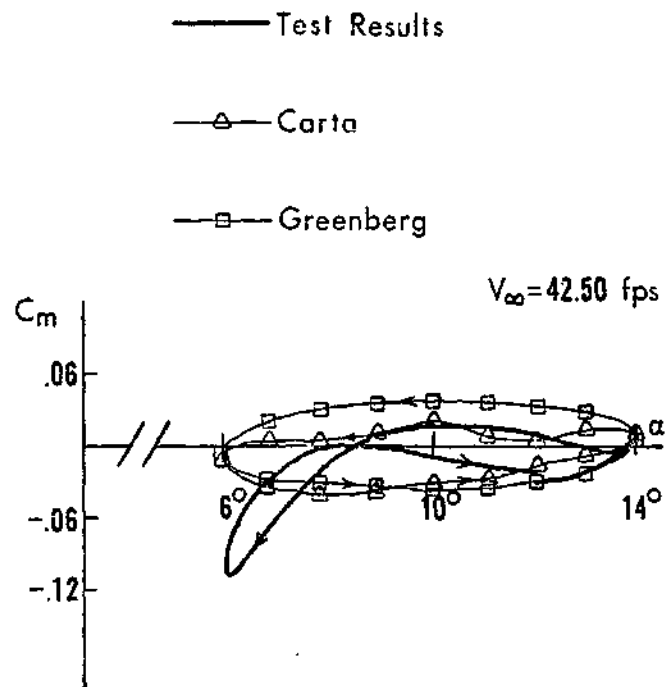


CONSTANT FREESTREAM



VARYING FREESTREAM

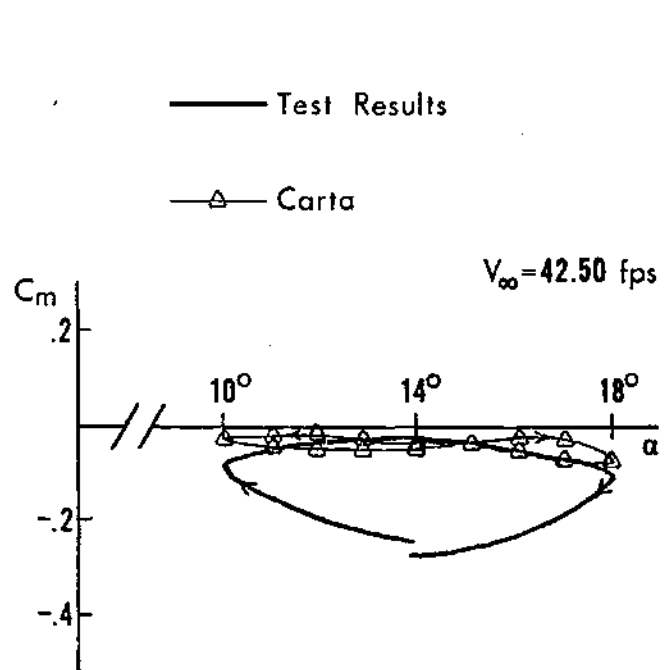
Figure 28. Analytical and Experimental C_m vs. α for Oscillations About 6° at 6 Hz^m in Constant and 1 Hz Varying Freestreams



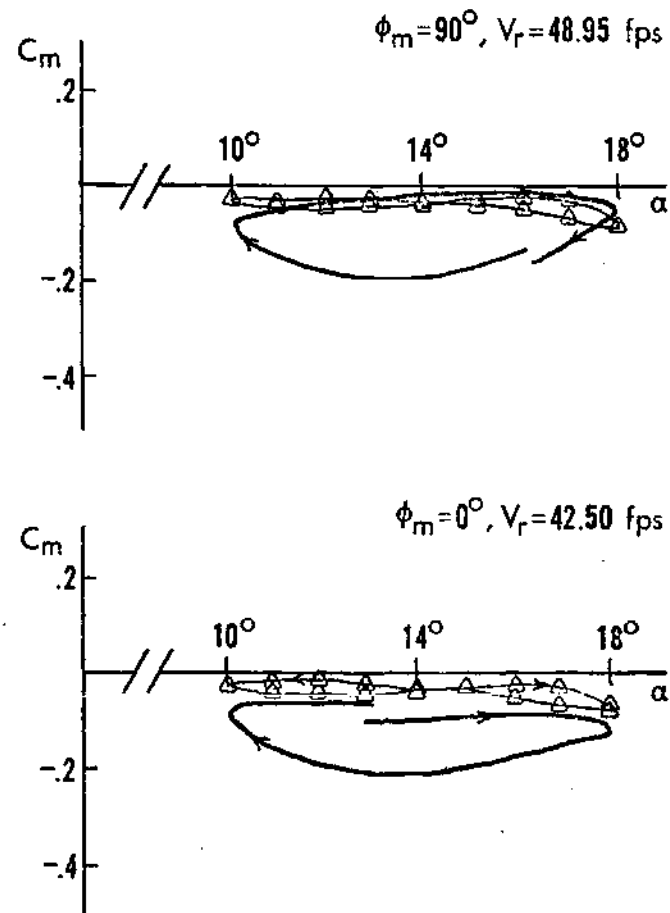
CONSTANT FREESTREAM

VARYING FREESTREAM

Figure 29. Analytical and Experimental C_m vs. α for Oscillations About 10° at 6 Hz in Constant and 1 Hz Varying Freestreams

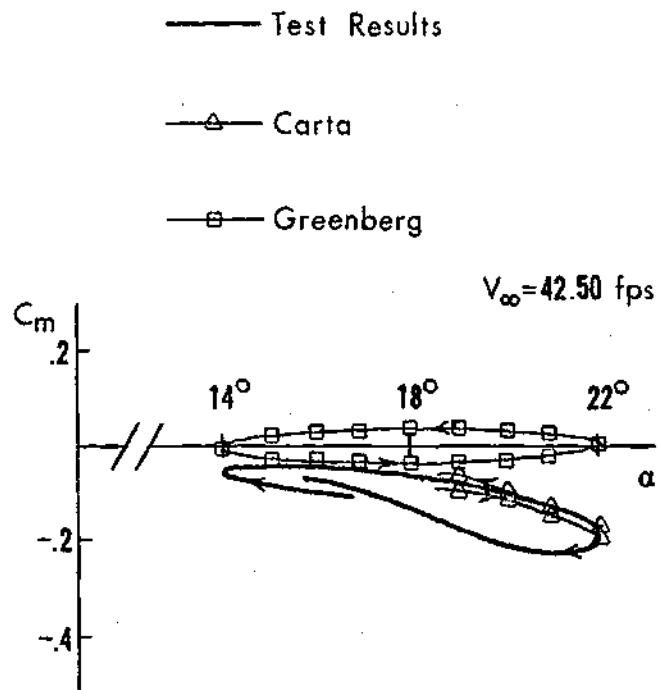


CONSTANT FREESTREAM

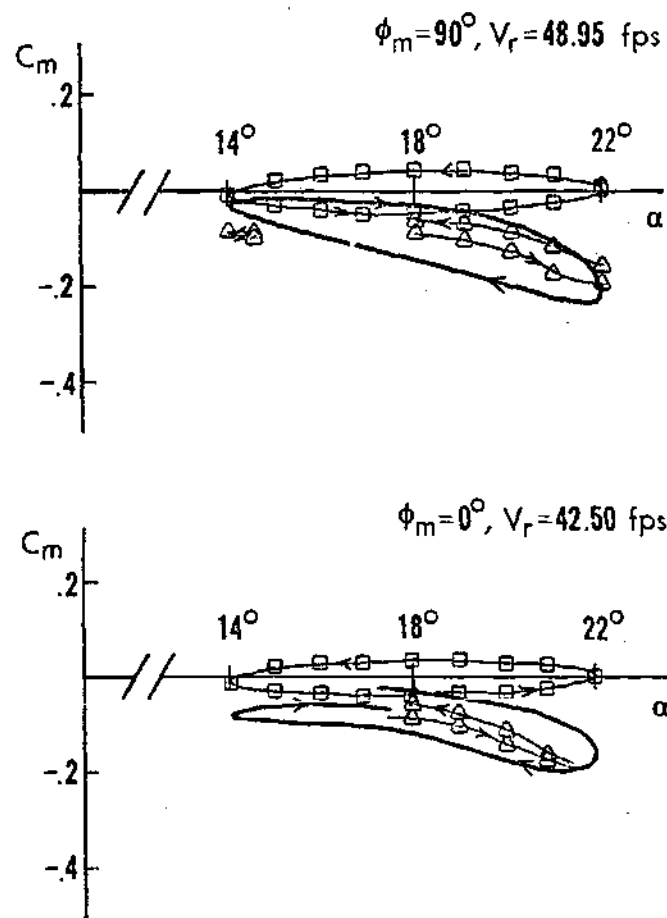


VARYING FREESTREAM

Figure 30. Analytical and Experimental C_m vs. α for Oscillations About 14° at 6 Hz in Constant and 1 Hz Varying Freestreams

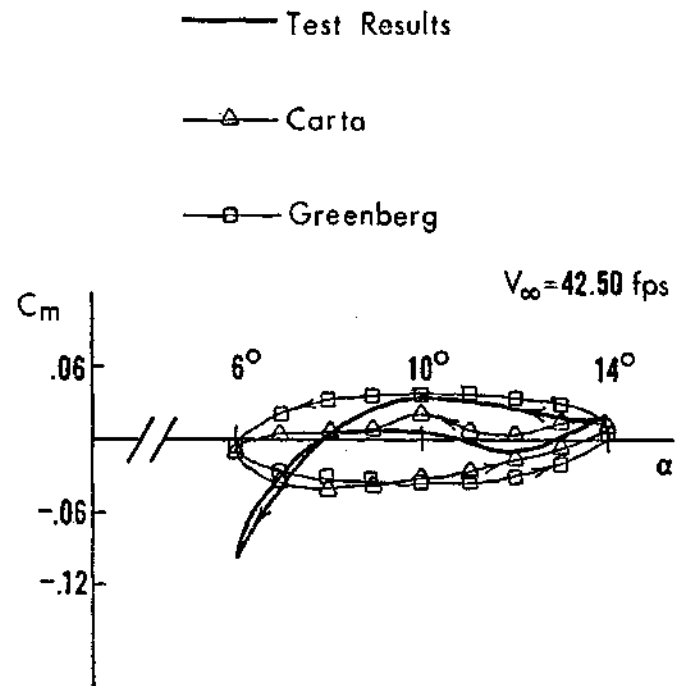


CONSTANT FREESTREAM

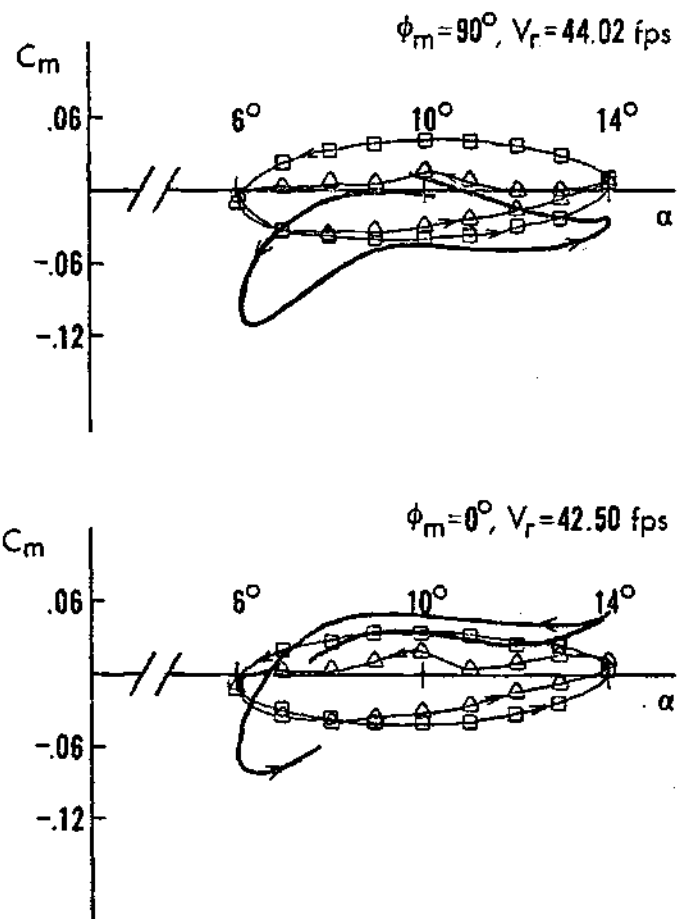


VARYING FREESTREAM

Figure 31. Analytical and Experimental C_m vs. α for Oscillations About 18° at 6 Hz in Constant and 1 Hz Varying Freestreams

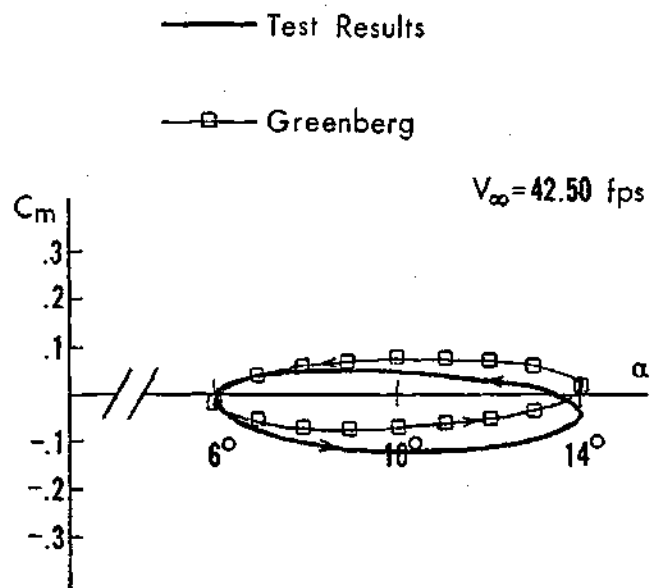


CONSTANT FREESTREAM

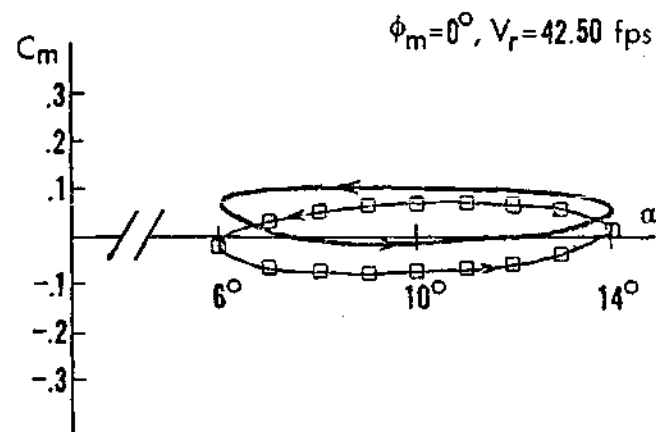
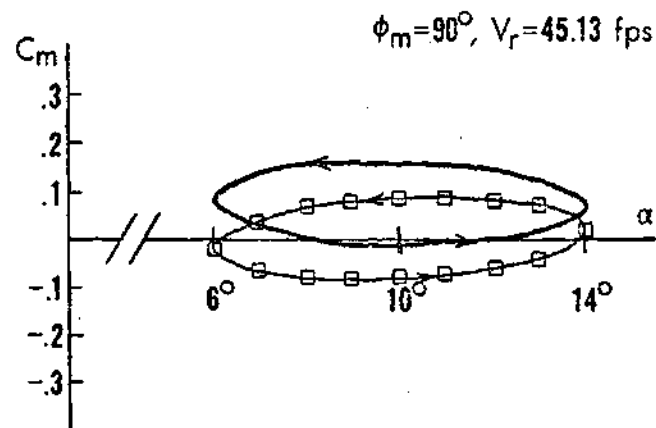


VARYING FREESTREAM

Figure 32. Analytical and Experimental C_m vs. α for Oscillations About 10° at 6 Hz in Constant and 2 Hz Varying Freestreams

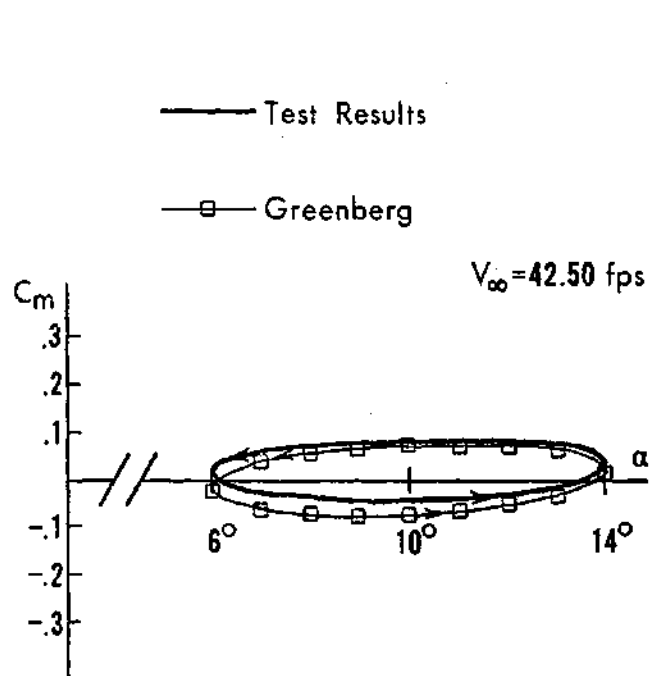


CONSTANT FREESTREAM

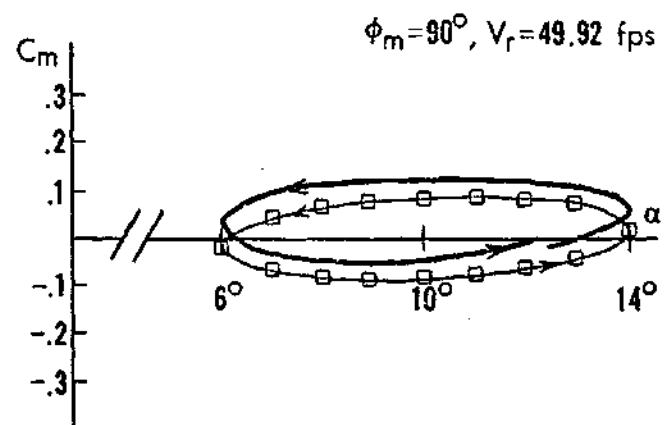


VARYING FREESTREAM

Figure 33. Analytical and Experimental C_m vs. α for Oscillations About 10° at 12 Hz in Constant and 2 Hz Varying Freestreams



CONSTANT FREESTREAM



VARYING FREESTREAM

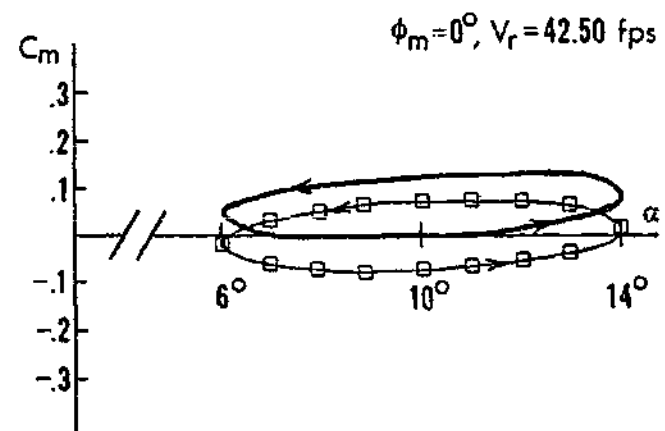


Figure 34. Analytical and Experimental C_m vs. α for Oscillations About 10° at 12 Hz in Constant and 1 Hz Varying Freestreams

computer program not being able to handle those points.

In Figures 33 and 34, the Greenberg potential flow theory matches up remarkably well with the test results. In fact, were it not for the random vertical shifts in the experimental data, they would be virtually identical. The Carta curves were not included for these two cases since the reduced frequency of the model oscillations exceeded his test conditions.

CHAPTER VI

CONCLUSIONS AND RECOMMENDATIONS

Using the Georgia Tech Low Turbulence Wind Tunnel, equipped with an axial gust generator, measurements were taken of the aerodynamic pitching moment acting on an airfoil model undergoing simple harmonic pitching motions while immersed in a harmonically varying freestream. The data were reduced on-line by using an operational analog computer and other electronic equipment. For the purposes of analysis and discussion, the results were presented as single, complete model cycles in selected regions of the velocity curve.

Conclusions

1. The varying freestream velocity was found to have a significant effect on the C_m vs. α curves. For the conditions tested, it did not radically affect the pitching stability, but did affect the shapes and magnitudes of the curves.
2. The stability of the pitching motions was much more strongly dependent on the model parameters than on the gust parameters. Changes in mean angle of attack had pronounced effects on the stability, while the gust frequency and frequency ratio had comparatively little effect.
3. Under conditions of small frequency ratio, the moment loads observed in the varying freestream exceeded those observed in the constant freestream. Thus, load predictions based on constant freestream data might tend to be unconservative.

4. Comparisons with Greenberg's potential flow theory showed that good predictions of the C_m vs. α curves could be obtained for the higher mean angles at high frequencies, as well as for mean angles well below stall.

5. The processes involved in dynamic stall were observed to be highly nonlinear and random in behavior.

6. The analog computer proved to be a valuable and versatile tool in all phases of data acquisition, reduction, and interpretation. Its use made it possible to get results that could not have been obtained otherwise.

Recommendations

1. For any further investigations, it would be advantageous to have a means for controlling the relationship of the velocity and model oscillations. Perhaps using a single motor to drive both the gust generator and the model would allow the relationship to be controlled.

2. A significant contribution to the lack of controllability of the model frequency was made by the presence of oscillatory loads on the motor. This situation might be improved by attaching a massive flywheel to the motor shaft to provide an inertial energy reservoir.

3. Considerable improvement in the model support and drive system could be made by redesigning it to eliminate as many of the bearings as possible. This could also reduce the noise and improve the quality of the moment data.

4. Future, in-depth studies of dynamic stall should be performed in a facility that can provide a larger test-section velocity. The resulting increase in dynamic pressure would improve the aerodynamic-to-

inertial force ratio, and the Reynolds number could be more realistic (e.g. 10^6).

PART II

UNSTEADY DRAG

CHAPTER VII

INTRODUCTION

In the development of a helicopter rotor system, aeroelastic phenomena not found in conventional, fixed-wing aircraft are often encountered. One such phenomenon is in-plane, or lead-lag motion. This can occur alone, or coupled with torsional and/or flapping oscillations. The presence and degree of coupling depend on the geometry, elastic properties, and aerodynamic environment of the rotor system.

It is well-known that the primary load governing pitch is the pitching moment, and that flapping is affected most by lift. Similarly, the drag force has a major influence on lead-lag oscillations. The unsteady nature of the motion and environment of a rotor blade demands that the forces on it be considered as unsteady. While there are analytical methods available for predicting the unsteady lift and moment on an airfoil both above and below stall [12,17-24,28-30], and experimental data for verification [3-4,7-12], no such methods are available to predict unsteady drag. In addition, there are little reliable, experimental, unsteady data available on which to base an empirical technique for predicting unsteady drag.

Those measurements which have been taken are, for the most part, of questionable accuracy or limited in scope. Also, they were all obtained for an airfoil, oscillating in pitch, in a freestream of constant velocity. In their study, Liiiva and Davenport [4] measured only

the average drag per pitch cycle. This was done by slowly traversing a pitot-static probe across the wake to measure the momentum deficit. They did not attempt to obtain the instantaneous drag. Windsor [7], however, did try to obtain instantaneous drag data with the use of a strain gage balance. Due to a lack of sensitivity and the low natural frequency of model and suspension system, he was only able to observe trends and could not make accurate measurements. The most recent effort was that of Philippe and Sagner [12]. They appeared to have had success in measuring the drag, but presented very little data. Apart from these three investigations, no other data could be found.

A survey of methods used by the helicopter industry to predict rotor loads was conducted by Ormiston [31]. It showed what effect the absence of information concerning unsteady drag had on the aerodynamic models being used. Below stall, a large majority of the nine companies surveyed used some form of Theodorsen aerodynamics, while others used the data obtained by Carta et al. [22] for unsteady lift and moment. However, steady-state or constant friction drag were the only approximations used for these same conditions. In the stall regime, several different methods were used to predict lift and moment, including Carta [22] and Harris et al. [18]. With only one exception, those that included stall effects used the steady-state drag or the approximation suggested by Harris et al. [18]. This approximation also used the static drag curves, but instead of the blade angle of attack, an angle was used which was a function of reduced frequency, Mach number, airfoil shape, and azimuthal variation in blade angle of attack.

The lack of unsteady drag data is also reflected in research efforts.

Hohenemser and Heaton [32] were able to neglect drag in their analysis of second-order flap-lag coupling by considering normal and tangential blade forces. Elman et al. [33] neglected drag in their analysis of flap-lag dynamics, even though it was included in the equations as derived by Arcidiacono [34]. In most analyses of rotors with flapping and lead-lag degrees of freedom, the drag coefficient has merely been regarded as a constant, equal to the profile drag coefficient [34-41].

Efforts have been made, however to employ more accurate representations of the drag forces in analyzing the dynamics of a rotor system. Chou [42] represented the drag coefficient by a power series in the unsteady pitch angle, retaining only the zeroth and second-order terms. Another series representation was used by Ormiston and Bousman [43], who employed a two term Taylor's series. The series coefficients were determined from airfoil section data. Experimental drag data were also incorporated into Crimi's computer analysis [44] in order to account for nonlinear drag effects.

In an attempt to include unsteady effects, Bellinger [45] came up with a scheme to synthesize an unsteady drag coefficient for pitching oscillations. His method was based on the assumption that unsteady lift and drag are related in a manner similar to the relationship between steady lift and drag. The drag coefficient was obtained by adding an empirical incremental value, which was a function of lift, to the steady-state drag coefficient. It was reported that this method gave quantitatively good results for the limiting cases of high and low frequency oscillations. However, there was no way to verify the results because of the absence of experimental data.

The lack of an accurate representation of unsteady drag does not, of course, invalidate the results of all of these analyses. They have provided insights into various aspects of the dynamics of rotor systems. It can be seen, however, that in order to make a complete analysis of in-plane motion, a method for representing the unsteady drag is needed. In addition, there is a need for experimental data, with which any forthcoming theory can be verified. This data could also be used in an empirical method similar to that of Carta et al. [22] until a suitable analytical technique can be developed.

The objective of this investigation was to obtain some unsteady drag data experimentally, and to compare it with a quasi-steady approximation. Keeping in mind the influence of drag on in-plane motion, the flow situation to be modeled was that of a blade undergoing lead-lag oscillations while on a hovering helicopter. To accomplish this, a stationary airfoil model was placed in an airstream which had simple harmonic, streamwise velocity perturbations impressed on the mean velocity. The unsteady lift and drag forces were then measured.

Using an equivalent displacement derived from the velocity perturbations, the lift and drag derivatives with respect to in-plane oscillations were computed for various angles of attack and reduced frequencies. With this formulation, it was hoped that the derivatives would be functions of only reduced frequency, at a particular angle of attack. In addition, comparisons were made to the unsteady drag derivatives using a quasi-steady approximation, and to the unsteady lift derivatives using both the quasi-steady approximation and a potential flow approximation.

CHAPTER VIII

MODIFIED AXIAL GUST GENERATOR

In order to measure the unsteady drag of frequencies comparable to those encountered in the lead-lag oscillations of a rotor blade, it was necessary to modify the axial gust generator. The modification involved replacing the original motor shaft pulley, which had a diameter of 2.5 inches, with one having a diameter of 6.8 inches. In this way, gust frequencies up to 6 Hertz could be obtained.

The remainder of the wind tunnel facilities, as described in Chapter II remained essentially the same. One change that was made was the wire on the tip of the hot-wire probe. The wire used previously broke.

Hot-wire Calibration

The procedure used to calibrate the hot-wire anemometer for the new probe wire was identical to that described in Chapter II. The calibration curve for this wire is shown in Figure 35.

Due to the strain put on the wire and, perhaps, a weak weld, this wire lasted only through the calibration of the 50% vanes. The 60% and 70% vane calibrations were carried out using a new wire, having the calibration curve shown in Figure 36.

Gust Generator Calibration

The calibration of the gust generator for the 50%, 60%, and 70% vanes in the frequency range of 1 to 6 Hertz was a relatively straight-

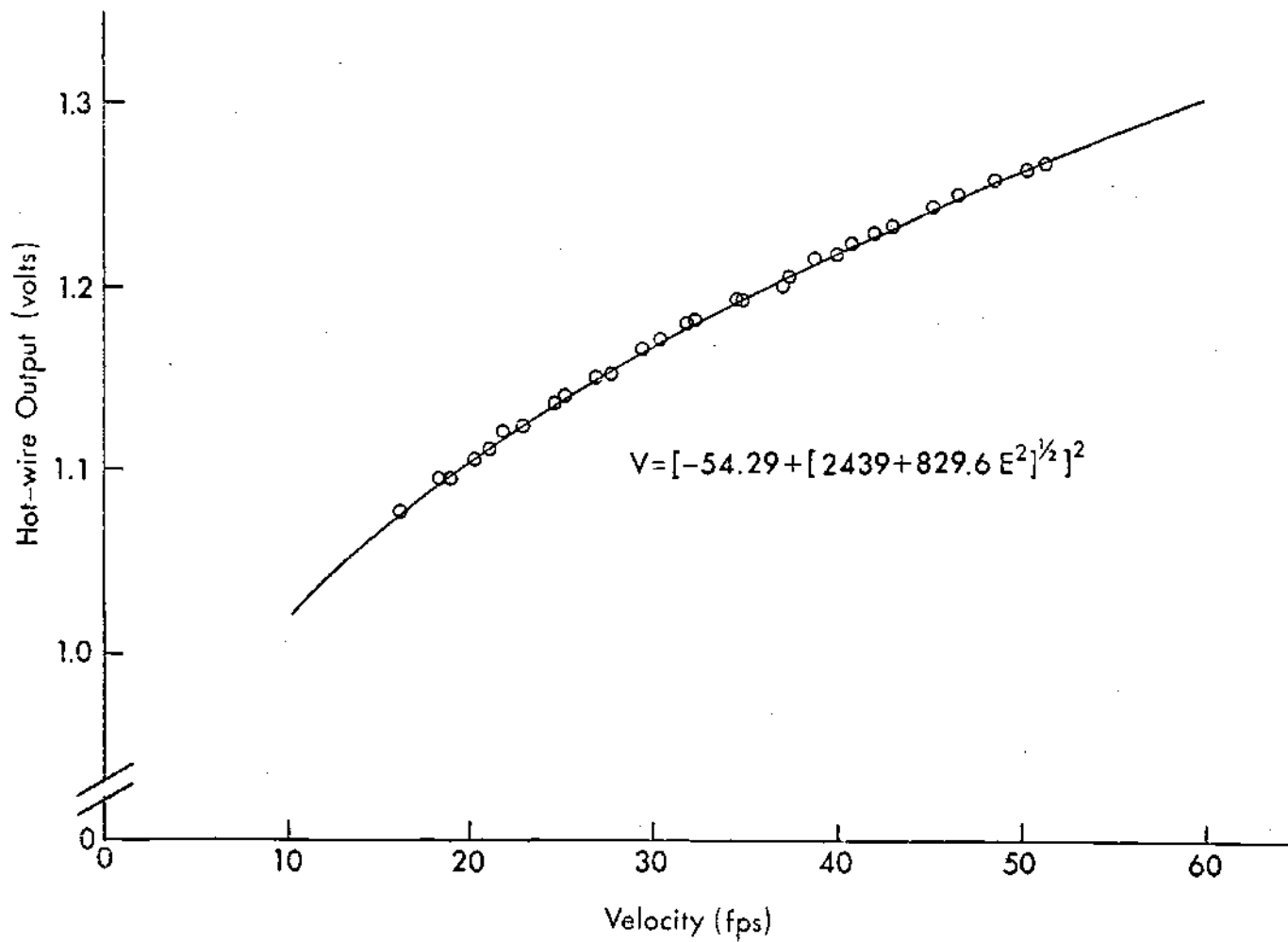


Figure 35. Hot-wire Calibration Curve No. 2

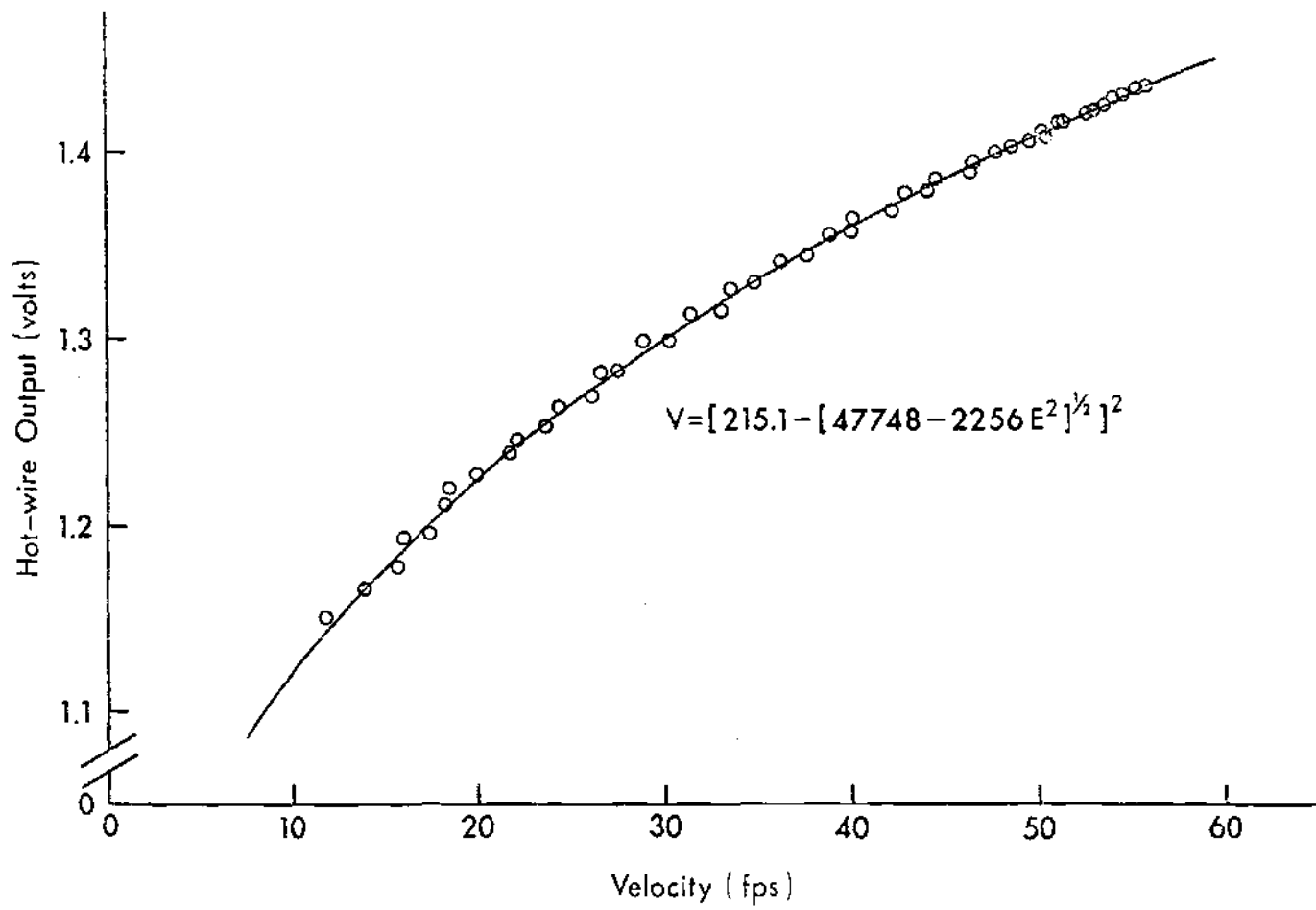


Figure 36. Hot-wire Calibration Curve No. 3

forward procedure. For each set of vanes, data were taken at each of six frequencies. At each frequency, thirty points were selected at random and the maximum and minimum anemometer voltages at each point were recorded.

To make these measurements, the equipment schematically shown in Figure 37 was used. Because of the higher frequencies attained here, it was not possible to use an x-y plotter to record the data, as Malone [25] had done. Thus, the oscilloscope was used.

The problem that then arose was to get sufficient sensitivity. Ideally, the anemometer output should be read to 4 digits, but the oscilloscope could only be accurate to 2.5 digits. To get additional sensitivity, the analog computer was used to subtract a known voltage (1.100 volts) from the anemometer output. The difference was then displayed on the oscilloscope, giving accuracy to 3.5 digits.

Once the data for all three sets of vanes had been collected, it was fed into a digital computer, which determined the operational curves.

Computer Cross-Plotting Program

In order to obtain the operational curves for the gust generator, it was necessary to cross-plot the calibration data. By this method, it was possible to get twenty-one curves of mean velocity versus amplitude, in the interval of 1 to 6 Hertz, for each set of vanes.

Because of the large quantity of raw data and the number of computations that would have had to be performed, a computer program was written to do the cross-plotting (see Appendix A). The program was based on a subroutine that, by a least-squares approximation, fit first-order and second-order curves to the data it received. Then, it chose

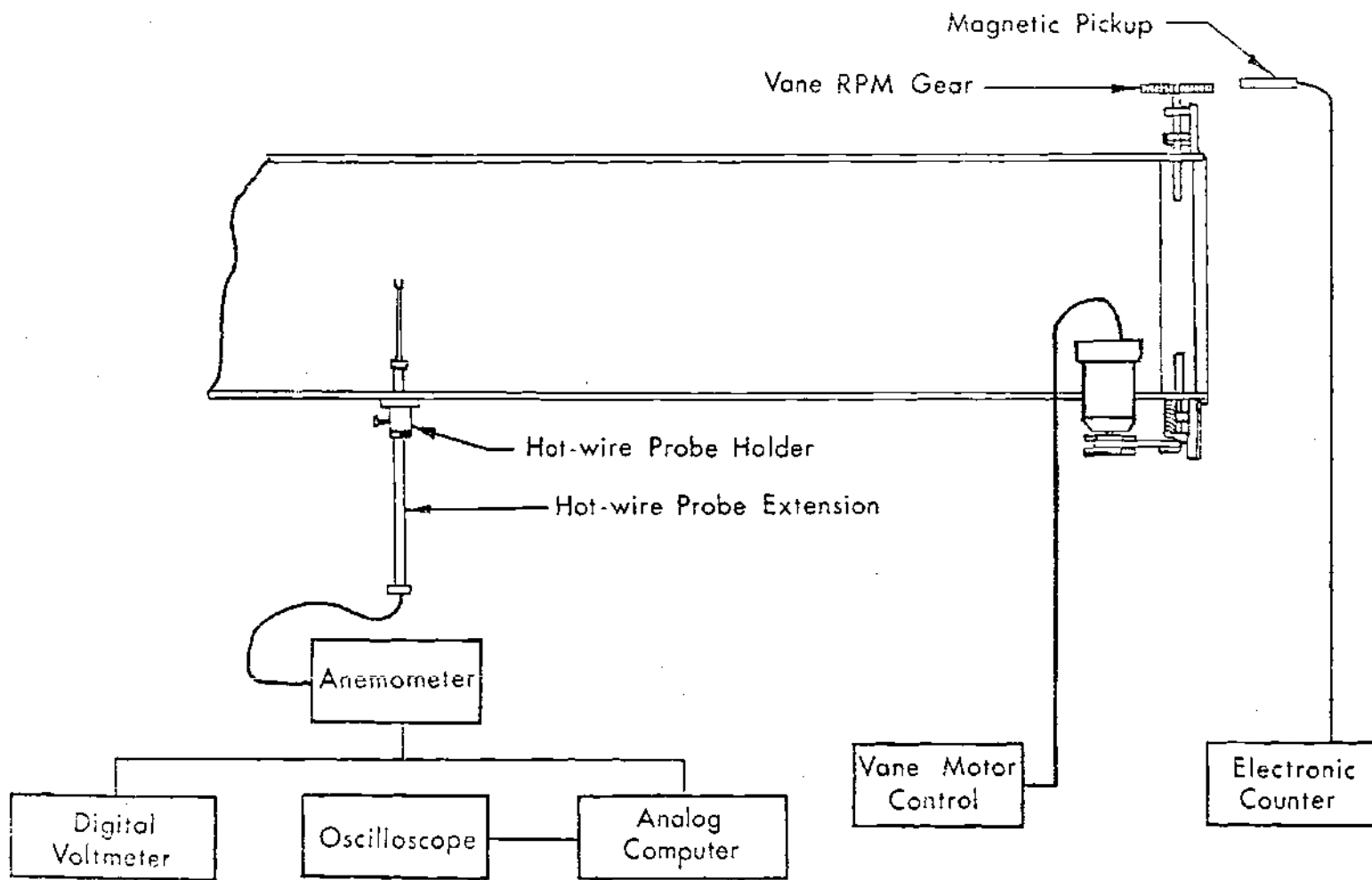


Figure 37. Equipment for the Gust Generator Calibration

the better fit. This subroutine was used throughout the program for all curve fitting.

Briefly, the program converted the hot-wire voltages to velocities, and computed the mean velocity and gust amplitude of each data point. After fitting curves to the data at each gust frequency, it mapped the curves from the mean velocity-amplitude plane to the gust frequency-amplitude plane. Least-squares curves were then fitted to the mapped points, giving a set of gust amplitude versus gust frequency curves at constant mean velocities. Finally, these curves were mapped back into the mean velocity-amplitude plane, where least-squares approximations were again applied. It was this set of curves that became the operational data for the gust generator.

The operational curves obtained by the above method for the 50%, 60%, and 70% vanes are listed in Tables 3-5. The operational limits of the gust generator are illustrated in Figure 38. Note that, as before, the upper curve of each region is at the lowest frequency (1 Hz), and that the higher frequency curves fill in below.

Observations

The first observation made in connection with the operation of the gust generator concerns phase shifts. That is, the existence or absence of any phase differences between the velocity at the probe location and the velocity at the model location. To this point, it had been assumed that there was no such phase shift present, since there was no apparent reason for one to exist. This possibility was, never-the-less, checked out.

Table 3. Gust Generator Operational Curves
for the 50% Vanes (1-6 Hz)

ω_v (Hz)	Gust Amplitude (fps)
1.00	$V_1 = - .54397 + .08731 V_o + .00129 V_o^2$
1.25	$V_1 = - .36970 + .06405 V_o + .00157 V_o^2$
1.50	$V_1 = - .21063 + .04268 V_o + .00184 V_o^2$
1.75	$V_1 = .06677 + .02322 V_o + .00207 V_o^2$
2.00	$V_1 = .06190 + .00564 V_o + .00229 V_o^2$
2.25	$V_1 = .17536 - .01003 V_o + .00249 V_o^2$
2.50	$V_1 = .27363 - .02381 V_o + .00265 V_o^2$
2.75	$V_1 = .35669 - .03569 V_o + .00279 V_o^2$
3.00	$V_1 = .42456 - .04567 V_o + .00291 V_o^2$
3.25	$V_1 = .47722 - .05376 V_o + .00300 V_o^2$
3.50	$V_1 = .51469 - .05995 V_o + .00308 V_o^2$
3.75	$V_1 = .53695 - .06425 V_o + .00312 V_o^2$
4.00	$V_1 = .54402 - .06665 V_o + .00315 V_o^2$
4.25	$V_1 = .53588 - .06715 V_o + .00315 V_o^2$
4.50	$V_1 = .51254 - .06575 V_o + .00312 V_o^2$
4.75	$V_1 = .47401 - .06246 V_o + .00308 V_o^2$
5.00	$V_1 = .42027 - .05723 V_o + .00301 V_o^2$
5.25	$V_1 = .35134 - .05019 V_o + .00291 V_o^2$
5.50	$V_1 = .26720 - .04121 V_o + .00279 V_o^2$
5.75	$V_1 = .16786 - .03033 V_o + .00265 V_o^2$
6.00	$V_1 = .05333 - .01756 V_o + .00248 V_o^2$

Table 4. Gust Generator Operational Curves
for the 60% Vanes (1-6 Hz)

ω_v (Hz)	Gust Amplitude (fps)
1.00	$V_1 = - .77578 + .14407 V_o + .00195 V_o^2$
1.25	$V_1 = - .65442 + .11857 V_o + .00228 V_o^2$
1.50	$V_1 = - .54427 + .09527 V_o + .00258 V_o^2$
1.75	$V_1 = - .44533 + .07417 V_o + .00284 V_o^2$
2.00	$V_1 = - .35760 + .05526 V_o + .00308 V_o^2$
2.25	$V_1 = - .28108 + .03855 V_o + .00328 V_o^2$
2.50	$V_1 = - .21577 + .02403 V_o + .00345 V_o^2$
2.75	$V_1 = - .16167 + .01171 V_o + .00359 V_o^2$
3.00	$V_1 = - .11878 + .00158 V_o + .00370 V_o^2$
3.25	$V_1 = - .08710 - .00635 V_o + .00378 V_o^2$
3.50	$V_1 = - .06662 - .01208 V_o + .00382 V_o^2$
3.75	$V_1 = - .05736 - .01562 V_o + .00383 V_o^2$
4.00	$V_1 = - .05930 - .01696 V_o + .00381 V_o^2$
4.25	$V_1 = - .07246 - .01611 V_o + .00376 V_o^2$
4.50	$V_1 = - .09682 - .01306 V_o + .00368 V_o^2$
4.75	$V_1 = - .13239 - .00782 V_o + .00356 V_o^2$
5.00	$V_1 = - .17917 - .00038 V_o + .00341 V_o^2$
5.25	$V_1 = - .23717 + .00926 V_o + .00323 V_o^2$
5.50	$V_1 = - .30637 + .02109 V_o + .00302 V_o^2$
5.75	$V_1 = - .38678 + .03512 V_o + .00277 V_o^2$
6.00	$V_1 = - .47840 + .05134 V_o + .00250 V_o^2$

Table 5. Gust Generator Operational Curves
for the 70% Vanes (1-6 Hz)

ω_v (Hz)	Gust Amplitude (fps)
1.00	$V_1 = - 1.44200 + .28847 V_o + .00189 V_o^2$
1.25	$V_1 = - 1.28242 + .24952 V_o + .00264 V_o^2$
1.50	$V_1 = - 1.13935 + .21419 V_o + .00332 V_o^2$
1.75	$V_1 = - 1.01288 + .18249 V_o + .00391 V_o^2$
2.00	$V_1 = - .90274 + .15442 V_o + .00442 V_o^2$
2.25	$V_1 = - .80922 + .12997 V_o + .00485 V_o^2$
2.50	$V_1 = - .73221 + .10915 V_o + .00520 V_o^2$
2.75	$V_1 = - .67171 + .09195 V_o + .00546 V_o^2$
3.00	$V_1 = - .62772 + .07838 V_o + .00565 V_o^2$
3.25	$V_1 = - .60024 + .06843 V_o + .00575 V_o^2$
3.50	$V_1 = - .58928 + .06211 V_o + .00577 V_o^2$
3.75	$V_1 = - .59482 + .05942 V_o + .00571 V_o^2$
4.00	$V_1 = - .61688 + .06035 V_o + .00557 V_o^2$
4.25	$V_1 = - .65545 + .06491 V_o + .00534 V_o^2$
4.50	$V_1 = - .71054 + .07309 V_o + .00504 V_o^2$
4.75	$V_1 = - .78213 + .08490 V_o + .00465 V_o^2$
5.00	$V_1 = - .87024 + .10033 V_o + .00418 V_o^2$
5.25	$V_1 = - .97486 + .11940 V_o + .00363 V_o^2$
5.50	$V_1 = - 1.09606 + .14208 V_o + .00300 V_o^2$
5.75	$V_1 = - 1.23366 + .16839 V_o + .00228 V_o^2$
6.00	$V_1 = - 1.38785 + .19833 V_o + .00149 V_o^2$

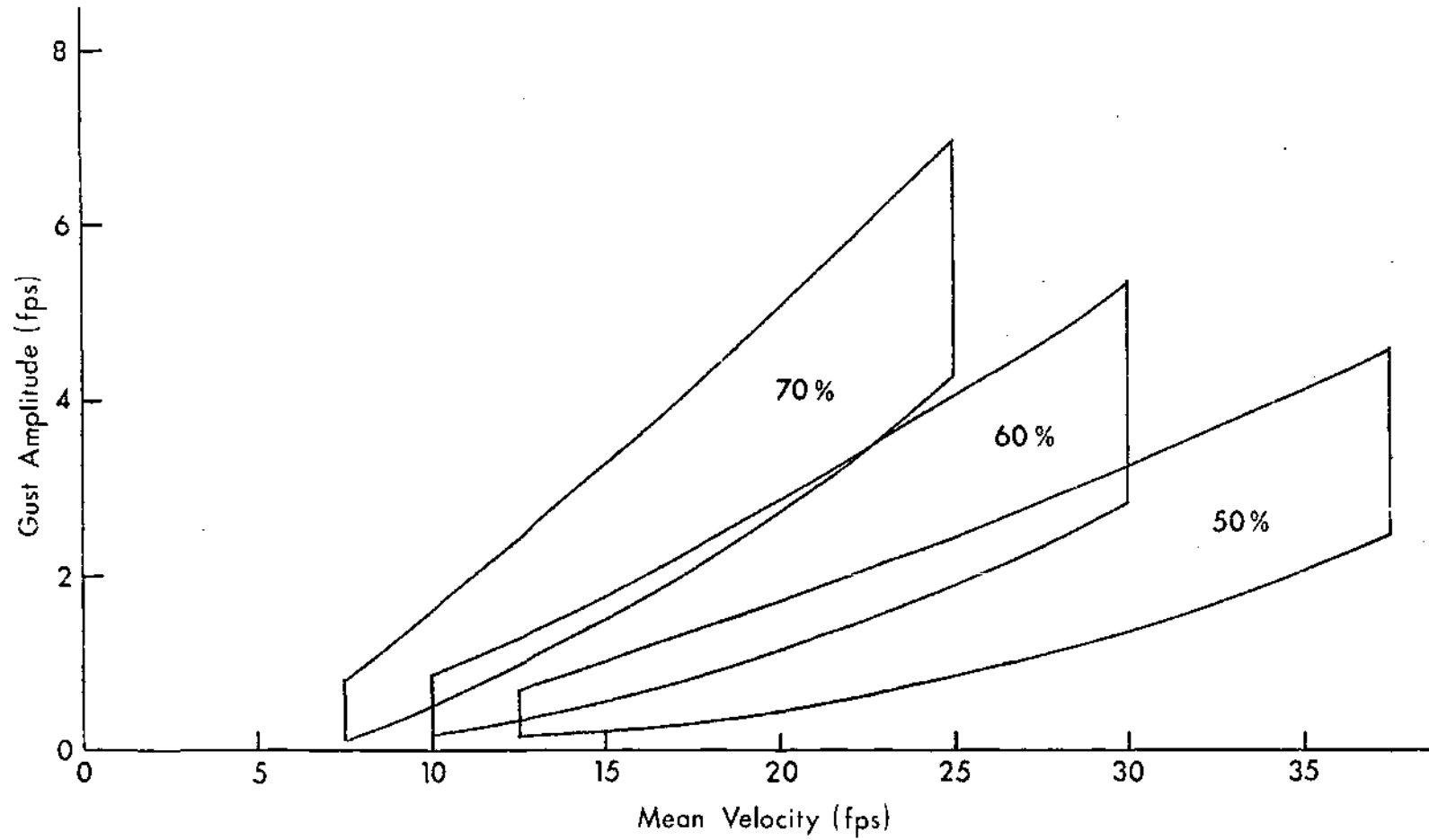


Figure 38. Gust Generator Operational Limits (1-6 Hz)

This check simply involved placing one probe at each of the two locations and viewing the outputs simultaneously. The test was performed at various mean velocities, gust amplitudes, and gust frequencies. No phase shifts were observed for any conditions, proving the original assumption to be valid.

The other observation concerns the operational curves obtained by the cross-plotting technique. Figure 39 shows these curves for the 70% vanes, and is representative of the other two sets of vanes. It can be seen that gust amplitude decreases with increasing gust frequency up to 4.5 Hertz, and then starts to increase. From a physical viewpoint, this is quite unexpected, as it would have been anticipated that the amplitudes continue decreasing with increasing frequency.

While there is no physical explanation for this behavior, there is a good reason for it. Looking at Figure 40, the experimental curves for the same set of vanes, it can be seen that the 3.0, 4.0, 5.0, and 6.0 Hertz curves are closely grouped, and even overlap one another. Since the standard deviations for all of the curves were approximately 0.1 fps. it is not a case of scattered data at the higher frequencies. The true curves were simply so closely spaced that the experimental methods available could not accurately make any distinctions among them. Thus, the good separation at low frequencies and the grouping at the higher frequencies.

The cross-plotting program could, of course, do nothing but process the data given to it. The operational curves of Figure 39 were the results. This is not to say that all of those curves are meaningless, because they do compare well with the experimental data.

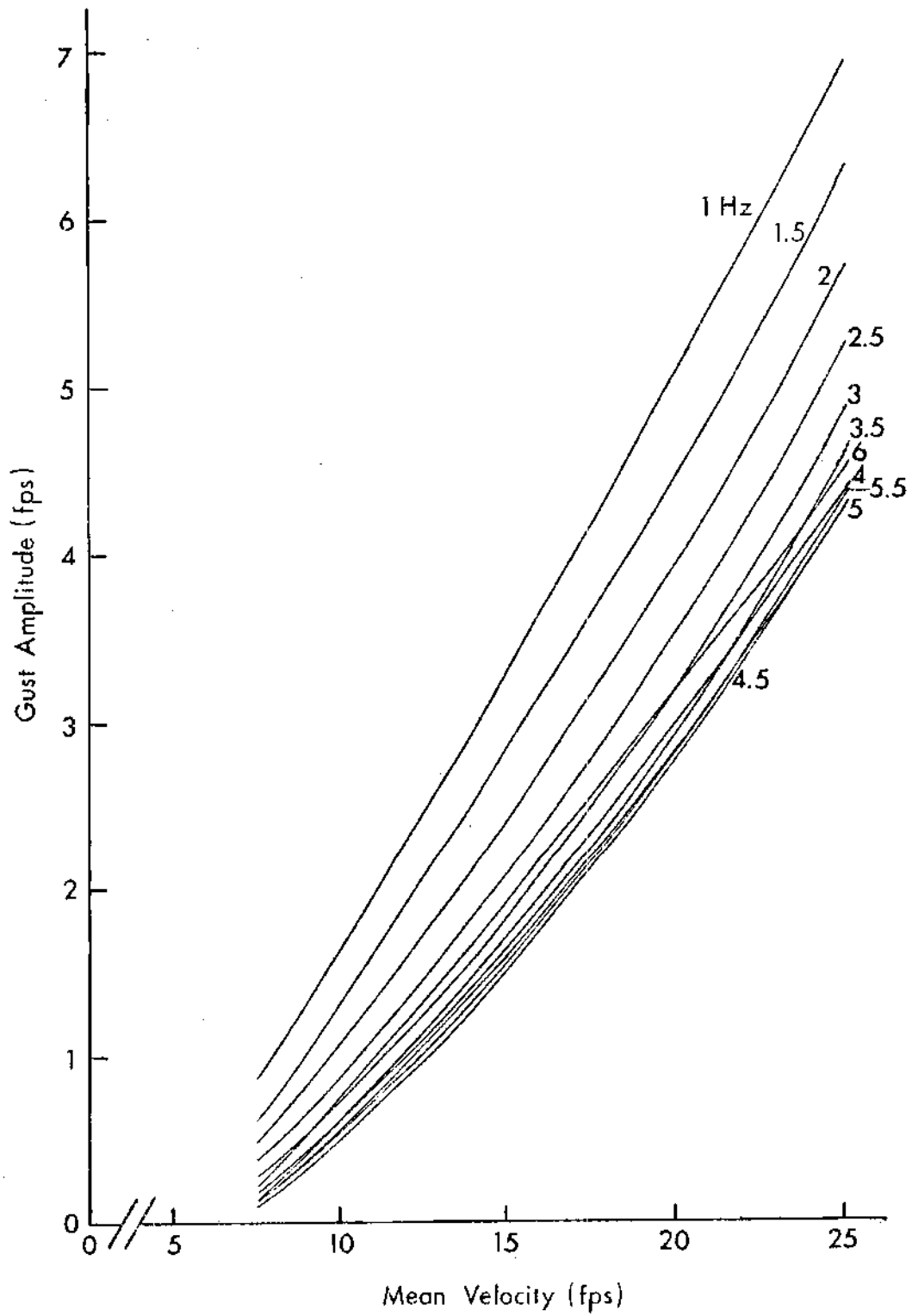


Figure 39. Operational Curves for the 70% Vanes (1-6 Hz)

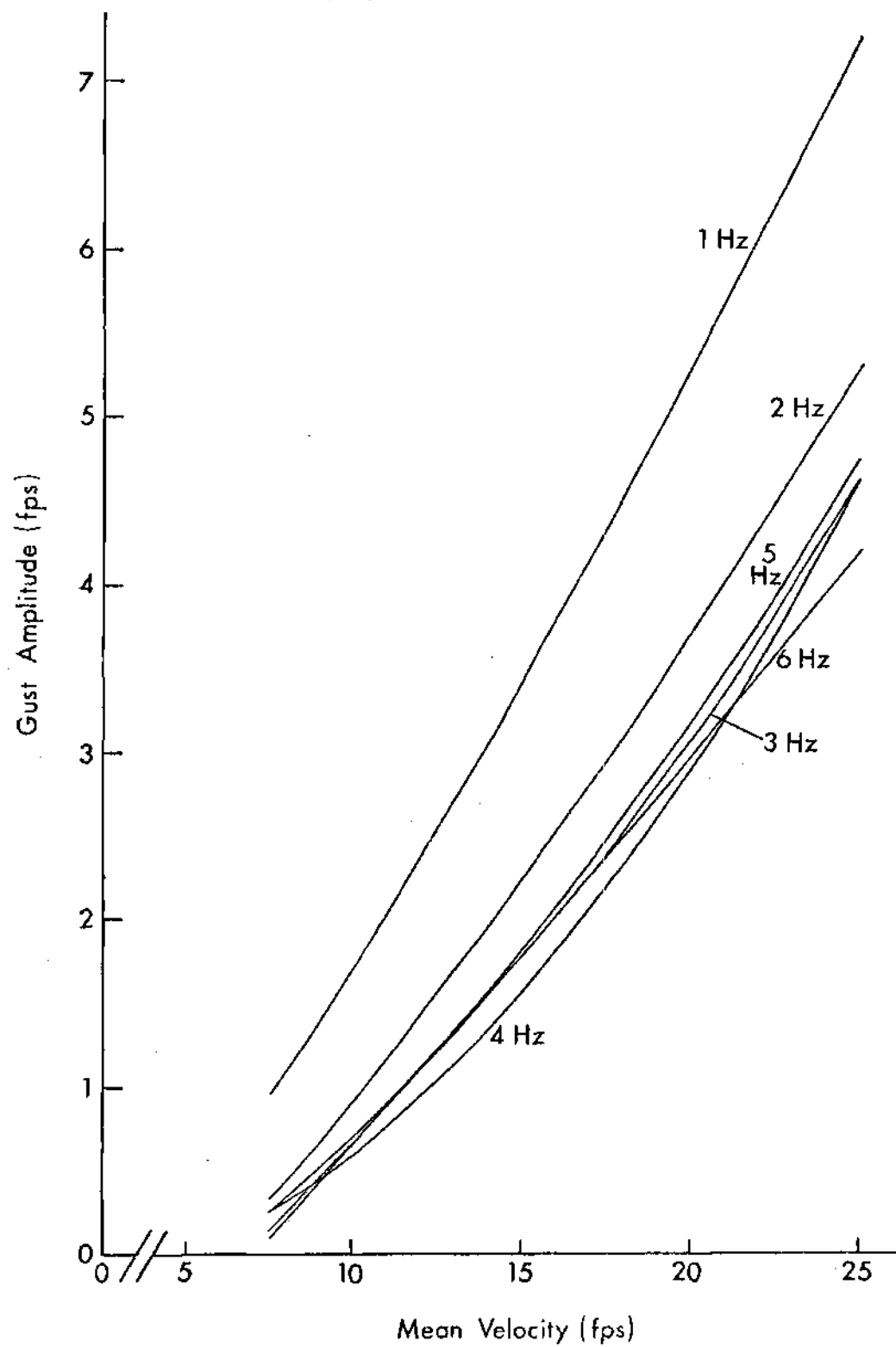


Figure 40. Raw Data Curves for the 70% Vanes (1-6 Hz)

CHAPTER IX

AIRFOIL MODEL AND SUSPENSION SYSTEM

To accomplish the objectives of the test program, the airfoil model and its suspension system had certain requirements that had to be satisfied. Most importantly, there had to be some means for measuring the lift and drag on the model. Also, the capability for changing the model angle of attack was needed. Finally, the natural frequency of the system had to be well above the operating frequencies of the freestream velocity perturbations.

Airfoil Model

Like the model described in Chapter III, this model had a 9 inch chord, a 42 inch span, and an NACA 0012 airfoil cross-section. It was, however, constructed from one piece of urethane foam that was split lengthwise, then bonded back together around the spar. It was then shaped to the NACA 0012 section. Due to the fact that the foam chipped easily along the trailing edge, the last inch of the chord was constructed from balsa wood. To complete its construction, the entire model was covered with a thin fabric, sealed, and painted.

In order to make the model as light as possible and still retain adequate lateral stiffness, a special spar was constructed. Starting with a one inch diameter aluminum rod, the part of the spar which was to be inside the model was shaped into an I-section. The total width of

the I-section was 0.625 inches and the height was 0.750 inches. Both flanges were 0.188 inches thick, while the web was 0.063 inches thick. Thus, the I-section had an $E_{Al}I$ of approximately 1.24×10^6 lb-in². The remainder of the spar was turned down to a 0.875 inch diameter. This was done so that the spar would fit through the existing holes in the wind tunnel walls.

Suspension System Assembly

To minimize the fabrication of new parts, the support for one end of the model was fastened to the trapezoidal frame used as a support for the oscillating model. The other support was fixed to the top of the original outer bearing support (Figure 6).

Unlike the oscillating model support system, this assembly (Figure 41) was identical on both sides of the wind tunnel. On each side it consisted of the force balance and the angle of attack adjustment disks.

Each force balance was attached to a base plate, which was in turn bolted to the supporting structure. The base plates served to orient the balances such that the model spar would line up with the holes in the wind tunnel wall.

Providing the means for adjusting the model angle of attack were the adjustment disks. The inner disk on each side was connected to the model spar, and the outer disk to the force balance. By loosening the four adjustment nuts on each disk, the model could be rotated to obtain the desired angle of attack.

The simplicity of this suspension system made it relatively easy to operate and service, as well as manufacture. In addition, it was considerably easier to set up and dismantle than was the previous system.

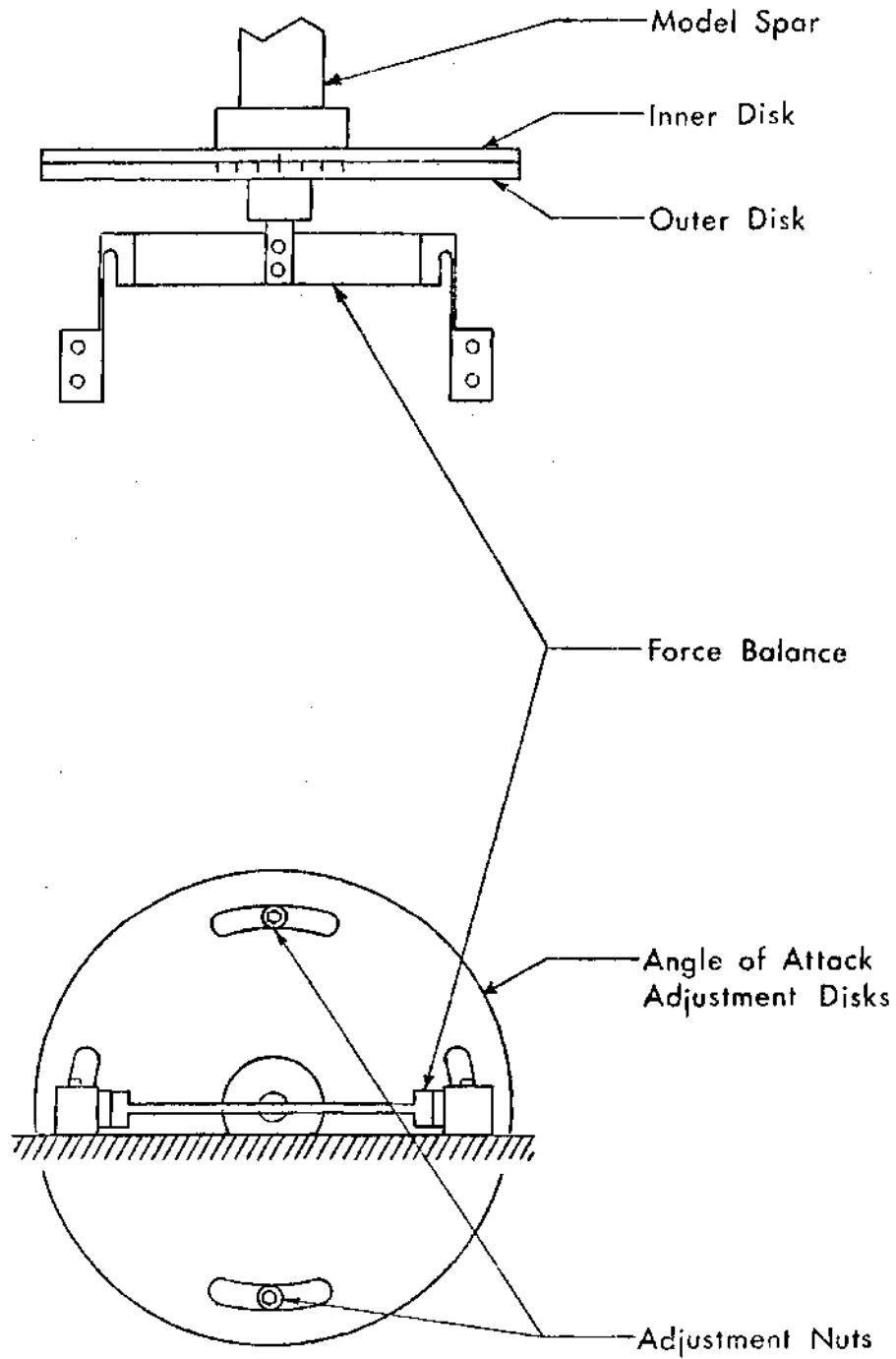


Figure 41. Stationary Model Suspension System

Force Balance

When the different means for measuring lift and drag were first being investigated, both force and pressure transducers were considered. While each system has its own advantages and disadvantages, the fact that pressure data can give only the lift was the deciding factor. In order to obtain the drag, a force measurement system had to be used. The one major obstacle that had to be overcome was how to get adequate sensitivity in the drag measurements, while having a sufficiently high natural frequency for the system.

Balance Design

In order to find a suitable design for the force balance, a literature search was undertaken to find out what configurations had been used, and with what success. The type of balance that was finally selected was similar to that used by Windson [7]. It combined the features of being able to measure lift and drag, and of being relatively easy to construct. Figure 42 shows the balance configuration, strain gage locations, and bridge circuits.

The use of this type of balance made it essential to find a way of getting a fairly large output voltage from the drag bridges, while maintaining a high natural frequency. Using ordinary foil strain gages, it was found that in order to get a reasonable output, the natural frequency of the entire system would have had to have been on the same order of magnitude as the system's operating frequency [7]. Thus, semiconductor strain gages were used on the drag beams, instead of the foil type which were used on the lift beams.

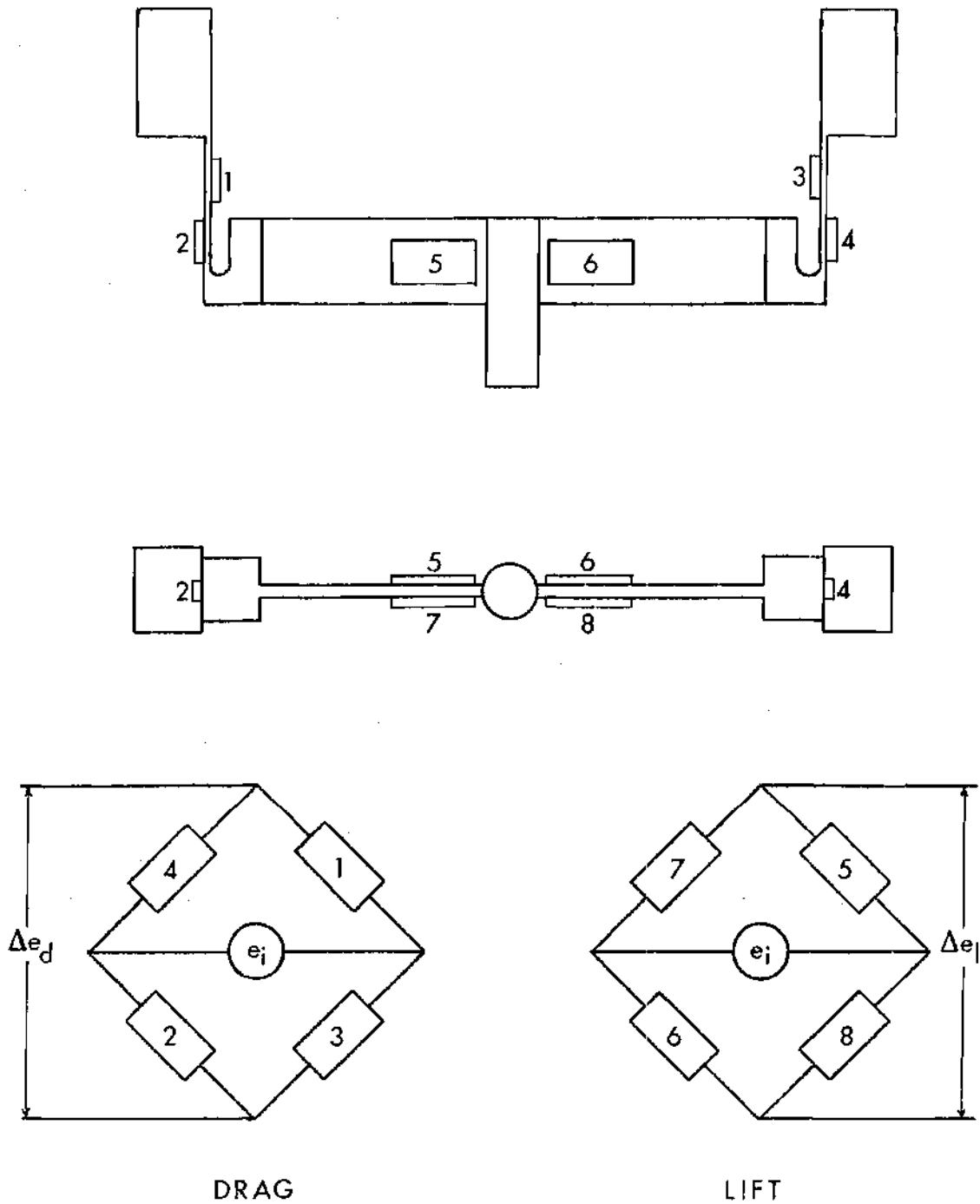


Figure 42. Force Balance Configuration and Strain Gage Bridge Circuits

Drag Beam

The elastic element used to measure drag force was an "S" bending beam [46]. To allow room for the bonding of gages, each beam was designed to be 0.750 inches long and 0.375 inches wide. That left only the beam thickness to be determined analytically.

Two factors entered into the specification of the thickness of the beam. One was the output of the bridge circuit, and the other was the natural frequency of the system as a whole. In previous work, a 5 microvolt, 60-cycle noise signal had been observed to be present in the bridge output at all times. Thus, it was necessary to assure that the bridge output would be large enough to obtain a satisfactory signal-to-noise ratio. Also, since the model was to be subjected to velocity variations at frequencies up to 6 Hertz, the natural frequency of the system, as supported by the drag beams, had to be as high as possible.

The procedure used to select a thickness for the drag beam was an iterative one. After picking a preliminary thickness, the output and frequency were calculated. This was repeated for successive values of thickness until a suitable value was found. The relations used for these calculations can be found in Appendix B, along with the results for the final set of dimensions.

Lift Beam

For the lift measurement, the elastic element was modeled as a beam pinned at both ends, with a torsional spring attached (see Appendix B). Like the drag beam, the lift beam length of 3.0 inches and width of 0.5 inches were selected so that the strain gages could be easily bonded to each beam. The thickness of this beam was also constrained by the

same factors as the drag beam. The procedure for selecting a suitable thickness was, therefore, identical to that for the drag beam, except for the equations used. These equations and the results for the final dimensions are also found in Appendix B.

Force Balance Calibration

The calibration of the force balances for the measurement of lift and drag was conducted outside the wind tunnel on a stand made specially for this purpose. On this stand, the model was mounted in the same manner as it would later be installed in the wind tunnel. However, the stand was constructed such that the entire assembly could be rotated ninety degrees.

Each strain gage bridge was driven by a 5 volt power supply, both for the calibration and for the testing to follow. The outputs of each bridge were amplified by Neff, Type 122, DC amplifiers. A gain of 50 was applied to each drag output signal, and a gain of 200 to each lift output. These output values were read directly from a Fluke digital voltmeter.

Lift Calibration

For the lift force calibration, the model and stand assembly were put in the horizontal position illustrated in Figure 43. With the weight pan and load arm assembly disconnected and with the loading collar removed, the amplified outputs of the lift strain gage bridges were zeroed. Then, the collar was attached along with the loading apparatus. Weights were then added to the weight pan until the outputs of the amplifiers were again zero. In this manner, the weight of the collar was cancelled out.

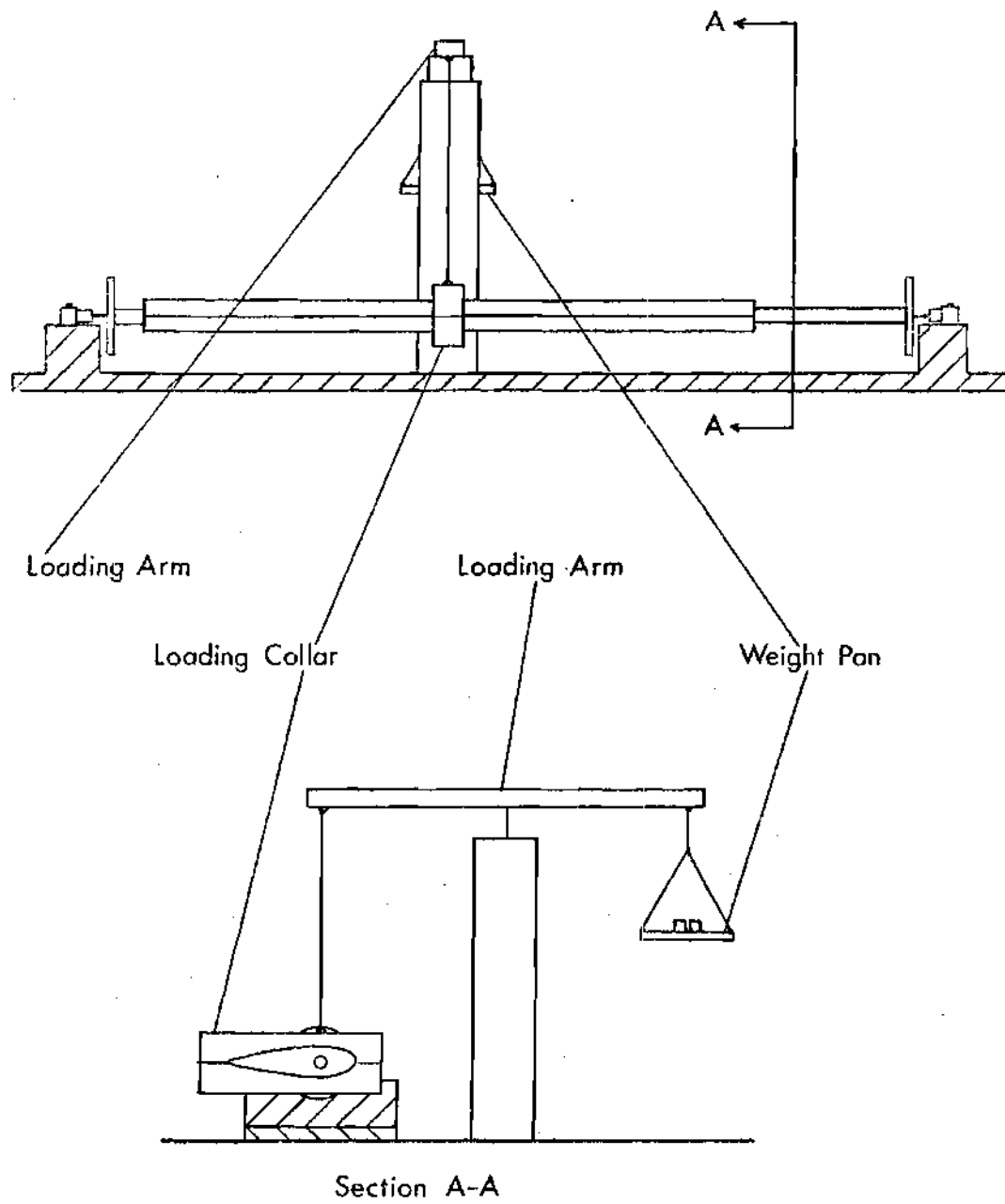


Figure 43. Lift Force Calibration Stand

The calibration itself simply involved adding to and subtracting from the weights in the pan, and recording the corresponding amplifier outputs. A linear least squares curve was fit to the calibration data for each balance. These curves are shown in Figure 44.

Note that, for the same load applied to the system, the output of the west force balance bridge is 1.39 times larger than the east output. This is a result of the model not being centered between the balances. Calculating the reactions at the supports for a unit load applied at the center of the airfoil model, the west reaction would be 1.34 times larger than the east reaction.

Drag Calibration

Since the drag loads that the model would experience were to be very small, the only practical methods of methods of calibration involved the direct use of weights. With the calibration stand in its horizontal position and the collar removed, all of the amplifier outputs were zeroed. The stand was put into the vertical position and weights were applied as shown in Figure 45, returning the outputs to zero. The horizontal force applied to the model represented the weight of the model while it was in the horizontal position. The vertical force alleviated the weight of the model and collar while the stand was in the vertical position. In addition, weights added to the vertical force weight pan represented drag.

The data in Figure 46 were obtained by adding weights to the vertical force weight pan. Using a least squares linear approximation, calibration curves were fit to the data (Figure 46). As for the lift calibration, the west bridge output was 1.39 times greater than the east output for the drag calibration. Again, this was due to the fact that

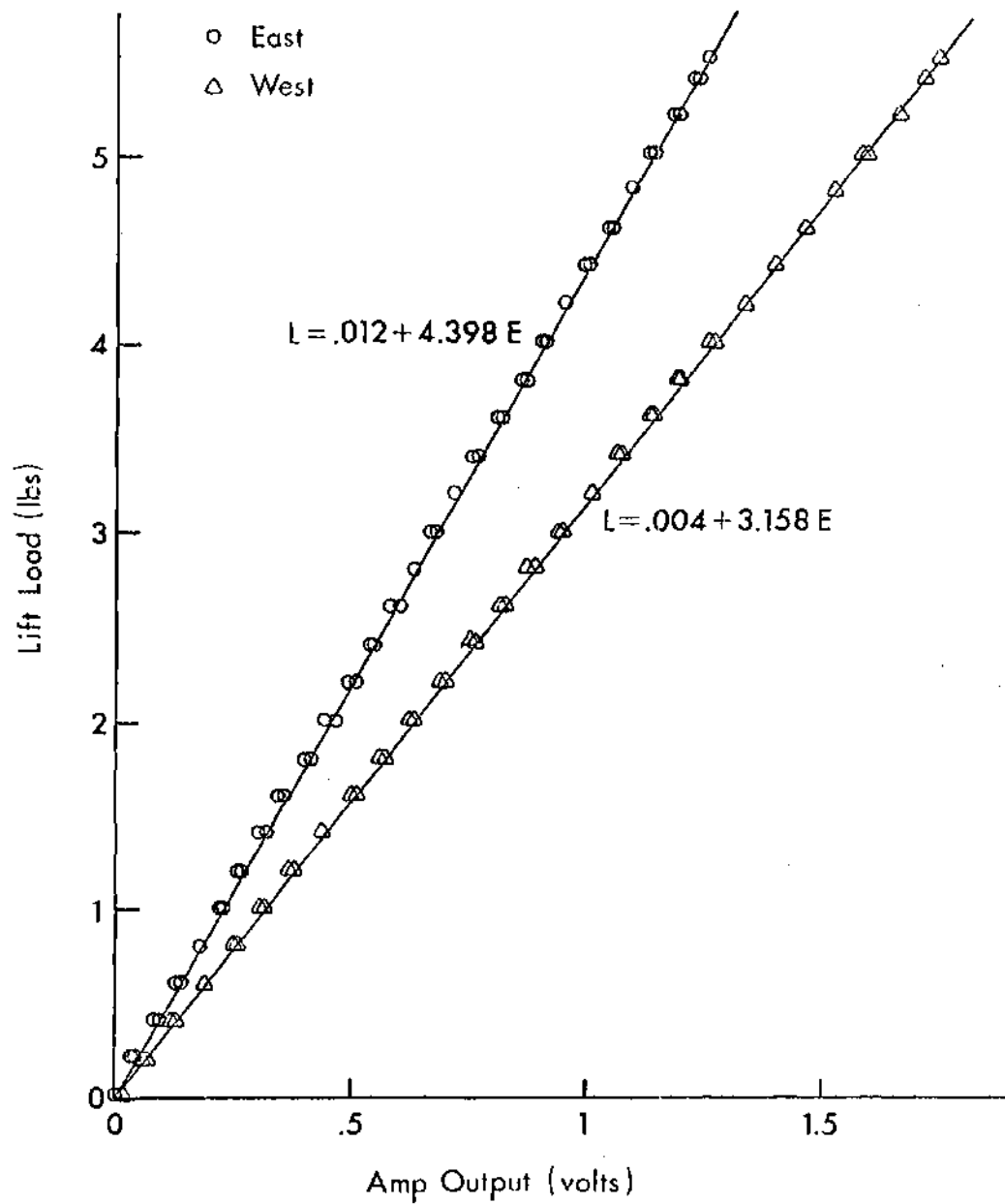


Figure 44. Lift Force Calibration Curves

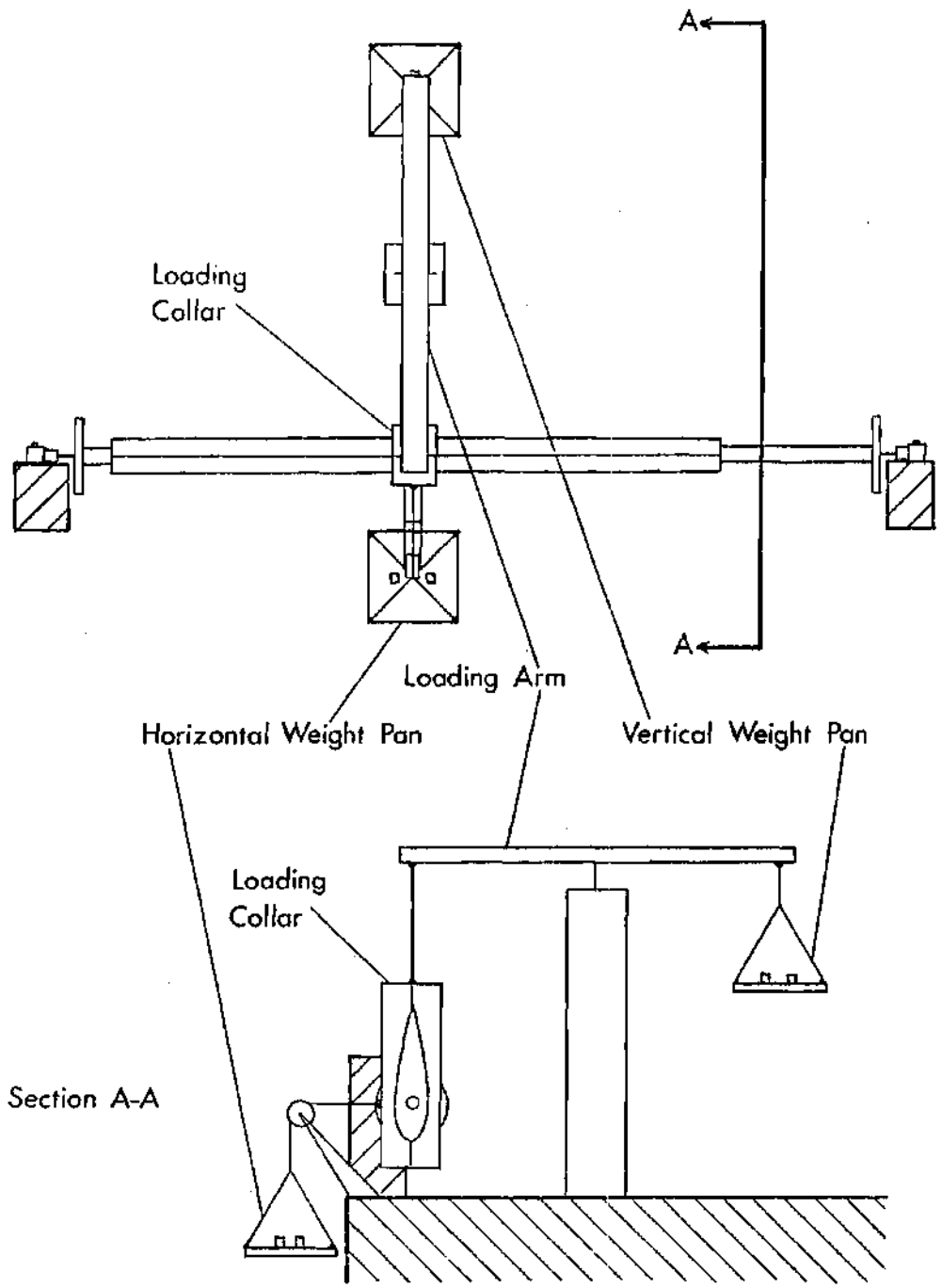


Figure 45. Drag Force Calibration Stand

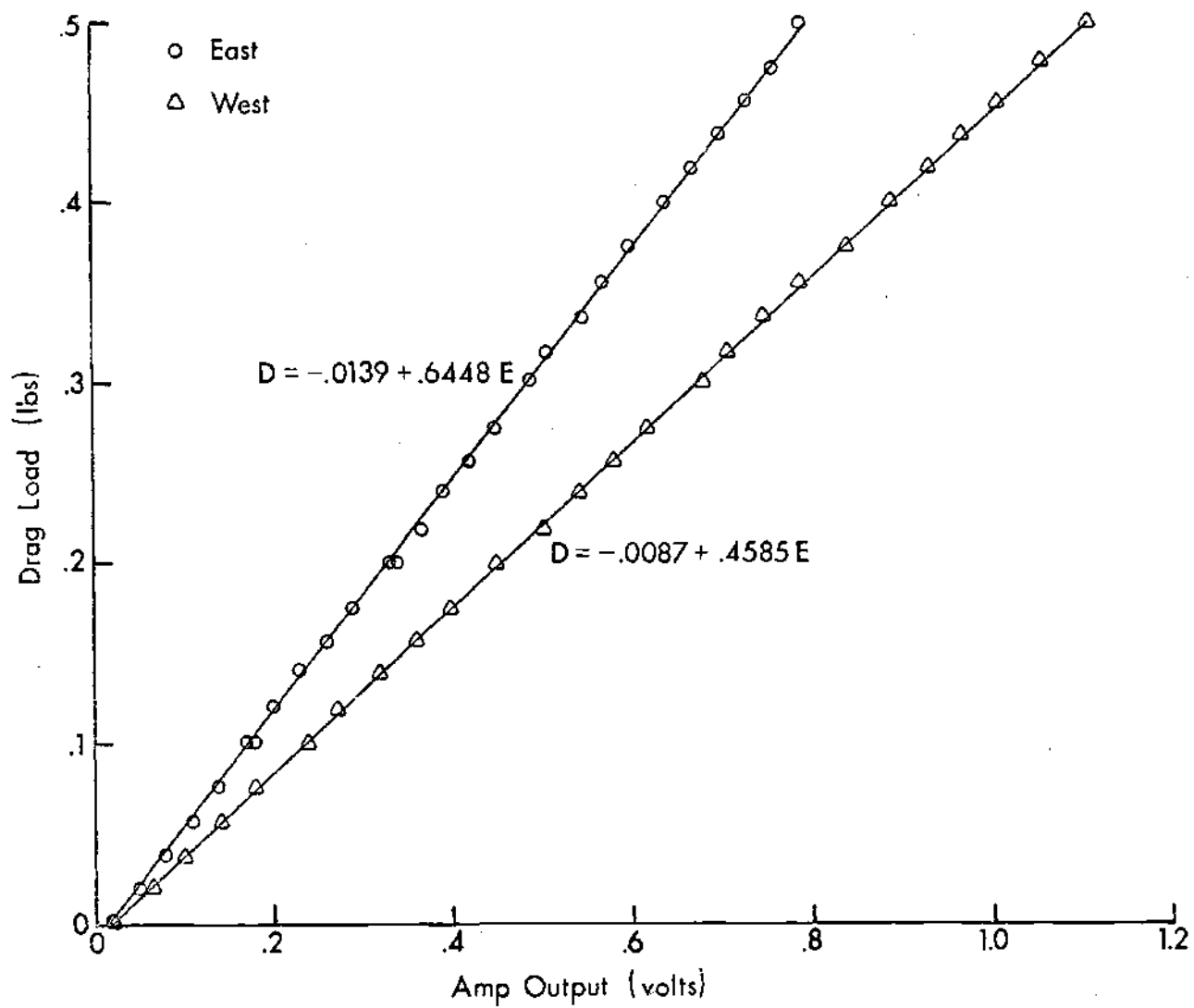


Figure 46. Drag Force Calibration Curves

the model was not centered between the supports.

Since semi-conductor strain gages are known to exhibit non-linear characteristics, and the calibration curves appear to be linear, additional loads beyond the anticipated load range were applied to check on the extent of the nonlinearity. As can be seen in Figure 47, the drag outputs follow the previously established calibration curves well beyond the anticipated load range. This is most likely due to the small strains put on the drag beams, plus the fact that in each bridge two gages are in tension while the other two are in compression, thus cancelling out any non-linear effect.

Lift-Drag Coupling

Using the same set-up as for the lift calibration, the effect of lift loads on drag outputs was investigated. In this case, all four amplifier outputs were zeroed with no loading collar. Then, as before, the collar and weight pan were installed and the lift outputs zeroed by adding weights to the pan. This should have, and did, also make the drag outputs zero.

The data in Figure 48 are the results from adding weight to the pan, recording all four amplifier outputs, and converting the voltages to lift and drag forces by the use of the calibration curves (Figures 44 and 46). Least-squares quadratic curves were fit to the data. From these curves, it can be seen that there is indeed a coupling between the lift and drag.

To gauge the significance that the coupling might have during the unsteady drag tests, the drag forces indicated by each force balance bridge were summed as they would be during the tests. The curve of

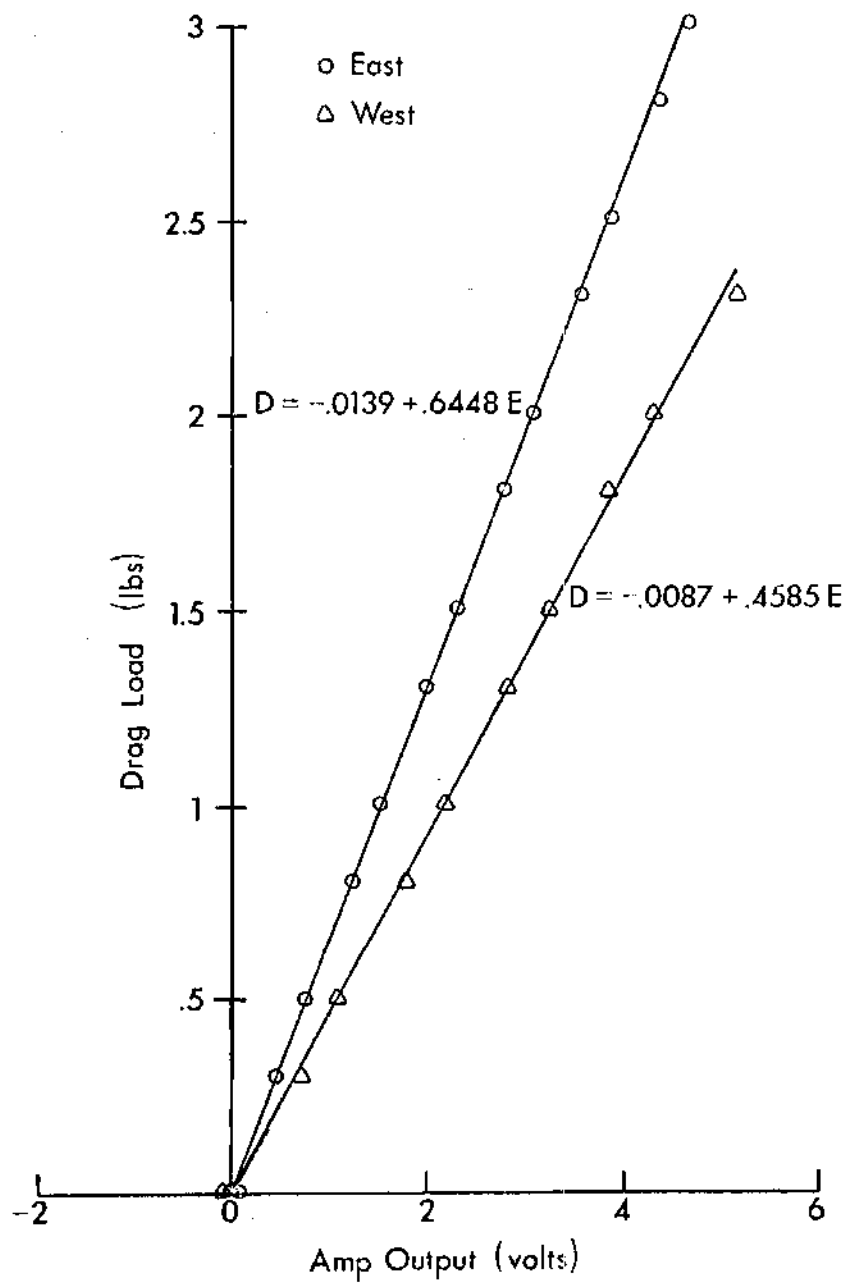


Figure 47. Extended Drag Force Calibration Curves

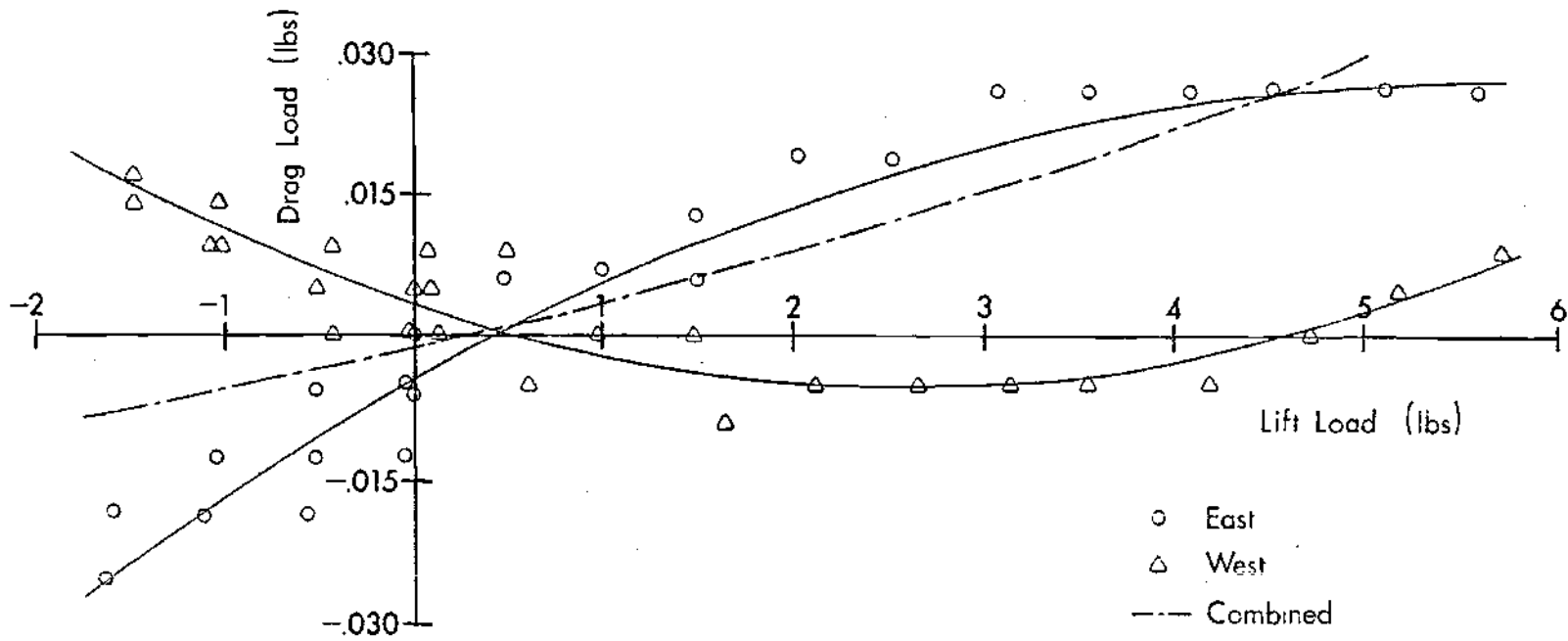


Figure 48. Lift-Drag Coupling Curves

combined drag versus lift is also shown in Figure 48.

Preliminary estimates of the magnitudes of the unsteady lift and drag forces indicated that they would be approximately 0.3 and 0.015 pounds, respectively, and that the coupling between the lift and drag outputs would add approximately 0.0015 pounds, or ten percent, to the drag readings (Figure 48). While this discrepancy might appear significant, it would likely not be particularly important because of other factors. In Appendix B, it was estimated that 60-cycle hum would be one percent of the total signal, and past experience with the gust generator has indicated that it could produce considerably more noise. Weighing these factors against the expected returns, and considering the complexities that could arise in making such a correction resulted in the coupling being neglected in the dynamic tests. It could not, however, be neglected in the steady-state measurements, both because the gust generator would not be in operation and because the coupling has a much greater influence on the magnitude of the drag.

A comment should also be made as to the reason for the opposite curvatures of the two coupling curves. A probable explanation is that when a lift load is imposed, there is a slight shortening of the distance between drag beams due to the curvature of the lift beam. This causes the drag beams to react like cantilever beams, and imposes a compressive strain on the root gages (1 and 3 in Figure 42) which is much larger than the tensile strain on the tip gages (2 and 4 in Figure 42). Since both balances are wired identically, but located on opposite sides of the wind tunnel, their polarities are opposite in sign in order to get positive drag in the downstream direction. Thus, this

type of loading, where both balances are loaded in the same way, results in outputs that are opposite in sign.

CHAPTER X

DATA ACQUISITION AND REDUCTION

This experimental program was designed to study unsteady drag at low angles of attack, and to determine its characteristics. To achieve this end, there were several necessary measurements to be made. These included the test-section velocity, the steady-state lift and drag, the unsteady drag, and the unsteady lift.

As in Part I, the data was recorded using a Tektronix Oscilloscope Camera C-12. However, for this data no automatic triggering was required, so both the camera shutter and oscilloscope sweep were tripped manually.

Velocity

For monitoring the freestream velocity during the steady-state force determinations, it was possible to read the hot-wire anemometer output directly from a digital voltmeter. However, the unsteady force measurements required a different approach. To completely describe the test section velocity with the gust generator in operation, the mean velocity (V_0), the gust amplitude (V_1), and the gust frequency (ω_v) had to be measured.

The mean velocity was determined by using the hot-wire voltage averaging circuit (Figure 18) described in Chapter IV. From the anemometer, the hot-wire voltage was fed to the analog computer, averaged, and the output read on the computer's digital voltmeter. The conversion to velocity was made using the calibration curve of Figure 36.

Taking the output directly from the anemometer and displaying only the perturbation voltages on one channel of the oscilloscope, the gust amplitudes and frequencies could be measured. This type of display also allowed the phase relationships between velocity and drag to be observed.

The conversion from perturbation voltages to velocities was accomplished by adding the maximum perturbation voltage to the mean, as acquired above, and subtracting the minimum. Using Figure 36, the maximum and minimum velocities were obtained, the difference taken, and halved. The result was the gust amplitude.

Finding the gust frequency involved measuring the length of the velocity cycles on the oscilloscope photographs, multiplying by the horizontal time scale, and inverting. The result was the gust frequency, in Hertz.

Static Lift and Drag

In obtaining the steady-state lift and drag, the same electronic equipment was employed as was used in the calibration of the force balances. Also, the two lift outputs and the two drag outputs were fed into the analog computer, where they were summed to give one lift and one drag signal.

The summed lift and drag voltages were read from a digital voltmeter and multiplied by the calibration constants for lift and drag (Figures 44 and 47). Then the drag force was corrected for coupling effects, as indicated in Figure 45.

To get the drag and lift coefficients, the forces obtained above were divided by the dynamic pressure according to the definitions

$$C_L = L / \frac{1}{2} \rho V^2 c s \quad (5)$$

$$C_D = D / \frac{1}{2} \rho V^2 c s \quad (6)$$

Unsteady Drag

Because of the noise induced in the drag signal by the operation of the wind tunnel and the gust generator, it was necessary to filter the drag outputs. A Spectral Dynamics SD101B Dynamic Analyzer, equipped with a 5 Hz bandwidth filter, was used. This tracking filter had the advantage of having a phase adjustment so as to preserve the proper phase relationships between drag and velocity. As illustrated in Figure 49, the filter was employed after the drag signals had been summed in the analog computer. The tuning input for these tests was provided by a Hewlett-Packard Model 202CR Low Frequency Oscillator.

The output of the tracking filter was connected to the second channel of the oscilloscope. Thus, the velocity perturbations and the unsteady drag could be viewed and photographed simultaneously.

Unsteady Lift

In recording the unsteady lift, the same procedures that were used to obtain the unsteady drag were again employed. Since there was only one tracking filter available, a function switch in the analog computer served to change the input to the filter from drag to lift (Figure 49).

Experimental Procedures

At each test condition for which data was to be recorded, the following quantities had to be set: angle of attack, mean freestream

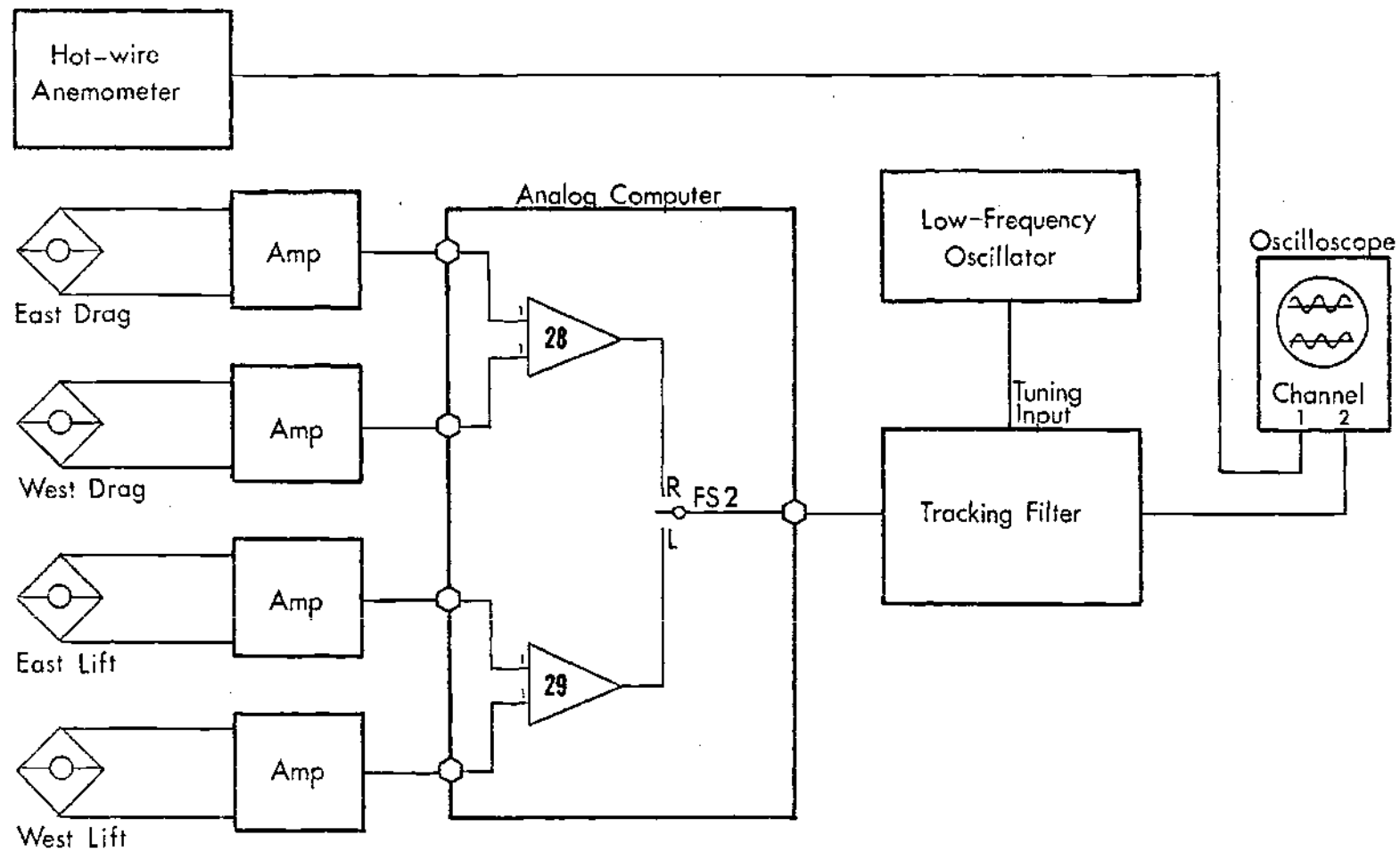


Figure 49. Electronics for the Unsteady Drag Measurements

velocity, gust frequency, and gust amplitude. In addition, each time the frequency was changed, the tuning input had to be adjusted along with the tracking filter phase shift. Thus, a procedure was developed to make the data collection as efficient as possible.

In order of increasing difficulty, the adjustments that had to be made were mean velocity, gust frequency, angle of attack, and vane size. The idea was, therefore, to make the more difficult changes the fewest possible number of times.

From the above considerations, a procedure evolved that was both efficient and workable. First, the desired set of vanes was installed in the gust generator and the angle of attack of the model set. Then, the tuning input to the tracking filter was set to the proper frequency. To assure that the filter induced no phase shift, the output of the low-frequency oscillator was connected to the filter input. Both the filtered output and the oscillator output were displayed on the oscilloscope, and the filter phase adjusted if necessary. After reconnecting the wires so that the unsteady drag output from the analog computer would be filtered and then displayed on the oscilloscope along with the velocity variations, the vanes were turned on and set to the desired frequency. Then, the wind tunnel was turned on and the mean velocity set, as indicated by the analog computer's digital voltmeter.

When this process was complete, a photograph of the drag and velocity outputs was taken with the oscilloscope camera. A second exposure was also taken on each picture with the inputs grounded, to locate the mean velocity and steady drag with respect to their variations.

The other data points were obtained by changing the mean velocity

until all points with the same frequency, angle of attack, and vane size had been photographed. Then, the frequency of the gusts was changed along with the tuning input, and the phase angle checked as before. When all of the frequencies associated with a particular angle of attack and vane size were completed, the angle of attack was changed. The vanes were only changed when all of the data points using that set were completed.

Aerodynamic Derivatives

The purpose of measuring the unsteady lift and drag in a flow field with streamwise, simple harmonic perturbations in the freestream velocity was to simulate the effects of a rotor blade undergoing in-plane oscillations in a uniform airstream. These velocity perturbations must first, therefore, be related to an "equivalent oscillatory displacement" of the blade in the streamwise direction.

The freestream velocity in the test-section can be written as

$$V = V_0 + V_1 e^{i\omega t} \quad (7)$$

The equivalent displacement (ξ), of course, has the same frequency and is positive in the direction of the advancing blade. It is written as

$$\xi = \bar{\xi} e^{i\omega t} \quad (8)$$

or, in non-dimensional form, as

$$x = \xi/b = \bar{x} e^{i\omega t} \quad (9)$$

The velocity perturbations and the in-plane displacement are related through the rate of displacement ($\dot{\xi}$), which is

$$\dot{\xi} = i\omega_v b \bar{x} e^{i\omega_v t} = V_1 e^{i\omega_v t} \quad (10)$$

Therefore, the amplitude of the velocity perturbations in terms of the displacement becomes

$$V_1 = i\omega_v b \bar{x} \quad (11)$$

Having established a relationship between the velocity perturbations and the equivalent displacement, it will now be assumed that both the unsteady lift and drag can be expressed as linear functions of that displacement. This assumption will later be verified on the basis of the data to be recorded. Under this assumption, the unsteady aerodynamic loads can be represented as

$$C_l = \bar{C}_l e^{i\omega_v t} = \frac{\partial C_l}{\partial x} \bar{x} e^{i\omega_v t} \quad (12)$$

$$C_d = \bar{C}_d e^{i\omega_v t} = \frac{\partial C_d}{\partial x} \bar{x} e^{i\omega_v t} \quad (13)$$

Both the lift and drag derivatives will, in general, be complex numbers which represent their phase relationship with respect to the equivalent displacement. They are defined as

$$\bar{C}_l = \left[\left(\frac{\partial C_l}{\partial x} \right)_R + i \left(\frac{\partial C_l}{\partial x} \right)_I \right] \bar{x} \quad (14)$$

$$\bar{c}_d = \left[\left(\frac{\partial c_d}{\partial x} \right)_R + i \left(\frac{\partial c_d}{\partial x} \right)_I \right] \bar{x} \quad (15)$$

From Equation (11), which shows the velocity perturbations leading the equivalent displacement by 90° , the imaginary parts of the aerodynamic derivatives will be in phase with the velocity. Similarly, the real parts will lag the velocity perturbations by 90° .

Consider, for example, the unsteady drag as

$$d = \bar{d} e^{i\omega_v t} = (d_R + i d_I) e^{i\omega_v t} \quad (16)$$

where d_R is the harmonic component of the drag force which lags the velocity perturbations by 90° , and d_I is the component which is in phase with the perturbations. The unsteady drag coefficient (c_d) is then

$$c_d = \bar{c}_d e^{i\omega_v t} = \left[(d_R + i d_I) / \frac{1}{2} \rho V_o^2 cs \right] e^{i\omega_v t} \quad (17)$$

$$\bar{c}_d = (c_d)_R + i (c_d)_I \quad (18)$$

The associated components of the complex drag derivatives can then be found, via Equations (15) and (11), to be

$$\left(\frac{\partial c_d}{\partial x} \right)_R = (c_d)_R / \bar{x} \quad (19)$$

$$\left(\frac{\partial c_d}{\partial x} \right)_I = (c_d)_I / \bar{x} \quad (20)$$

Lift and Drag Data Reduction

Figure 50 is an example of the unsteady drag and the velocity perturbations as they appear in the oscilloscope photographs. The data on pictures such as this one were reduced and tabulated to obtain the lift and drag derivatives. Since each photograph could represent only one set of test conditions, only the real and imaginary parts of the lift or drag derivative for those conditions could be obtained from each photograph.

The real and imaginary parts of the drag derivatives were computed from

$$\left(\frac{\partial C_d}{\partial x}\right)_R = d_R / \frac{1}{2} \rho V_o^2 \text{ cs } \bar{x} \quad (21)$$

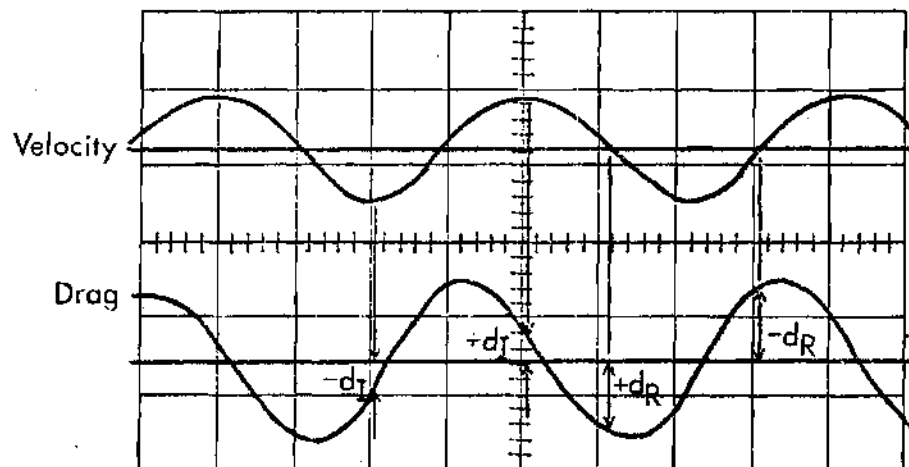
$$\left(\frac{\partial C_d}{\partial x}\right)_I = d_I / \frac{1}{2} \rho V_o^2 \text{ cs } \bar{x} \quad (22)$$

As demonstrated in the preceding section and shown in Figure 50, the imaginary component of the unsteady drag is in phase with the velocity perturbations, while the real component lags the perturbations by 90° .

The same phase relationships that apply to the real and imaginary parts of the unsteady drag also apply to the real and imaginary parts of the unsteady lift. The equations used to compute the lift derivative are also similar to those for the drag derivative. They are

$$\left(\frac{\partial C_l}{\partial x}\right)_R = l_R / \frac{1}{2} \rho V_o^2 \text{ cs } \bar{x} \quad (23)$$

$$\left(\frac{\partial C_l}{\partial x}\right)_I = l_I / \frac{1}{2} \rho V_o^2 \text{ cs } \bar{x} \quad (24)$$



$$d_R = \left[\sum_1^2 (+d_R) + \sum_1^2 (-d_R) \right] / 4$$

$$d_I = \left[\sum_1^3 (+d_I) + \sum_1^3 (-d_I) \right] / 5$$

Figure 50. Example of Unsteady Drag Data

CHAPTER XI

RESULTS AND DISCUSSION

Having obtained the unsteady lift and drag data by the methods of Chapter X, and having reduced it to lift and drag derivatives, it was necessary to examine the results. In addition to looking for trends due to reduced frequency and angle of attack, the test results were compared to quasi-steady and potential flow approximations.

The test conditions that the data represent are listed in Table 6 and 7. These tables became useful during the analysis of the data, when dependencies other than reduced frequency and angle of attack were being investigated.

Static Lift Data

The experimental lift curve obtained for these tests, at a Reynolds number of 1.43×10^5 , is shown in Figure 51. In order to verify this curve, steps were taken to compare the lift curve slope, shape, and stall angle to both theoretical and experimental results.

Since one of the suppositions of this investigation was that the flow was a two-dimensional, potential flow, the obvious comparison of the lift curve slope was to the potential flow value of 2π (for a flat plate). As can be seen from Figure 51, the test results exhibited a slope that was somewhat greater than predicted. In Chapter 16 of reference [46], Karamcheti gives an approximate correction factor for thickness effects.

Table 6. Unsteady Drag Test Conditions

α (deg)	k_v	V_o (fps)	Vane Size (%)	ω_v (hz)	V_1/V_o
4	.20	32.1	50	2.7	.05
4	.21	29.2	50	2.6	.04
4	.21	35.0	50	3.1	.05
4	.28	25.0	60	3.0	.07
4	.29	25.0	50	3.1	.04
4	.29	33.3	50	4.1	.06
4	.31	37.5	50	4.9	.06
4	.36	20.0	50	3.1	.03
4	.36	26.7	50	4.1	.04
4	.36	26.7	60	4.1	.08
4	.37	20.0	60	3.1	.06
4	.37	30.0	50	4.8	.06
4	.47	15.0	50	3.0	.03
4	.49	15.0	60	3.1	.05
4	.49	22.5	60	4.7	.07
4	.50	22.5	50	4.8	.04
4	.58	12.5	60	3.1	.04
4	.59	12.5	50	3.1	.02
4	.74	20.0	70	6.3	.12
4	.96	11.3	70	4.6	.08
0	.36	20.0	60	3.1	.06
0	.36	26.7	60	4.0	.07
0	.36	30.0	50	4.6	.05
0	.37	20.0	50	3.1	.03
0	.57	12.5	70	3.0	.07
0	.58	18.8	50	4.7	.03
2	.35	20.0	70	2.9	.11
2	.36	20.0	50	3.1	.03
2	.36	26.7	50	4.1	.04
2	.36	30.0	50	4.6	.06
2	.58	18.8	50	4.6	.03
2	.59	12.5	70	3.1	.07
6	.36	20.0	50	3.1	.04
6	.36	20.0	60	3.1	.06
6	.36	26.7	50	4.1	.04
6	.36	30.0	50	4.6	.06
6	.58	12.5	50	3.1	.02
6	.58	12.5	70	3.1	.07

Table 7. Unsteady Lift Test Conditions

α (deg)	k_v	V_o (fps)	Vane Size (%)	ω_v (Hz)	V_1/V_o
4	.23	32.1	50	3.1	.05
4	.29	25.0	50	3.1	.03
4	.30	37.5	50	4.7	.06
4	.37	26.7	50	4.2	.04
4	.37	30.0	50	4.7	.06
4	.47	15.0	50	3.0	.02
4	.59	18.8	50	4.7	.03
4	.72	15.0	50	4.6	.02
4	.72	15.0	70	4.6	.09
4	.98	11.3	70	4.7	.07
0	.36	26.7	50	4.1	.04
0	.37	30.0	50	4.7	.05
2	.35	30.0	50	4.5	.05
2	.37	26.7	50	4.2	.04
6	.36	26.7	50	4.1	.04
6	.36	26.7	50	4.6	.05

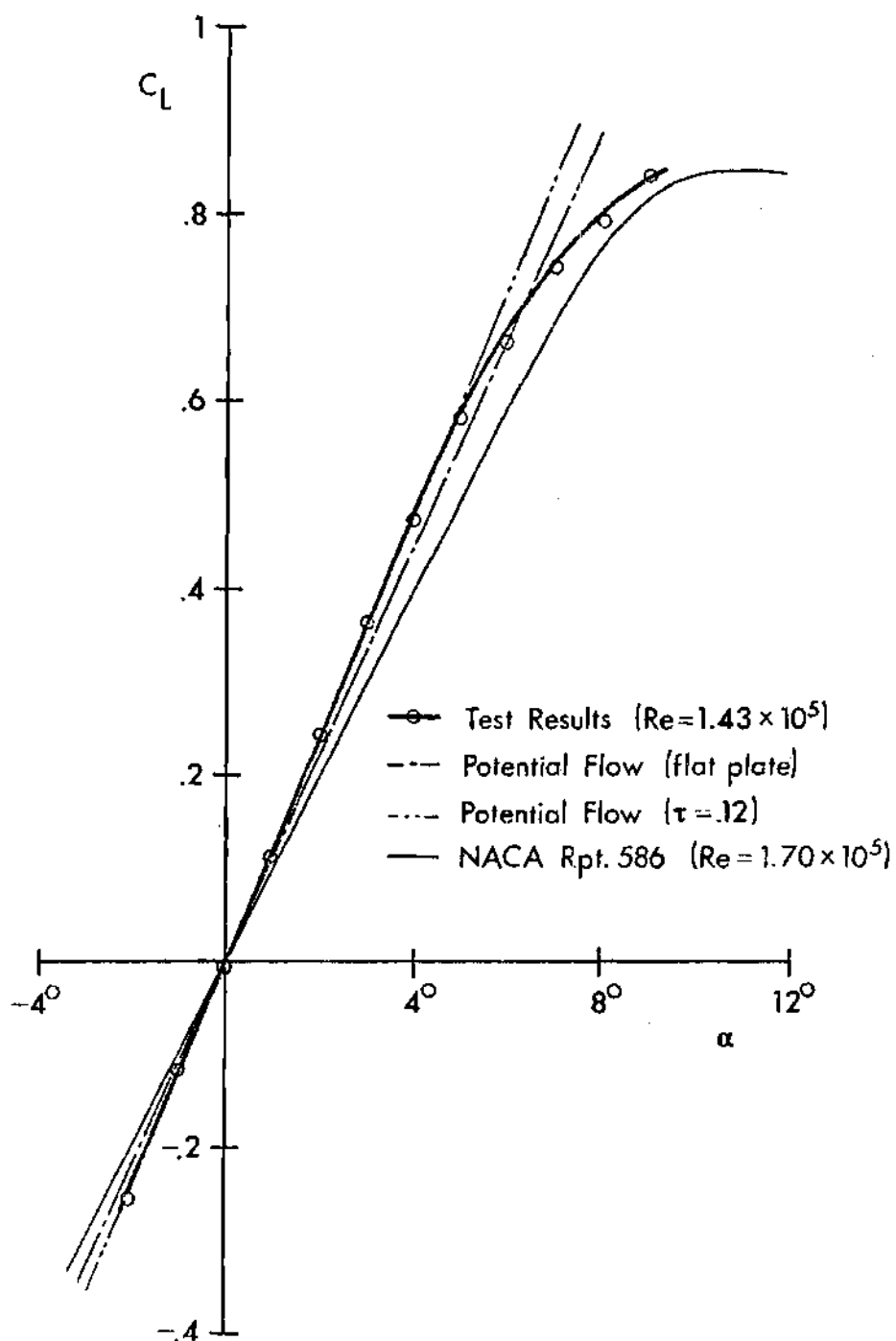


Figure 51. Static Lift Curves

$$\frac{\partial C_L}{\partial \alpha} = 2\pi (1 + .77 \tau) \quad (25)$$

Figure 51 shows that this correction brings the experimental and theoretical lift curves right into line. The close correlation of the two slopes not only confirmed the accuracy of the test results, but also indicated that three-dimensional effects played little or no part in the flow.

The next feature of the experimental lift curve to be investigated was the stall angle. Test data for this model were not taken beyond an angle of 9° because the turbulence generated by stall separation caused the model to vibrate. This was how the stall angle was determined. Since this angle appeared to be quite low, other data also obtained at a low Reynolds number were desired for the purposes of comparison.

In an NACA report by Jacobs and Sherman [47], it was found that the low stall angle was an effect of Reynolds number (Figure 51). In addition, the lift curve in the report showed a change in lift curve just above 4° , but to a lesser extent than the experimental curve obtained here. One explanation for the exaggeration of this deviation could be some roughness that was presented on the upper surface of the model, in the area of 0.8 c.

Static Drag Data

Figure 52 shows both current results and data from Jacobs and Sherman [47]. While the profile drag coefficients at 0° were nearly identical, the test results exhibited more curvature than the NACA results. Again, it is possible that the model's upper surface roughness was the major contributing factor. Because of the sensitivity required for these

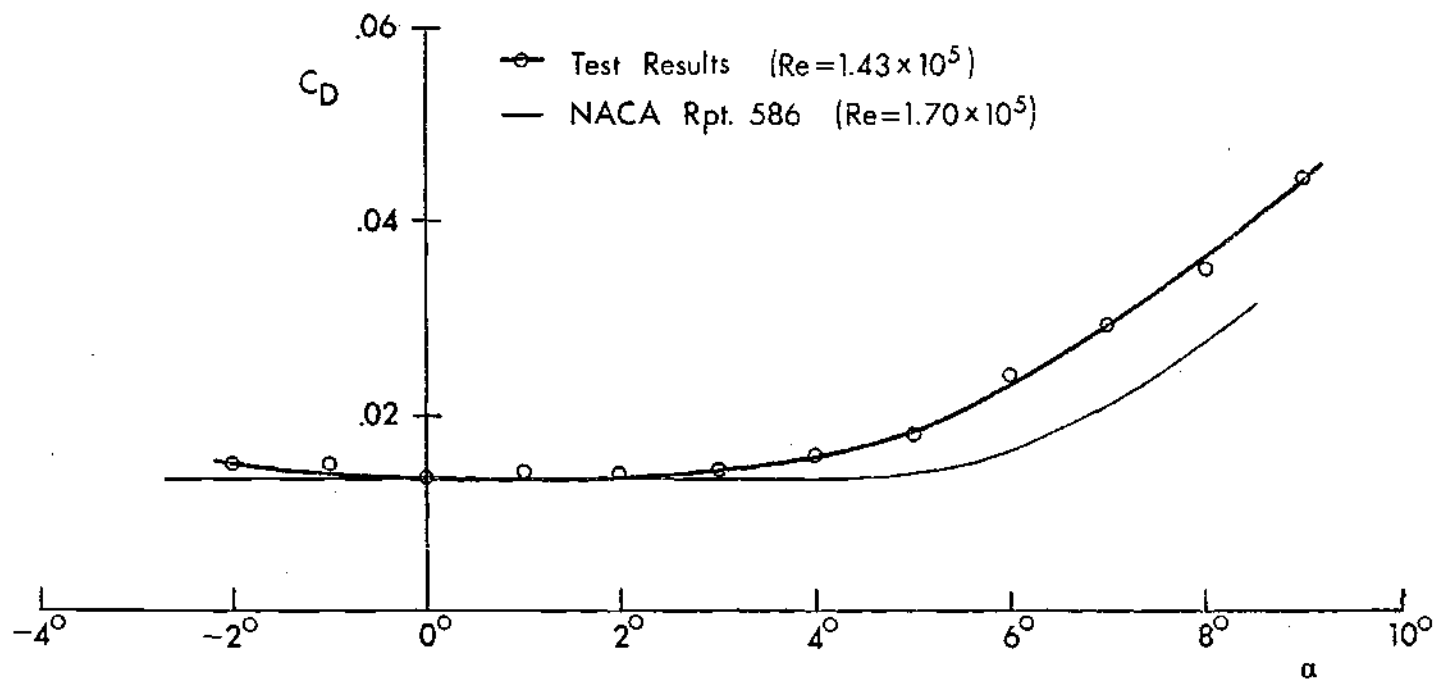


Figure 52. Static Drag Curves

measurements, the closeness of the two curves was encouraging, as it lent credibility to the accuracy of the drag measurements.

Unsteady Drag Derivative

The variations of the real and imaginary parts of the drag derivative with respect to reduced frequency, at an angle of attack of 4° , are shown in Figures 53 and 54. Both graphs exhibit good consistency, in that a definite, continuous trend is present in each. However, the data for the imaginary part are considerably more scattered than that for the real part. In addition, it should be noted that while the data in both figures appear to show larger deviations at the higher reduced frequencies, the percent deviation does not change appreciably.

A probable explanation for the greater scatter in the imaginary part can be illustrated by Figure 50. The real part of the drag was a larger number, located near the point of maximum velocity. The imaginary part was smaller, and found near the axis. Since both parts were subject to the same accuracy limitations at a particular reduced frequency, the imaginary part showed a greater percent deviation.

With respect to reduced frequency, both the real and imaginary parts of the drag derivative exhibited a tendency to increase in magnitude as the reduced frequency increased. The real part became more negative, while the imaginary part became more positive.

Figures 55 and 56 illustrate the effect of angle of attack on the drag derivative. Both of these plots show that, compared to the effect of reduced frequency, the angle of attack has only a weak influence. Again, it should be noted that while the data for $k_v = 0.58$ appear to be less consistent than the data for $k_v = 0.36$, there is little percentage

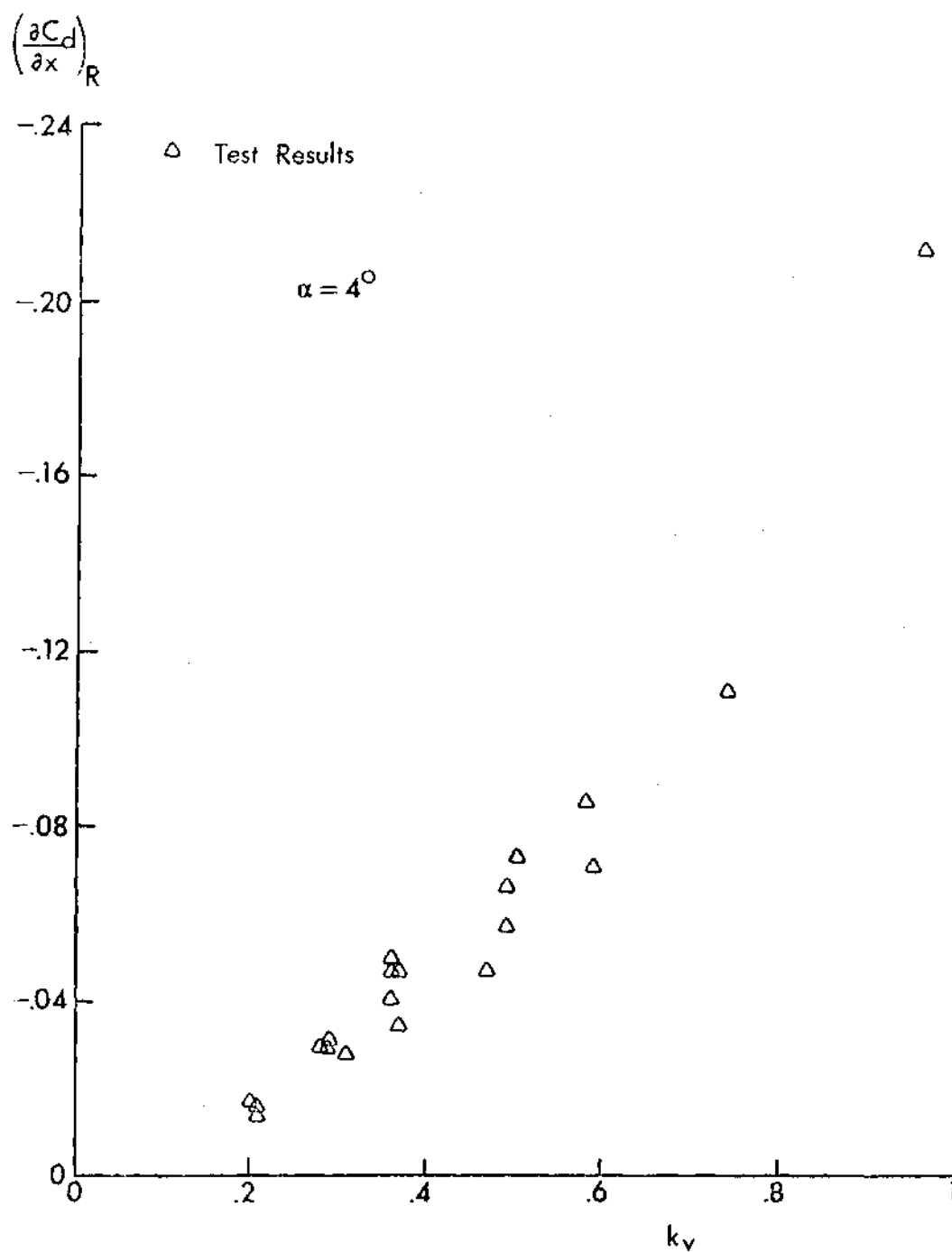


Figure 53. Drag Derivative Variations with Reduced Frequency (Real Part)

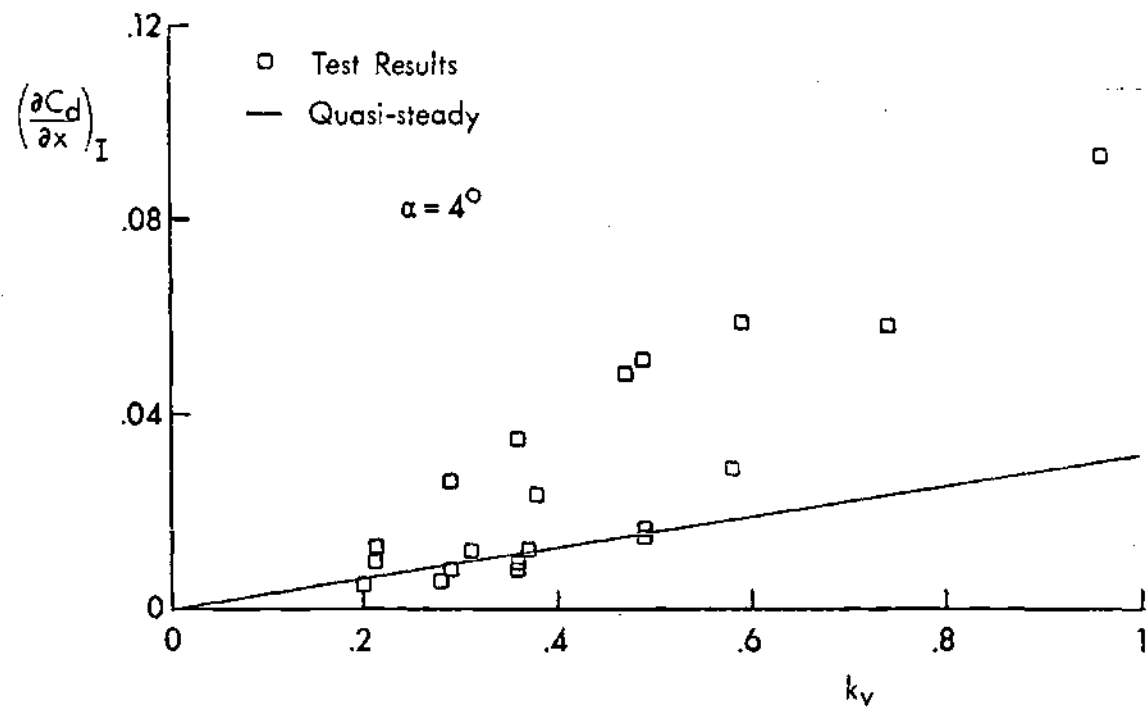


Figure 54. Drag Derivative Variations with Reduced Frequency (Imaginary Part)

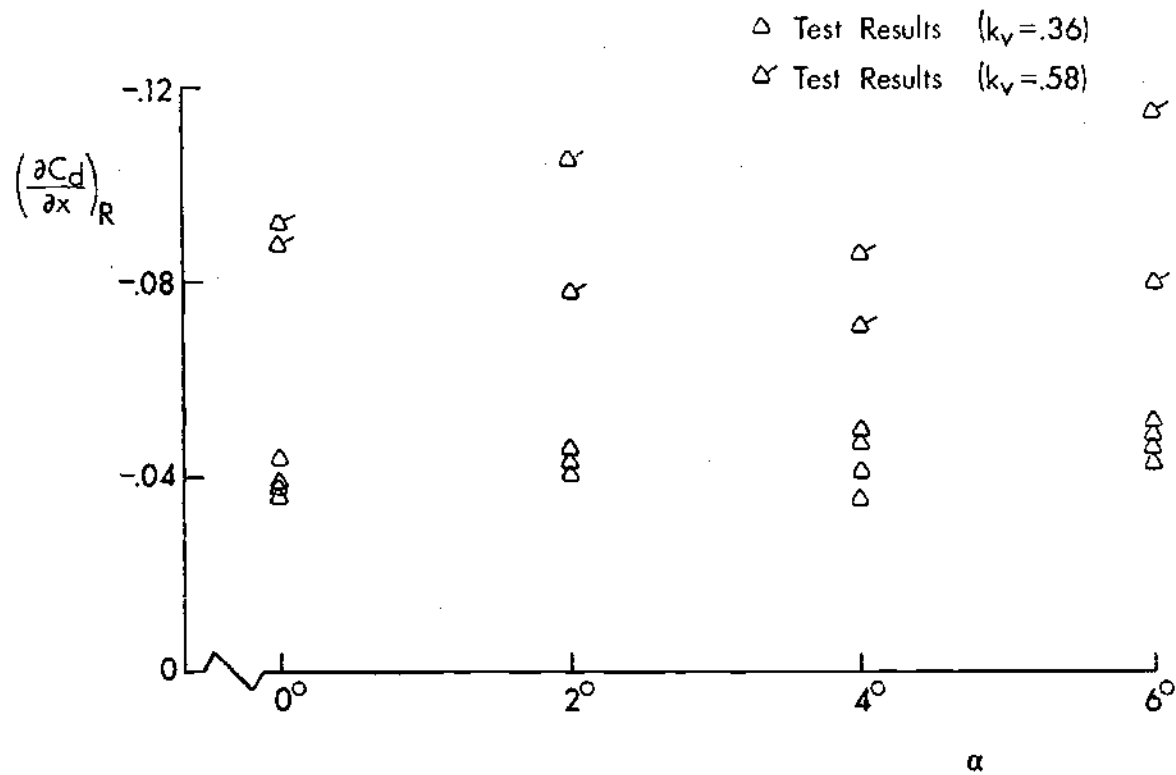


Figure 55. Drag Derivative Variations with Angle of Attack (Real Part)

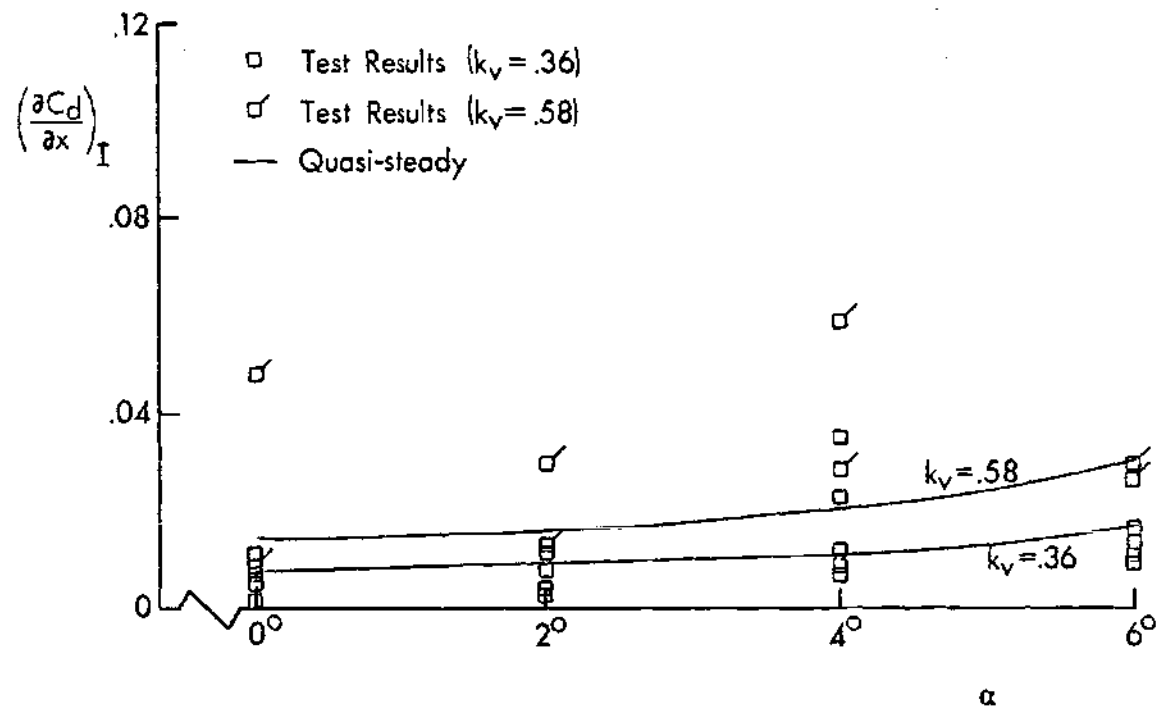


Figure 56. Drag Derivative Variations with Angle of Attack (Imaginary Part)

difference. It would have been considerably more difficult, however, to draw any conclusions based solely on the higher reduced frequency data.

Quasi-Steady Drag Approximation

As noted in Chapter VII, most analyses of in-plane blade oscillations use a drag coefficient equal to the two-dimensional, profile drag coefficient. This approach yields a drag derivative whose real and imaginary parts are zero at all angles and reduced frequencies. Judging from the data in Figure 53 through 56, this approximation does not appear to be valid.

It is proposed that a quasi-steady drag approximation be used, which is based on two-dimensional, steady-flow data. The unsteady drag can then be represented as

$$c_d = \bar{c}_D e^{i\omega t} \quad (26)$$

$$\bar{c}_D = \left[\frac{1}{2} \rho (v_0 + v_1)^2 c_D - \frac{1}{2} \rho v_0^2 c_D \right] / \frac{1}{2} \rho v_0^2 c_D \quad (27)$$

$$\bar{c}_D = c_D \left[2 \left(\frac{v_1}{v_0} \right) + \left(\frac{v_1}{v_0} \right)^2 \right] \quad (28)$$

Since the maximum experimental value of (v_1/v_0) was 0.12, the squared term can be neglected with respect to the linear term.

$$\bar{c}_D = 2 c_D v_1/v_0 \quad (29)$$

Substituting from Equation (10) to get Equation (29) in terms of

k_v and \bar{x} ,

$$\bar{c}_D = i 2 C_D k_v \bar{x} \quad (30)$$

$$c_d = i 2 C_D k_v \bar{x} e^{i\omega t} \quad (31)$$

From the definitions of the real and imaginary parts of the drag derivative, Equations (19) and (20),

$$\left(\frac{\partial c_d}{\partial x}\right)_R = 0 \quad (32)$$

$$\left(\frac{\partial c_d}{\partial x}\right)_I = 2 C_D k_v \quad (33)$$

Note that the real part of the derivative is zero. This is because the drag approximation is completely in phase with velocity.

The results of this approximation are plotted on Figures 54 and 56 to see how they compare with the test data. Since the real part of this derivative is always zero, its curve lies along the horizontal axes of Figures 53 and 55. Obviously, this is not a good approximation to the real part. In Figure 54, the steady-flow approximation lies along the lower boundary of the swath of data points. While it is difficult to ascertain a true slope for the points, the approximation does appear to predict somewhat smaller values.

At a reduced frequency of 0.36, in Figure 56, the approximation seems to do an excellent job. However, the curve for $k_v = 0.58$ falls below the data points. Judging from Figure 53, it is just possible that the close agreement at $k_v = 0.36$ is due to good fortune in picking the

reduced frequency. However, it is also possible that the true slope of the data in Figure 54 could be closer to the quasi-steady approximation than it appears. In that case, this approximation is indeed good, but for the imaginary part only.

Unsteady Lift Derivative

The lift derivative data are shown in Figures 57 and 58. In both plots, the data exhibit good consistency, and less scatter than the drag measurements. Most likely, this is a result of the lift forces being considerably larger and easier to measure.

In both figures, it is noted that, like the drag derivatives, the real and imaginary parts are of opposite sign. However, in this case, the real part is negative and the imaginary part positive. This change of sign is indicative of the phase difference between drag and lift that was observed in the raw data. It was found that the drag lagged the lift by an average of about 35° .

Figure 57 indicates that the imaginary part of the derivative does not change greatly with reduced frequency, although it does increase a little. The real part, on the other hand, shows a marked decrease above a reduced frequency of one-half.

The data showing the variation of lift derivative with angle of attack (Figure 58) demonstrates a definite increase in the imaginary part with angle of attack. The real part also appears to increase with angle of attack, but only very slightly.

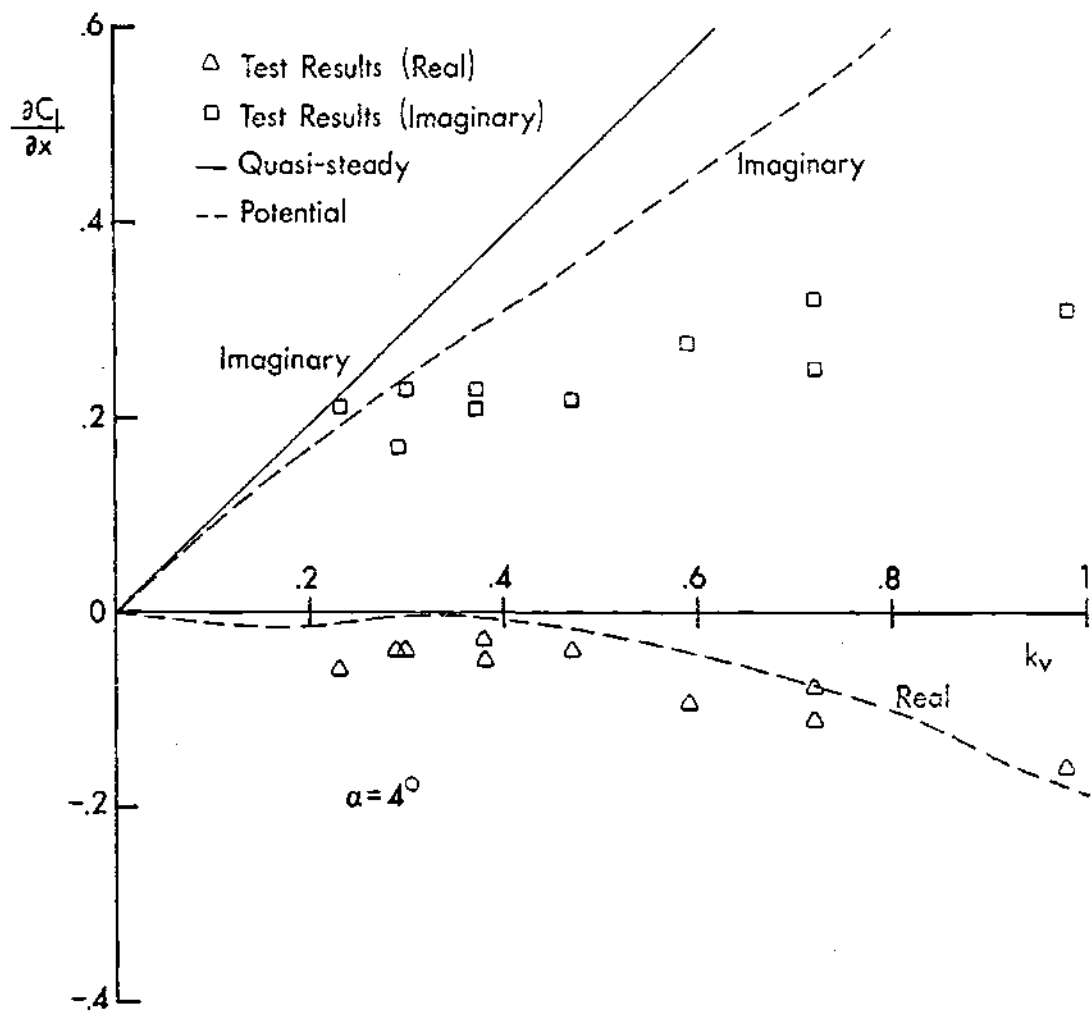


Figure 57. Lift Derivative Variations with Reduced Frequency

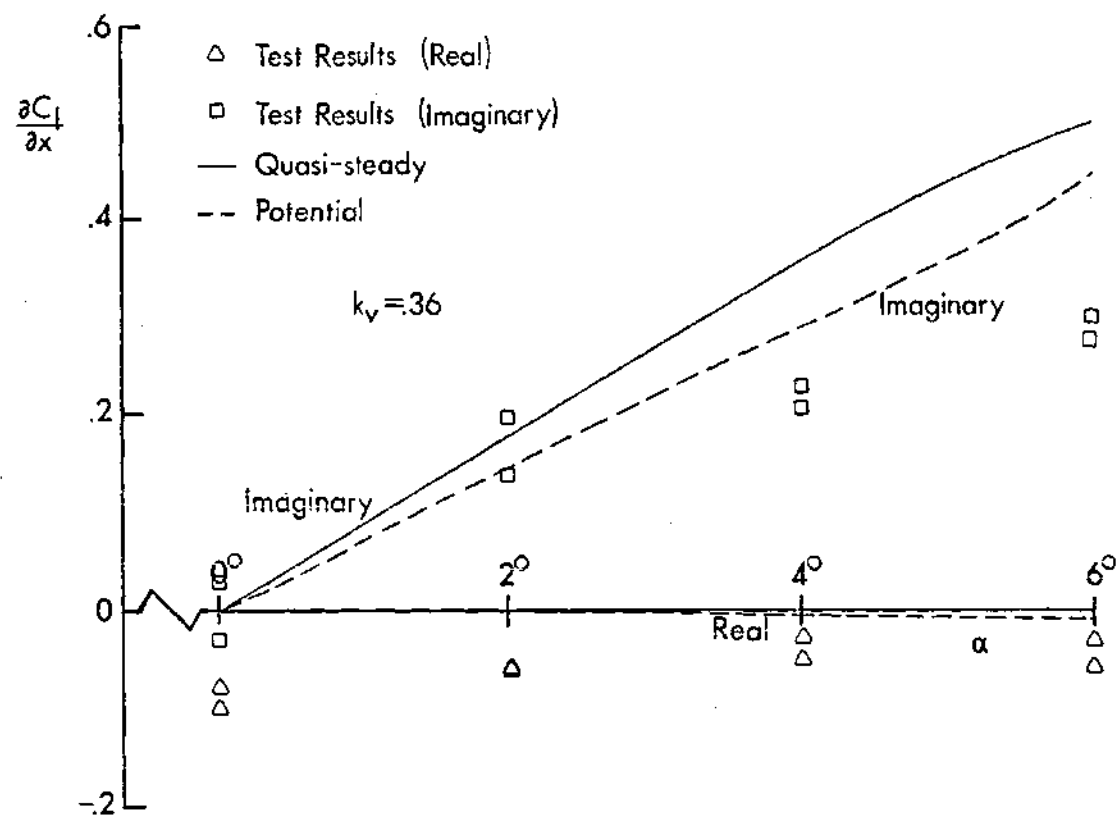


Figure 58. Lift Derivative Variations with Angle of Attack

Quasi-Steady Lift Approximation

An approximation to the unsteady flow situation like the one made for drag can also be developed. The unsteady lift is then

$$C_{\ell} = \bar{C}_L e^{i\omega_v t} \quad (34)$$

Proceeding in the same fashion as for the drag derivative,

$$\bar{C}_L = C_L \left[2 \left(\frac{V_1}{V_0} \right) + \left(\frac{V_1}{V_0} \right)^2 \right] \quad (35)$$

$$C_{\ell} = i 2 C_L k_v \bar{x} e^{i\omega_v t} \quad (36)$$

Applying Equations (23) and (24), the definitions of the real and imaginary parts of the lift derivative,

$$\left(\frac{\partial C_{\ell}}{\partial x} \right)_R = 0 \quad (37)$$

$$\left(\frac{\partial C_{\ell}}{\partial x} \right)_I = 2 C_L k_v \quad (38)$$

These equations are plotted in Figures 57 and 58 along with the experimental data. Again, the real part is zero, and coincides with the horizontal axis in both figures. The imaginary part in this approximation increases much faster than the data in Figure 57, and only a little faster than the data in Figure 58. As in the case of drag, this approximation does a better job in predicting changes with angle of attack than it does in predicting variations with reduced frequency.

Potential-Flow Approximation

Another approximation to the unsteady lift derivative can be derived from Greenberg's work [29]. In that paper, the normal force was determined for an airfoil pitching and plunging in a pulsating freestream. The force coefficient or, in this case, lift coefficient was

$$C_L^* = 2\pi\alpha_r \left\{ \frac{b}{2V_o^2} \left(\frac{\partial V}{\partial t} \right) + \frac{V}{V_o} \left[1 + \frac{V_1}{V_o} C(k_v) e^{i\omega_v t} \right] \right\} \quad (39)$$

As before, the pulsating velocity is written as

$$V = V_o + V_1 e^{i\omega_v t} \quad (40)$$

Substituting Equation (40) into (39) and expanding,

$$C_L^* = 2\pi\alpha_r \left\{ \frac{ik_v}{2} \left(\frac{V_1}{V_o} \right) e^{i\omega_v t} + 1 + \left(\frac{V_1}{V_o} \right) e^{i\omega_v t} + \left(\frac{V_1}{V_o} \right) C(k_v) e^{i\omega_v t} + \left(\frac{V_1}{V_o} \right)^2 C(k_v) e^{i2\omega_v t} \right\} \quad (41)$$

The second term of Equation (40) is obviously the steady contribution to the lift coefficient. It is also apparent that the steady lift curve slope is 2π . Applying the thickness correction for lift curve slope as before, the unsteady lift coefficient is obtained.

$$C_L = 2\pi (1 + 0.77 \tau) \alpha_r \left\{ \frac{ik_v}{2} \left(\frac{V_1}{V_0} \right) + \left(\frac{V_1}{V_0} \right) + \left(\frac{V_1}{V_0} \right) C(k_v) \right. \quad (42)$$

$$\left. + \left(\frac{V_1}{V_0} \right)^2 C(k_v) e^{i\omega_v t} \right\} e^{i\omega_v t}$$

As in the steady-flow approximation, the last term of Equation (40) is neglected as being small because of the gust amplitude ratio being squared.

Again, to put the simplified form of Equation (42) in terms of k_v and \bar{x} , Equation (11) is employed.

$$C_L = 2\pi(1 + 0.77 \tau) \alpha_r k_v \bar{x} \quad (43)$$

$$\left\{ - \left[\frac{k_v}{2} + G(k_v) \right] + i \left[1 + F(k_v) \right] \right\} e^{i\omega_v t}$$

Applying Equations (19) and (20) to get the real and imaginary parts of the lift derivative,

$$\left(\frac{\partial C_L}{\partial x} \right)_R = - 2\pi (1 + 0.77 \tau) \alpha_r k_v \left[\frac{k_v}{2} + G(k_v) \right] \quad (44)$$

$$\left(\frac{\partial C_L}{\partial x} \right)_I = 2\pi(1 + 0.77 \tau) \alpha_r k_v \left[1 + F(k_v) \right] \quad (45)$$

Like the steady-flow approximation, the real and imaginary parts of the lift derivative were plotted against reduced frequency and angle of attack. Figures 57 and 58 show the comparison of the three sets of data.

Figure 57 shows that the imaginary part of the potential-flow approximation exhibits an increase with reduced frequency, as did the test results and the quasi-steady approximation. The slope of the curve does not, however, agree well with either. On the other hand, the real part of this approximate derivative comes very close to the test data, especially at the higher reduced frequencies.

In looking at the variations of the lift derivative with angle of attack (Figure 58), the quasi-steady and the potential flow approximations are found to be close. The major difference is in the imaginary part, where the potential-flow approximation has a shallow slope. In addition, while the real part stays very close to zero at all angles, it does show some decrease.

CHAPTER XII

CONCLUSIONS AND RECOMMENDATIONS

The Georgia Tech Low Turbulence Wind Tunnel, equipped with an axial gust generator, was again used in this part of this investigation to obtain unsteady drag and lift data. Measurements were made on a two-dimensional airfoil model at constant angles of attack, and the results used to get drag and lift derivatives.

Conclusions

1. The consistency of the experimental data and its qualitative agreement with theoretical methods lend credibility to the data, and to the reliability of the experimental methods. The results are, however, of limited practical use because of the low values of Reynolds number.

2. The phase difference between drag and lift indicates that the major contribution to the unsteady drag is not pressure drag. Most likely, the major contribution is due to viscous forces.

3. The quasi-steady approximation does not give adequate results for the real and imaginary parts of the drag derivative with respect to reduced frequency or angle of attack. Neither is it particularly good for the lift derivative.

4. The potential-flow approximation is not capable of predicting drag, and would not account for the phase shift in any case. It does, however, do a better job in predicting lift than the quasi-steady approximation.

Recommendations

1. Improved drag and lift signals might be obtained by isolating the force balance mounts from the wind tunnel. If the model were mounted on heavy pylons placed on the floor, the noise induced by the gust generator might be greatly reduced.

2. An improvement in signal quality might also be attained by using thicker lift and drag beams. Since the amplifiers were set at fairly low gains, no loss of signal strength would result. In addition, it might be possible to get the total drag and lift instead of just the unsteady part.

3. Undertaking a similar investigation for higher Reynolds numbers could be done simply by using a facility that could produce higher velocities. The results of such a study would be considerably more useful in practice.

4. Using the more realistic data, and an existing blade stability analysis, the effect of unsteady drag on the stability of in-plane oscillations could be determined. This type of comparison would result in giving analysts a better idea of how accurately drag needs to be represented.

APPENDIX A

GUST GENERATOR CROSS-PLOT PROGRAM

The following program is written in FORTRAN IV for use in the Control Data Corporation CYBER 74 digital computer currently in use at Georgia Tech. The approximate compilation time for this program is 2.6 seconds. For six sets of data consisting of 30 data points per set, the approximate execution time is 0.8 seconds.

Data input to the program includes the vane width in percent and the number of data sets. This is followed by the first set of data which consists of the number of data points in the set and the vane frequency in revolutions per minute, followed by the minimum and maximum hot-wire voltages for each data point. The second data set follows the first, and so forth.

The output of this program gives the mean velocities and gust amplitudes in feet per second, for the input data in each set, plus the least-squares approximate curve for that frequency. Then, it gives the operational curves computed by the cross-plotting technique. These curves are spaced at frequency intervals equal to one-quarter of the difference between the frequencies of the original data sets.

```

PROGRAM CROSS(INPUT,OUTPUT,TAPE5=INPUT,TAPE6=OUTPUT)
C
C THIS IS A PROGRAM WHICH DETERMINES THE OPERATIONAL CURVES FOR
C THE GUST GENERATOR. FOR ANY GIVEN VANE WIDTH, IT CAN HANDLE UP
C TO 10 SETS OF DATA AT EQUALLY SPACED FREQUENCIES AND UP TO 50
C DATA POINTS PER SET. ALL DATA IS INPUT IN FREE FORMAT.
C INPUT DATA-
C IVW      VANE WIDTH (FCT)
C NS       NO. OF DATA SETS
C NA       NO. OF DATA POINTS IN THE SET
C VF       VANE FREQ FOR THE SET (RPM)
C EMIN     MINIMUM HOT-WIRE VOLTAGE (VOLTS)
C EMAX     MAXIMUM HOT-WIRE VOLTAGE (VOLTS)
C
C
C DIMENSION EMAX(50),EMIN(50),X(10,50),XX(50),Y(10,50),YY(50),
1 CA(3),C1(10,3),XF(50),XMAX(10),XMIN(10),AB(10,40),VI(40),
1 AEP(10),CE(3),C2(40,3),GFG(40),AC(40,40),CC(3),C3(40,3),
1 GF(10),ACF(40)
C
C READ IN VANE WIDTH AND NO. OF OF DATA SETS.
C READ(5,*) IVW,NS
C WRITE(6,2) IVW
C NX=NS+(3*(NS-1))
C XNX=NX-1
C
C
C SECTION 1 - CONVERT VOLTAGE TO VELOCITY AND FIT CURVES TO THE
C INPUT DATA.

```

```

      DO 101 IS=1,NS
C
C   READ IN NO. OF DATA PTS, VANE FREQ, MIN VOLTAGES, AND MAX
C   VOLTAGES FOR DATA SET IS. COMPUTE GUST FREQ FOR THE SET AND
C   STORE IN GF(I).
      READ(5,*) NA,VF
      READ(5,*) (EMIN(I),EMAX(I),I=1,NA)
      GF(IS)=VF/30.
      WRITE(6,3) GF(IS)
C
C   CONVERT HOT-WIRE VOLTAGES TO VELOCITIES. COMPUTE GUST AMPL
C   AND MEAN VELOCITY. EACH AMPLITUDE Y(I,J) CORRESPONDS TO A
C   MEAN VELOCITY X(I,J) AT GUST FREQ GF(I).
      DO 102 IA=1,NA
      EA=EMAX(IA)
      EB=EMIN(IA)
      VA=FNF(EA)
      VB=FNF(EB)
      X(IS,IA)=(VA+VB)/2.
      XX(IA)=X(IS,IA)
      Y(IS,IA)=(VA-VB)/2.
      YY(IA)=Y(IS,IA)
102  WRITE(6,4) X(IS,IA),Y(IS,IA)
C
C   DETERMINE THE COEFFICIENTS CA(I) OF THE LEAST-SQUARES CURVE
C   FOR THE DATA CORRESPONDING TO GUST FREQ GF(IS). STORE IN
C   C1(IS,I).
      CALL LSTSQR(NA,XX,YY,CA,SA)

```

```

      DO 103 I=1,3
103  C1(IS,I)=CA(I)
      WRITE (6,7)
      WRITE (6,5) GF(IS),C1 (IS,1),C1 (IS,2),C1 (IS,3),SA
      WRITE (6,8)
C    FIND THE MAX VEL USED IN THE DATA SET.  STORE IN XMAX(IS).
      DO 104 I=1,NA
104  XP (1)=X (IS,I)
      DO 105 J=2,NA
      IF (XP (1).GE.XP (J)) GO TO 105
      XMX=XP (1)
      XP (1)=XP (J)
      XP (J)=XMX
105  CONTINUE
      XMAX (IS)=XP (1)
C
C    FIND THE MIN VEL USED IN THE DATA SET.  STORE IN XMIN(IS).
      DO 106 J=2,NA
      IF (XP (1).LE.XP (J)) GO TO 106
      XMN=XP (1)
      XP (1)=XP (J)
      XP (J)=XMN
106  CONTINUE
      XMIN (IS)=XP (1)
C
C    REPEAT FOR THE NEXT DATA SET.
101  CONTINUE
      WRITE (6,7)
C

```

```

C
C SECTION 2 - CROSS-PLOT FROM THE MEAN VEL-AMPL PLANE TO THE
C GUST FREQ-AMPL PLANE.
C
C FIND THE MAX VELOCITY IN ALL DATA SETS.
  DC 201 J=2,NS
  IF(XMAX(1).GE.XMAX(J)) GO TO 201
  VMX=XMAX(1)
  XMAX(1)=XMAX(J)
  XMAX(J)=VMX
201 CONTINUE
C
C FIND THE MIN VELOCITY IN ALL DATA SETS.
  DC 202 J=2,NS
  IF(XMIN(1).LE.XMIN(J)) GO TO 202
  VMN=XMIN(1)
  XMIN(1)=XMIN(J)
  XMIN(J)=VMN
202 CONTINUE
C
C COMPUTE THE VELOCITY INTERVAL DV AND THE CORRESPONDING
C VELOCITY MATRIX VI(I).
  DV=(XMAX(1)-XMIN(1))/XNX
  DC 203 I=1,NX
203 VI(I)=XMIN(1)+((I-1)*DV)
C
C FROM THE COEFFS IN THE C1 MATRIX, COMPUTE AB(J,I). EACH
C POINT AB(J,I) IS THE AMPL AT MEAN VEL VI(I) FOR GUST FREQ

```

```

C   GF(I).  EACH ROW OF AB IS AT CONSTANT GUST FREQ AND EACH COLUMN
C   AT CONSTANT MEAN VEL.
      DO 204 I=1,NX
      DO 205 J=1,NS
      AB(J,I)=C1(J,1)+C1(J,2)*VI(I)+C1(J,3)*(VI(I)**2)
      ABF(J)=AB(J,I)
205  CONTINUE
C
C   DETERMINE THE COEFFS CE(K) OF THE LEAST-SQUARES CURVE
C   CORRESPONDING TO MEAN VEL VI(I).  STORE IN C2(I,K).
      CALL LSTSOR(NS,GF,ABF,C0,SB)
      DO 206 K=1,3
206  C2(I,K)=CE(K)
204  CONTINUE
C
C
C   SECTION 3 - CROSS-PLOT BACK FROM THE GUST FREQ-AMPL PLANE TO
C   THE MEAN VEL-AMPL PLANE.
C
C   COMPUTE THE GUST FREQ INTERVAL MATRIX.
      DO 301 I=1,NX
301  GFQ(I)=GF(1)+((I-1)*ABS((GF(2)-GF(1))/4.))
C
C   FROM THE COEFFS IN THE C2 MATRIX, COMPUTE AC(J,I).  EACH
C   POINT AC(J,I) IS THE AMPL FOR GUST FREQ GFQ(I) AT MEAN VEL
C   VI(I).  EACH ROW OF AC IS AT CONSTANT MEAN VEL AND EACH
C   COLUMN AT CONSTANT GUST FREQ.
      DO 302 I=1,NX
      DO 303 J=1,NX

```

```

      AC(J,1)=C2(J,1)+C2(J,2)*GFC(I)+C2(J,3)*(GFC(I)**2)
      ACF(J)=AC(J,1)
303  CONTINUE
C
C   DETERMINE THE LOEFFS CC(K) OF THE LEAST-SQUARES CURVE
C   CORRESPONDING TO GUST FREQ GFC(I).  STORE IN C3(I,K).
      CALL LSTSQR(NX,VI,ACF,CC,SC)
      DO 304 K=1,3
304  C3(I,K)=CC(K)
302  CONTINUE
C
      WRITE(6,6)
      DO 305 I=1,NX
      WRITE(6,5) GFC(I),C3(I,1),C3(I,2),C3(I,3),SC
305  CONTINUE
      WRITE(6,9)
C
C
C   THE OUTPUT OF THIS PROGRAM GIVES FIRST THE ORIGINAL DATA AND
C   THE CURVE FITS.  THEN, THE OPERATIONAL CURVES ARE GIVEN.  ALL
C   VELOCITIES ARE IN FT/SEC.  THERE ARE 3 CURVES FIT BETWEEN
C   EACH ORIGINAL CURVE.
C
2   FORMAT (1H1,13X, 44H***** VANE CALIBRATION CROSS-PLOT DATA *****
17/13X,19H***** VANE WIDTH = ,I2,14H PERCENT *****//23X,
224H* RAW WIND TUNNEL DATA *//)
3   FORMAT (9X,16HGUST FREQUENCY =,F6.2,30H HZ      MEAN SPEED      AMPLIIT
1UDE//)

```

```

4  FORMAT (40X,F7.3,5X,F7.3)
5  FORMAT (1X,F6.2,3H HZ,3X,8HAMFL = (,E11.5,5H) + (,E11.5,
17H)*V + (,E11.5,8H)*(V**2)/13X,21HSTANDARD DEVIATION = ,E10.4/)
6  FORMAT (1H1,23X,24H** OPERATIONAL CURVES **/)
7  FORMAT(/)
8  FORMAT(//)
9  FORMAT(1H1)
   END

```

```

FUNCTION FNF(E)

```

```

C
C THIS FUNCTION CONVERTS HOT-WIRE VOLTAGE TO WIND TUNNEL VELOCITY
C USING THE CALIBRATION CURVE FNF(E).

```

```

C
   FNF1=215.1-((47770-(2256*(E**2)))**.5)
   FNF=FNF1**2
   RETURN
   END

```

```

      SUBROUTINE LSTISQR(N,X,Y,C,S)
C
C THIS SUBROUTINE COMPUTES BOTH FIRST-ORDER AND SECOND-ORDER
C LEAST-SQUARES APPROXIMATIONS FOR THE INPUT DATA. THEN, IT
C CHOOSES THE BETTER FIT ON THE BASIS OF THE STANDARD DEVIATION.
C INPUT PARAMETERS-
C   N           NO. OF DATA PTS
C   X(N)        ABSCISSAS OF THE DATA PTS
C   Y(N)        ORDINATES OF THE DATA PTS
C OUTPUT PARAMETERS-
C   C(1)        COEFFS OF THE BETTER FIT
C   S           STANDARD DEVIATION OF THE BETTER FIT
C
C
C   DIMENSION SX(4),SY(2),SXY(2),X(N),Y(N),C(3)
C   XN=N
C   XNI=1./XN
C
C CLEAR SX, SY, SXY MATRICES.
C   DO 10 I=1,4
C     SX(I)=0.0
C     IF(I-3) 11,10,10
11  SY(I)=0.0
C     SXY(I)=0.0
10  CONTINUE
C
C COMPUTE SX(I), SY(I), SXY(I).
C   DO 12 I=1,4
C     DO 13 J=1,N

```

```

      SX(I)=SX(I)+(X(J)**I)
      IF (I-3) 14,13,13
14    SY(I)=SY(I)+(Y(J)**I)
      SXY(I)=SXY(I)+((X(J)**I)*Y(J))
13    CONTINUE
12    CONTINUE
C
      S243=(SX(2)*SX(4))-(SX(3)**2)
      S2314=(SX(2)*SX(3))-(SX(1)*SX(4))
      S132=(SX(1)*SX(3))-(SX(2)**2)
      S123=(SX(1)*SX(2))-(XN*SX(3))
      S21=(XN*SX(2))-(SX(1)**2)
      S42=(XN*SX(4))-(SX(2)**2)
      DEL=(XN*S243)+(SX(1)*S2314)+(SX(2)*S132)
      DELI=1./DEL
C
C  COMPUTE THE COEFFS OF THE FIRST-ORDER FIT.
      B1=(SXY(1)-(XNI*SX(1)*SY(1)))/(SX(2)-(XN*(SX(1)**2)))
      A1=(SY(1)*XNI)-(B1*(SX(1)*XNI))
C
C  COMPUTE THE STD DEV OF THE FIRST-ORDER FIT
      S01=SY(2)-(XNI*(SY(1)**2))-(B1*(SXY(1)-(XNI*SX(1)*SY(1))))
      IF (S01.LE.1.E-05) GO TO 21
      S1=SQRT(S01/(XN-2.))
      GO TO 22
21    S1=0.0
22    CONTINUE
C

```

```

C  COMPUTE THE COEFFS OF THE SECOND-ORDER FIT.
    C2=DELI*((S132*SY(1))+(S123*SXY(1))+(S21*SXY(2)))
    P2=DELI*((S2314*SY(1))+(S42*SXY(1))+(S123*SXY(2)))
    A2=DELI*((S243*SY(1))+(S2314*SXY(1))+(S132*SXY(2)))
C
C  COMPUTE THE STD DEV OF THE SECOND-ORDER FIT.
    S02=SY(2)-(A2*SY(1))-(B2*SXY(1))-(C2*SXY(2))
    IF(S02.LE.1.E-15) GO TO 23
    S2=SQRT(S02/(XN-3.))
    GO TO 24
23  S2=0.0
24  CONTINUE
C
C  CHOOSE THE SMALLER STD DEV AND STORE THE CORRESPONDING COEFFS
C  IN C(I).
    IF(S1-S2) 15,15,16
15  C(1)=A1
    C(2)=B1
    C(3)=0.0
    S=S1
    GO TO 17
16  C(1)=A2
    C(2)=B2
    C(3)=C2
    S=S2
17  RETURN
    END

```

APPENDIX B

FORCE BALANCE DESIGN CALCULATIONS

The selection of dimensions for the lift and drag beams consisted of only determining the beam thicknesses, the lengths and widths being dependent on the strain gage dimensions. Selecting a suitable thickness for each beam involved considering both the bridge output voltage and the natural frequency of the model and its supporting system. For loads to which the system would be subjected, it was found that the natural frequency constraint was more stringent than any yield stress considerations. Thus, the calculations of the maximum stresses in the beams at maximum loading were not undertaken.

Load Increments

The sensitivities of the lift and drag measurements were dependent on the smallest load increments which the strain gage bridges could accurately measure. To select a suitable increment for both lift and drag, the maximum loads that could be expected were estimated and divided by 100.

For this estimate, Equations (5) and (6) from Chapter X were used. The values in Table 8 were substituted into the equations to get the maximum possible lift and drag loads. Dividing them by 100, the drag increment (ΔD) became 0.004 lb., and the lift increment (ΔL) became 0.1 lb.

Table 8. Constants for the Force Balance Computations

Variable	Definition	Value
ρ	density of air (lb-sec ² /ft ⁴)	.00238
V	test-section velocity (ft/sec)	50
s	model span (ft)	3.5
c	model chord (ft)	.75
C _D	steady-flow drag coefficient	.05
C _L	steady-flow lift coefficient	2.5
AD	drag increment (lb)	.004
AL	lift increment (lb)	.1
E _{Al}	Young's modulus for aluminum (lb/in ²)	10.6 x 10 ⁶
e _i	bridge exciting voltage (volts)	8
m _s	total sprung mass (lb-sec ² /in)	.0104
F _d	drag gage factor	110
x _d *	drag gage location (in)	.125
s _d	drag beam length (in)	.75
w _d	drag beam width (in)	.375
h _d	drag beam thickness (in)	.025
F _l	lift gage factor	2
x _l *	lift gage location (in)	1
s _l	lift beam length (in)	3
w _l	lift beam width (in)	.5
h _l	lift beam thickness (in)	.08

Drag Bridge Output

The "S" bending beam (Figure 59a), used as the sensing element for drag, has a point of inflection in its deflection curve at the mid-point of the beam [48]. Thus, there is no moment at that point, and each half of the beam can be considered independently as a cantilevered-free configuration (Figure 59b). The load applied to each beam is a quarter of the total drag load because there are four of these beams supporting the model.

Analyzing the cantilevered-free beam, the bending moment as a function of x^* is given by

$$M_d = D (s_d - 2x^*)/8 \quad , \quad 0 \leq x^* \leq s_d/2 \quad (46)$$

The strain at any point, $0 \leq x^* \leq s_d/2$, on the beam can then be found, assuming a linearly elastic material (aluminum) and using the expression for the moment of inertia of a rectangular cross-section.

$$|\epsilon_d| = 3 D (s_d - 2x^*) / 4 E_{Al} w_d h_d^2 \quad (47)$$

For a strain gage bridge with four active arms, the change in output voltage for any change in strain ($\Delta\epsilon_d$) is

$$\Delta e_d = F_d e_i \Delta\epsilon_d \quad (48)$$

Substituting into Equation (48) the change in strain from Equation (47) resulting from a change in drag equal to the drag increment (ΔD),

$$\Delta e_d = 3 F_d e_i \Delta D(s_d - 2 x_d^*) / 4 E_{At} w_d h_d^3 \quad (49)$$

Then, using the appropriate constants from Table 8, the change in bridge output voltage due to an incremental drag change is found to be 531 microvolts. The resulting signal-to-noise ratio is approximately 110 for a noise level of 5 microvolts.

Drag Stiffness

Returning to Figure 59a, the deflection per unit load at the point of load application is [48]

$$\delta_d = s_d^3 / E_{At} w_d h_d^3 \quad (50)$$

Then, the beam stiffness becomes

$$K_d = E_{At} w_d h_d^3 / s_d^3 \quad (51)$$

To compute the natural frequency of this system, it is necessary to know how the system is sprung, the total stiffness, and the sprung mass. The weight of the model, spar, and angle of attack disks was estimated to be four pounds. Figure 59c illustrates how the model was supported. The stiffness of the entire system is equal to the sum of the four drag beam stiffness [49].

$$K_{ds} = 4 E_{At} w_d h_d^3 / s_d^3 \quad (52)$$

The natural frequency of the system, in Hertz, is then

$$f_d = \sqrt{K_{ds}/m_s} / 2\pi \quad (53)$$

Substituting Equation (52) into Equation (53),

$$f_d = \sqrt{E_{Al} w_d h_d^3 / s_d^3 m_s} / \pi \quad (54)$$

Then, using the constants from Table 8, the natural frequency was calculated to be approximately 38 Hertz.

Lift Bridge Output

Because of the flexibility of the drag beams, it might be thought that the lift beam can be idealized as a beam pinned at both ends (Figure 60a). From Figure 42, it might also appear that it is built-in at both ends (Figure 60b). However, neither is correct. In fact, while it is possible for both ends to have a finite slope, neither end is completely free to rotate. The beam can be approximated by placing torsional springs at both ends of a pinned-pinned beam (Figure 60c), each contributing a moment reaction equal to half of that found in a beam built-in at both ends. The bending moment as a function of x^* then becomes [50]

$$M_l = L(8x_l^* - s_l)/32 \quad , \quad 0 \leq x_l^* \leq s_l/2 \quad (55)$$

The strain at the point of gage application, assuming a linearly elastic material, is then

$$|\epsilon_l| = 3 L(8x_l^* - s_l)/16 E_{Al} w_l h_l^2 \quad (56)$$

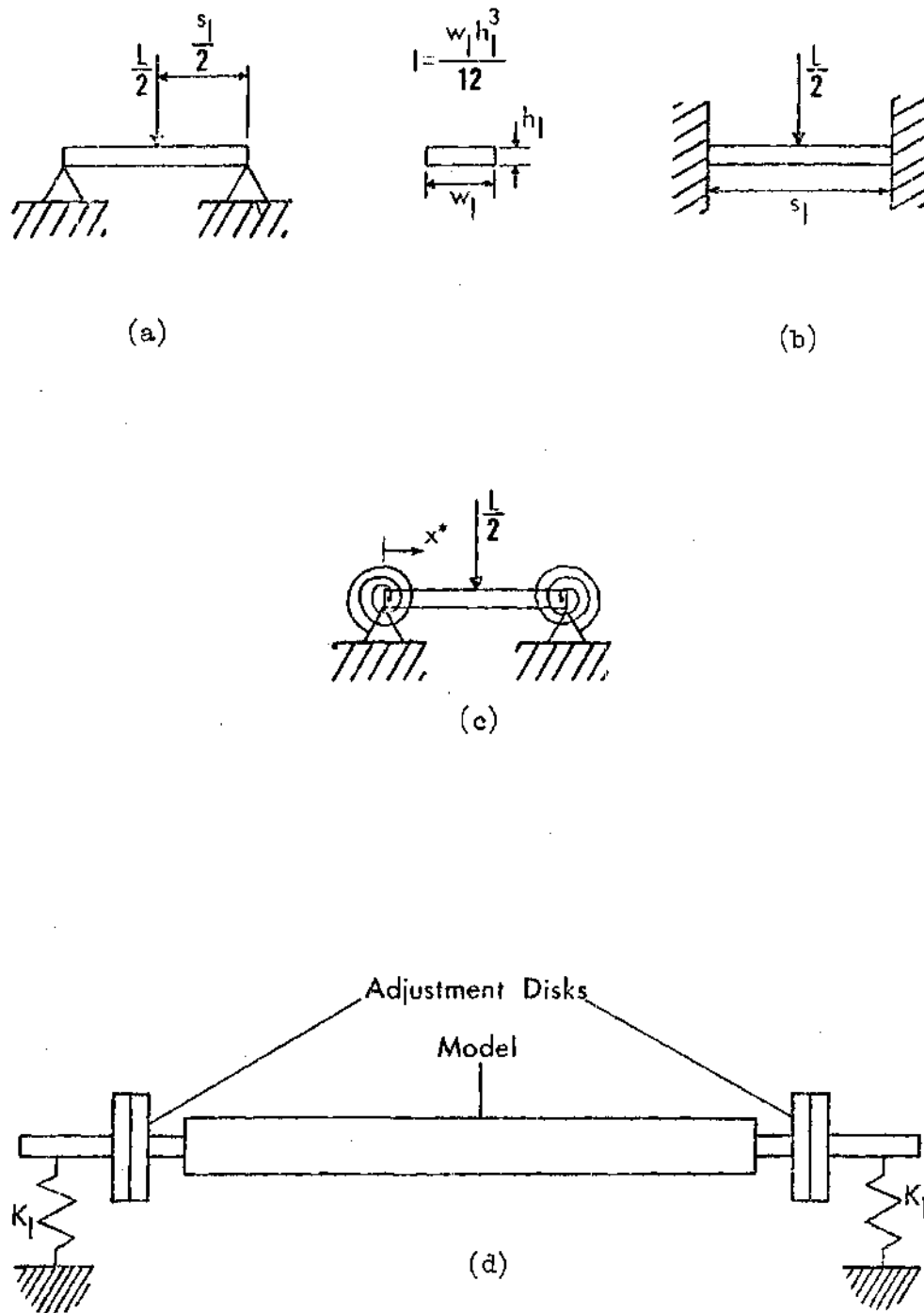


Figure 60. Force Balance Lift Beam

Using the expression for a four-active-arm bridge similar to Equation (48), and substituting the change in strain due to an incremental lift change (ΔL).

$$\Delta e_l = 3 F_l e_i \Delta L (8x_l^* - s_l) / 16 E_{Al} w_l h_l^2 \quad (57)$$

Substituting into the right-hand-side of Equation (57) from Table 8, the lift bridge incremental output is found to be 44 microvolts, giving a signal-to-noise ratio of approximately 9 for a noise level of 5 microvolts.

Lift Stiffness

Using the same boundary conditions that were used to compute the lift bridge output, the deflection of the beam center per unit load is [50]

$$\delta_l = 5 s_l^3 / 32 E_{Al} w_l h_l^3 \quad (58)$$

The beam stiffness is then

$$K_l = 32 E_{Al} w_l h_l^3 / 5 s_l^3 \quad (59)$$

As shown in Figure 60d, the model is supported in such a way as to make the stiffness of the system twice that of a single beam [49].

$$K_{ls} = 64 E_{Al} w_l h_l^3 / 5 s_l^3 \quad (60)$$

The natural frequency in Hertz is then written as

$$f_l = 4 \sqrt{E_{Al} w_l h_l^3 / 5 s_l^3 m_s / \pi} \quad (61)$$

Again using the constants from Table 8, the lift natural frequency is computed to be 56 Hertz.

REFERENCES

1. Ham, N. D., "An Experimental Investigation of Stall Flutter," Journal of the American Helicopter Society, Vol. 7, No. 1, January 1962, pp. 3-16.
2. Ham, N. D., and Young, M. I., "Torsional Oscillation of Helicopter Blades Due to Stall," Journal of Aircraft, Vol. 3, No. 3, May-June 1966, pp. 218-224.
3. Liiva, J., "Unsteady Aerodynamics and Stall Effects on Helicopter Rotor Blade Airfoil Sections," Journal of Aircraft, Vol. 6, No. 1, January-February 1969, pp. 46-51.
4. Liiva, J., and Davenport, F. J., "Dynamic Stall of Airfoil Sections for High Speed Rotors," Journal of the American Helicopter Society, Vol. 14, No. 2, April 1969, pp. 26-33.
5. Johnson, W., "The Effect of Dynamic Stall on the Response and Airloading of Helicopter Rotor Blades," Journal of the American Helicopter Society, Vol. 14, No. 2, April 1969, pp. 68-79.
6. Patay, S. A., "Leading Edge Separation on an Airfoil During Dynamic Stall," MIT Aeroelastic and Structures Research Laboratory, ASRL TR 156-1, October 1969.
7. Windsor, R. I., "Measurement of Aerodynamic Forces on an Oscillating Airfoil," USAAVLABS Technical Report 69-98, March 1970.
8. Velkoff, H. R., Blaser, D. A., and Jones, K. M., "Boundary Layer Discontinuity on a Helicopter Rotor Blade in Hovering," Journal of Aircraft, Vol. 8, No. 2, February 1971, pp. 101-107.
9. Ericsson, L. E., and Reding, J. P., "Unsteady Airfoil Stall Review and Extension," Journal of Aircraft, Vol. 8, No. 8, August 1971, 609-616.
10. Carta, F. O., "A Theoretical Study of the Effect of Unsteady Pressure Gradient on Dynamic Stall Delay," Journal of Aircraft, Vol. 8, No. 10, October 1971, pp. 839-841.
11. McCroskey, W. J., "Recent Developments in Rotor Blade Stall," AGARD Conference Preprint No. 111, Aerodynamics of Rotary Wings, Marseilles, France, September 1972.

12. Philippe, J. J., and Sagner, M., "Calcul et Mesure des Forces Aerodynamiques sur un Profil Oscillant avec et sans Decrochage," Presented at the AGARD Specialists' Meeting on 'The Aerodynamics of Rotary Wings,' Marseilles, France, September 13-15, 1972.
13. Ward, J. F., and Young, W. H., Jr., "A Summary of Current Research in Rotor Unsteady Aerodynamics with Emphasis on Work at Langley Research Center," AGARD Conference Preprint No. 111, Aerodynamics of Rotary Wings, Marseilles, France, September 1972.
14. Johnson, W., and Ham, N. D., "On the Mechanism of Dynamic Stall," Journal of the American Helicopter Society, Vol. 17, No. 4, October 1972, pp. 36-45.
15. Jones, W. P., McCroskey, W. J., and Costes, J. J., "Unsteady Aerodynamics of Helicopter Rotors," NATC AGARD Report No. 595, October 1972.
16. Martin, J. M., Empey, R. W., McCroskey, W. J., and Caradonna, F. X., "A Detailed Experimental Analysis of Dynamic Stall on An Unsteady Two-Dimensional Airfoil," AHS Preprint No. 702, Presented at the 29th Annual National Forum of the American Helicopter Society, Washington, D.C., May 1973.
17. Ham, N. D., "Aerodynamic Loading on a Two-Dimensional Airfoil during Dynamic Stall," AIAA Journal, Vol. 6, No. 10, October 1968, pp. 1927-1933.
18. Harris, F. D., Tarzanin, F. J., Jr., and Fisher, R. K., Jr., "Rotor High Speed Performance, Theory vs. Test," Journal of the American Helicopter Society, Vol. 15, No. 3, July 1970, pp. 35-44.
19. Ericsson, L. E., and Reding, J. P., "Dynamic Stall of Helicopter Blades," Journal of the American Helicopter Society, Vol. 17, No. 1, January 1972, pp. 11-19.
20. Tarzanin, F. J., Jr., "Prediction of Control Loads Due to Blade Stall," Journal of the American Helicopter Society, Vol. 17, No. 4, April 1972, pp. 33-45.
21. Crimi, P., and Reeves, B. L., "A Method for Analyzing Dynamic Stall of Helicopter Rotor Blades," NASA CR-2009, May 1972.
22. Carta, F. O., Commerford, G. L., Carlson, R. G., and Blackwell, R. H., "Investigation of Airfoil Dynamic Stall and Its Influence on Helicopter Control Loads," USAAMRDL Technical Report 72-51, September 1972.
23. Carta, F. O., Commerford, G. L., and Carlson, R. G., "Determination of Airfoil and Rotor Blade Dynamic Stall Response," Journal of the American Helicopter Society, Vol. 18, No. 2, April 1973, pp. 31-39.

24. Carlson, R. G., Blackwell, R. H., Commerford, G. L., and Mirick, P. H., "Dynamic Stall Modeling and Correlation with Experimental Data on Airfoils and Rotors," Presented at the AHS/NASA-Ames Specialists' Meeting on Rotorcraft Dynamics, Moffett Field, California, February 13-15, 1974.
25. Malone, J. B., "Dynamic Stall Characteristics of an Oscillating Airfoil in a Harmonically Varying Freestream Velocity," Ph.D. Thesis, Georgia Institute of Technology, December 1974.
26. Gault, D. E., "A Correlation of Low-Speed, Airfoil-Section Stalling Characteristics with Reynolds Number and Airfoil Geometry," NACA TN 3963, March 1957.
27. Ericsson, L. E., and Reding, J. P., "Dynamic Stall Simulation Problems," Journal of Aircraft, Vol. 8, No. 7, July 1971, pp. 579-583.
28. Kottapalli, S.B.R., "Application of an Empirical Technique to Predict Airfoil Dynamic Stall," Georgia Institute of Technology, School of Aerospace Engineering, Student Special Problem, October 1973.
29. Greenberg, J. M., "Airfoil in Sinusoidal Motion in a Pulsating Stream," NACA TN 1326, June 1947.
30. Theodorsen, T., "General Theory of Aerodynamic Instability and the Mechanism of Flutter," NACA Report 496, 1935.
31. Ormiston, R. A., "Comparison of Several Methods for Predicting Loads on a Hypothetical Helicopter Rotor," Presented at the AHS/NASA-Ames Specialists' Meeting on Rotorcraft Dynamics, Moffett Field, California, February 13-15, 1974.
32. Hohenemser, K. H., and Heaton, P. W., Jr., "Aeroelastic Instability of Torsionally Rigid Helicopter Blades," Journal of the American Helicopter Society, Vol. 12, No. 2, April 1967, pp. 1-13.
33. Elman, H. L., Niebanck, C. F., and Bain, L. J., "Prediction of Rotor Instability at High Forward Speeds, Vol. V," USAAVLABS Technical Report 68-18E, February 1969.
34. Arcidiacono, P. J., "Prediction of Rotor Instability at High Forward Speeds, Vol. I," USAAVLABS Technical Report 68-18A, February 1969.
35. Jenkins, J. L., Jr., "A Numerical Method for Studying the Transient Blade Motions of a Rotor with Flapping and Lead-Lag Degrees of Freedom," NASA TN D-4195, October 1967.
36. Jenkins, J. L., Jr., "A Parametric Study of Blade-Motion Stability Boundaries for an Articulated Rotor," NASA TN D-5032, February 1969.

37. Ormiston, R. A., and Hodges, D. H., "Linear Flap-Lag Dynamics of Hingeless Helicopter Rotor Blades in Hover," Journal of the American Helicopter Society, Vol. 17, No. 2, April 1972, pp. 2-14.
38. Ormiston, R. A., and Bousman, W. G., "A Theoretical and Experimental Investigation of Flap-Lag Stability of Hingeless Helicopter Rotor Blades," NASA TM X-62179, August 1972.
39. Hodges, D. H., and Ormiston, R. A., "Nonlinear Equations for Bending of Rotating Beams with Application to Linear Flap-Lag Stability of Hingeless Rotors," NASA TM X-2770, May 1973.
40. Friedmann, P., and Tong, P., "Non-linear Flap-Lag Dynamics of Hingeless Helicopter Blades in Hover and in Forward Flight," Journal of Sound and Vibration, Vol. 30, No. 1, September 1973, pp. 9-31.
41. Friedmann, P., and Silverthorn, L. J., "Flap-Lag Dynamics of Hingeless Helicopter Blades at Moderate and High Advance Ratios," Presented at the AHS/NASA-Ames Specialists' Meeting on Rotorcraft Dynamics, Moffett Field, California, February 13-15, 1974.
42. Chou, P. C., "Pitch-Lag Instability of Helicopter Rotors," Journal of the American Helicopter Society, Vol. 3, No. 3, July 1958, pp. 30-39.
43. Ormiston, R. A., and Bousman, W. G., "A Study of Stall-Induced Flap-Lag Instability of Hingeless Rotors," AES Preprint No. 730, 29th Annual National Forum of the American Helicopter Society, Washington, D. C., May 1973.
44. Crimi, P., "A Method for Analyzing the Aeroelastic Stability of a Helicopter Rotor in Forward Flight," NASA CR-1332, August 1969.
45. Bellinger, E. D., "Analytical Investigation of the Effect of Blade Flexibility, Unsteady Aerodynamics, and Variable Inflow on Helicopter Rotor Stall Characteristics," NASA CR-1769, September 1971.
46. Karamcheti, K., Principles of Ideal-Fluid Aerodynamics, John Wiley and Sons, Inc., New York, 1966.
47. Jacobs, E. N., and Sherman, A., "Airfoil Section Characteristics as Affected by Variations in Reynolds Number," NACA Report 586, 1937.
48. Pollock, N., "The Optimum Design of Strain Gauge Sting Balances for Wind Tunnel Models," Australian Defence Scientific Service Report ARL/A 133, March 1969.
49. Thomson, W. T., Vibration Theory and Applications, Prentice-Hall, Inc., Englewood Cliffs, N. J., 1965.

50. Niles, A. S., and Newell, J. S., Airplane Structures, Volume I, John Wiley and Sons, Inc., New York, 1949.

VITA

Donald Lee Kunz is the son of Mildred K. and Clarence E. Kunz of Geneva, New York. He was born, in Geneva, on October 19, 1949. His younger brother, Richard, is married, and he and his wife, Stephanie, live in Atlanta, Georgia.

Mr. Kunz attended elementary and secondary school in Geneva, and graduated from Geneva High School in 1967. Then, he enrolled at Syracuse University. While in Syracuse, he became a member of Tau Beta Pi, Pi Tau Sigma, and Phi Kappa Phi. In his senior year, he was selected as a co-captain of the varsity track team and received the ECAC Medal Merit. After his graduation from Syracuse in June 1971, with a Bachelor of Science in Aerospace Engineering, Mr. Kunz went to the Georgia Institute of Technology. There, he received a Master of Science in Aerospace Engineering in August of 1972.

Continuing his education at Georgia Tech, Mr. Kunz, under the direction of Dr. G. Alvin Pierce, embarked on a program of study that would earn him a doctorate. While pursuing his course, he also competed on the Georgia Tech Lacrosse Club, and later became an assistant coach with the team. In addition, he became a member of the AIAA, and joined the Society of Sigma Xi and the American Helicopter Society.